

# REPORT DOCUMENTATION PAGE

AFRL-SR-AR-TR-03-

Public reporting burden for this collection of information is estimated to average 1 hour per response, including the time for reviewing instructions, searching existing data sources, gathering the required data, reviewing existing materials on the subject, completing the collection of information. Send comments regarding this burden estimate or any other aspect of this collection of information, including suggestions for reducing the burden, to Washington Headquarters Services, Directorate for Information Operations and Reports, 1215 Jefferson Davis Highway, Suite 1204, Arlington, VA 22202-4302, and to the Office of Management and Budget, Paperwork Reduction Project (0704-0182), Washington, DC 20503.

0248

1. AGENCY USE ONLY (Leave blank)		2. REPORT DATE		3. REPORT TYPE AND DATES COVERED	
				15 February 2000 to 29 November 2002	
4. TITLE AND SUBTITLE Development of Robust Boundary Layer Controllers				5. FUNDING NUMBERS F49620-00-1-0166	
6. AUTHOR(S) Jason Speyer					
7. PERFORMING ORGANIZATION NAME(S) AND ADDRESS(ES) Mechanical and Aerospace Engineering Department University of California, LA Los Angeles, CA 90005-1597				8. PERFORMING ORGANIZATION REPORT NUMBER	
9. SPONSORING/MONITORING AGENCY NAME(S) AND ADDRESS(ES) AFOSR/NM 4015 Wilson Blvd, Room 713 Arlington, VA 22203-1954				10. SPONSORING/MONITORING AGENCY REPORT NUMBER  F49620-00-1-0166	
11. SUPPLEMENTARY NOTES					
12a. DISTRIBUTION AVAILABILITY STATEMENT APPROVED FOR PUBLIC RELEASE, DISTRIBUTION UNLIMITED				12b. DISTRIBUTION CODE	
13. ABSTRACT (Maximum 200 words) In this study, control system analysis and design techniques were developed to control turbulent and convective boundary layers. The design was dependant solely on the linearized governing equations of a channel flow and a layer of heated fluid. The three-dimensional Navier-Stokes equations of channel flow, linearized about a Poiseuille profile, and Oberbeck-Boussinesq equations of a layer of fluid, linearized about the no motion state, were decomposed by a spectral decomposition involving a two-dimensional Fourier expansion and a Chebyshev Galerkin projection. The resulting temporal state space model, composed of the coefficients of this decomposition, allowed for a multivariable feedback design combining an array of sensors to an array of actuators. In particular, this spectral decomposition decouples the dynamical equations into a parallel architecture, where each wave number pair sub-system could be handled individually. Linear Quadratic Gaussian (LQG) multivariable synthesis and model reduction techniques are applied to a few select wave number pair sub-systems, reducing the required computational bandwidth. Controller performance was tested on direct numerical simulations. Even with a limited number of controlled wave number pairs and a drastic reduction in state space size, the controllers have proven remarkably effective.					
14. SUBJECT TERMS				15. NUMBER OF PAGES 121	
				16. PRICE CODE	
17. SECURITY CLASSIFICATION OF REPORT		18. SECURITY CLASSIFICATION OF THIS PAGE		19. SECURITY CLASSIFICATION OF ABSTRACT	
				20. LIMITATION OF ABSTRACT	

20030731 046

# DEVELOPMENT OF ROBUST BOUNDARY LAYER CONTROLLERS

Grant No. 49620-00-1-0166  
*Air Force Office of Scientific Research*  
Dr. Belinda King, Technical Contact  
AFOSR/NM  
Mathematics Division

Jason L. Speyer and John Kim  
Mechanical and Aerospace Engineering Department  
University of California, Los Angeles  
Los Angeles, CA 90095-1597

Final Report

February 28, 2003

In this study, control system analysis and design techniques were developed to control turbulent and convective boundary layers. The design was dependent solely on the linearized governing equations of a channel flow and a layer of heated fluid. The three-dimensional Navier-Stokes equations of channel flow, linearized about a Poiseuille profile, and Oberbeck-Boussinesq equations of a layer of fluid, linearized about the no motion state, were decomposed by a spectral decomposition involving a two-dimensional Fourier expansion and a Chebyshev-Galerkin projection. The resulting temporal state space model, composed of the coefficients of this decomposition, allowed for a multivariable feedback design combining an array of sensors to an array of actuators. In particular, this spectral decomposition decouples the dynamical equations into a parallel architecture, where each wavenumber pair sub-system could be handled individually. Linear Quadratic Gaussian (LQG) multivariable synthesis and model reduction techniques are applied to a few select wavenumber pair sub-systems, reducing the required computational bandwidth. Controller performance was tested on direct numerical simulations. Even with a limited number of controlled wavenumber pairs and a drastic reduction in state space size, the controllers have proven remarkably effective.

# Table of Contents

Project Summary	i
1. Introduction	1
2. Achievements	3
2.1 A Linear Process in Wall-Bounded Shear Flows	3
2.2 Application of Reduced-Order Controller to Turbulent Flows for Drag Reduction	3
2.3 Robust Feedback Control of Rayleigh-Bénard Convection	5
3. Conclusions and Future Work	7
4. References	8
APPENDIX A: A Linear Process in Wall-Bounded Turbulent Shear Flows	
APPENDIX B: Application of Reduced-Order Controller to Turbulent Flows for Drag Reduction	
APPENDIX C: Robust Feedback Control of Rayleigh-Bénard Convection	
APPENDIX D: Active Suppression of Finite Amplitude Rayleigh-Bénard Convection	
APPENDIX E: Control of Turbulent Boundary Layers	

# 1 Introduction

The potential benefits of controlling flows to reduce drag are significant. In its New World Vistas report, the Air Force identifies active flow control, boundary layer control in particular, as one of the essential enabling technologies for efficient cruise aircraft. Furthermore, little imagination is required to see that active control of boundary layers can benefit many more applications. Furthermore, the suppression of the onset of convection in a boundary layer of fluid has potentially important applications in controlling the quality of material for certain manufacturing processes such as in the production of large silicon wafers and composite material for turbine blades.

Due to its importance as well as its genuine intellectual challenge, flow control has attracted much attention from many fluid dynamicists. However, until recently, research has been based primarily on the investigator's physical intuition. With the discovery of coherent turbulence structures within the near-wall region of turbulent boundary layers, some additional progress has been made. Choi et al. [1], for example, report an active control scheme, which was designed to reduce the strength of the near-wall streamwise vortices. This active control scheme, which was based on observations that there are strong correlations between the near-wall streamwise vortices and the high skin-friction region, is reported to reduce the viscous drag by as much as 25%.

It is our belief, however, that much more progress can be made for more classes of flows and other phenomena if we can avoid the need for empirical observations and apply modern control theories to linear equations that approximate the non-linear phenomena. For fluid flows, a few examples of this approach have appeared in the recent literature. The foundations of applying optimal control theory to the equations governing fluid flow were developed and its application to flow control was reported by Choi et al. [2], Moin and Bewley [3], and Lee et al. [4].

Our group has developed a methodology to synthesize reduced-order controllers to target the linear mechanisms of a channel flow, identified from the Navier-Stokes equations, and Rayleigh-Bénard convection in a fluid layer, identified from the Oberbeck-Boussinesq equations. Linearized around the Poiseuille profile or the no motion state, the dynamical equations are further modified to allow for actuation and sensors. Spectrally decomposed, the governing equations can be cast into temporal state-space form to which modern control theories can be applied. The system equations decouple into independent sub-systems by wavenumbers, affording the option to design controllers for certain wavenumbers. A parallel architecture of compensators in wave space is thus possible [5].

The research began with a simple integral controller on the streamwise shear stress in a strictly 2 dimensional linear flow [6]. Although it was only applied to, at most, a few wavenumbers, it was able to control a two-dimensional finite-amplitude disturbance responsible for the secondary instability, thus suggesting that nonlinear effects could be handled by a linear controller. However, the main thrust of the paper was to show the importance of analyzing the properties of the flow dynamic equations from a control theoretic viewpoint. Subsequently, a controller was developed using Linear-Quadratic-Gaussian (LQG) optimal



control synthesis, producing a controller, which required less energy than the simple integral compensator [7]. However, the resulting state space was quite large and motivated the development of state reduction by a form of balanced realization for LQG design. The uncertainty was assumed to be emanating from the wall and was modeled as an input with the same input matrix as the control. For the two dimensional controller, where the system is minimal phase, good loop transfer recovery was obtained producing good stability margins for robust control [5,8].

The parallel structured controller of [5] for multiple (but not all) wavenumbers was successful in suppressing up to 90% of the wall shear stress in a linearized two-dimensional Navier-Stokes channel flow. The controller was then embedded in a direct simulation of the Navier-Stokes equations [9]. Although controlling skin-friction drag in two dimensions cannot be readily extrapolated to the three-dimensional turbulence case, the linear controller (using 10% of the order of the full system) applied to the bottom wall of a two-dimensional turbulent periodic channel flow at a Reynolds number of 1,500, managed a drag reduction of up to 60% with respect to the uncontrolled turbulent flow.

Given the success with the flow equations, the same methodology was applied to the Rayleigh-Bénard problem of delaying the onset of convection in a fluid layer heated from below. Due to the nature of the dynamical equations, the application was straightforward and produced promising results. A linear feedback controller is used to increase the stability threshold of the purely heat conductive state so that no convection occurs despite the presence of a large thermal gradient [10,11,12,13]. Development in this area would have applications in materials processing, solidification, semiconductor melts, welding, evaporative coating, and crystal growth. Due to the nature of the Oberbeck-Boussinesq equations governing the behavior of the fluid layer, it has been easier synthesizing viable controllers for this problem than the channel flow problem.

## 2 Recent Progress

In the past three years, the design methodology developed for the two-dimensional flow problem was extended to handle a fully three-dimensional flow field. The linearized three-dimensional Navier-Stokes equations were used as the basis for a new set of fully three dimensional reduced-order controllers. Their initial application highlighted some new problems never experienced with the two-dimensional controllers, requiring us to return to the two-dimensional controllers and building up to a fully three-dimensional controller in increments. Significant success was achieved while learning some important lessons associated with the three-dimensional flow dynamic equations.

With the Rayleigh-Bénard convection problem, success has come more readily since the dynamical equations are more straightforward than the Navier-Stokes equations. Successful LQG controllers have been developed for both the linear and non-linear simulation of a heated layer of fluid.

### 2.1 A Linear Process in Wall-Bounded Shear Flows

A linear process in wall-bounded turbulent shear flows has been investigated through numerical experiments. It is shown that the linear coupling term, which enhances non-normality of the linearized Navier-Stokes equation, plays an important role in fully turbulent hence, nonlinear flows [14, Appendix A]. Near-wall turbulence is shown to decay without the linear coupling term. It is also shown that near-wall turbulence structures are not formed in their proper scales without the non-linear terms in the Navier-Stokes equation, thus indicating that the formation of the commonly observed near-wall turbulence structures are essentially non-linear, but the maintenance relies on the linear process.

This result is consistent with the analysis of Reddy and Henningson [15], who showed that non-normality of the linearized Navier-Stokes operator is a necessary condition for disturbances to grow for Reynolds number below the critical number predicted by traditional linear analysis. However, we believe this is the first direct demonstration that turbulence (non-linear disturbance) decays when the non-normality of the underlying linear operator in non-linear flows is reduced. The time scale associated with the formation is found to be smaller than the bursting process used in the optimal perturbation theory. The fact that the coupling term plays an essential role in maintaining the streamwise vortices, which have been found to be responsible for high skin-friction drag in turbulent boundary layers, suggests that an effective control algorithm for drag reduction should be aimed at reducing the effect of the coupling term in the wall region.

### 2.2 Application of Reduced-Order Controller to Turbulent Flows for Drag Reduction

The strictly two-dimensional controllers were applied successfully to a three-dimensional channel flow simulation. The controller was designed from the linearized two-dimensional

Navier-Stokes equations. Model reduction techniques were used to reduce the temporal state space representation of the dynamical equations, and then LQG/LTR control synthesis was used to derive controllers for several streamwise wavenumbers. Applied in parallel to 32 spanwise locations in the channel, the controller achieved a 10% decrease in drag reduction [16, Appendix B]). However, since no measurements were shared in the spanwise direction, the resulting shear stress varied significantly in the spanwise direction. By additional blowing and suction proportional to the spanwise variation of the streamwise-averaged wall shear stress, the shear stress oscillations in the spanwise direction was removed, and the drag was reduced by about 16% [16, Appendix B].

The linearized three-dimensional Navier-Stokes equations were then used as the basis for fully three-dimensional controllers. The Navier-Stokes equations were modified to include the control through wall-transpiration on a two-dimensional surface (bottom wall), and both spanwise and streamwise shear stress on the same two-dimensional surface was used as measurements. Since the dynamical equations now contained both the Orr-Sommerfeld and Squire modes, the question of energy amplification could now be addressed. Initial attempts proved problematic; however, a controller was successfully designed for several spanwise wavenumbers [17]. This controller managed a modest 5% reduction in drag in a DNS of a fully turbulent channel flow.

The study of the three-dimensional equations revealed several aspects, which were not apparent in the two-dimensional flow field. The assumption that the strictly streamwise wavenumber pair equations (spanwise wavenumber equaling zero) are equivalent to the two-dimensional flow equations proved to be incorrect. The original two-dimensional controllers were controlling all spanwise wavenumber systems at a given streamwise wavenumber since they had been applied in physical space (as opposed to the wave space of the decomposed system equations). In contrast, the new three-dimensional compensators were only controlling one specific wavenumber pair. Three different classes of wavenumber pairs were also discovered, each class behaving just a little differently from the others. This made it difficult to apply one single methodology and cost function to all wavenumbers.

In an effort to resolve these newly discovered issues, several spanwise three-dimensional compensators were used to augment the two-dimensional compensators developed in [9,16], replacing the *ad-hoc* scheme. This partially three-dimensional controller was able to achieve a 17% reduction in total drag with a power ratio of 30 (power saved vs. control power used).

Changing the uncertainty to also emanate from the entire flow field seemed to improve the controller. Compensators for all wavenumber pairs of the first five streamwise wavenumbers (0 to 4) were synthesized. This fully three-dimensional controller was able to achieve a 19% reduction in drag with a power ratio of 60 (Fig. 1). Efforts to improve the channel flow controller performance beyond the 15% to 20% range have been very difficult. The non-orthogonality of the eigenmodes of the dynamical system [18,19], which the compensator in many ways is designed to attenuate, is hampering our progress. The non-orthogonality of the eigenmodes is affecting the numerical calculation of the estimator and control gains. We anticipate improved controller performance once these numerical issues are resolved.

What is surprising is that 15% to 20% reduction in drag has been achieved even with

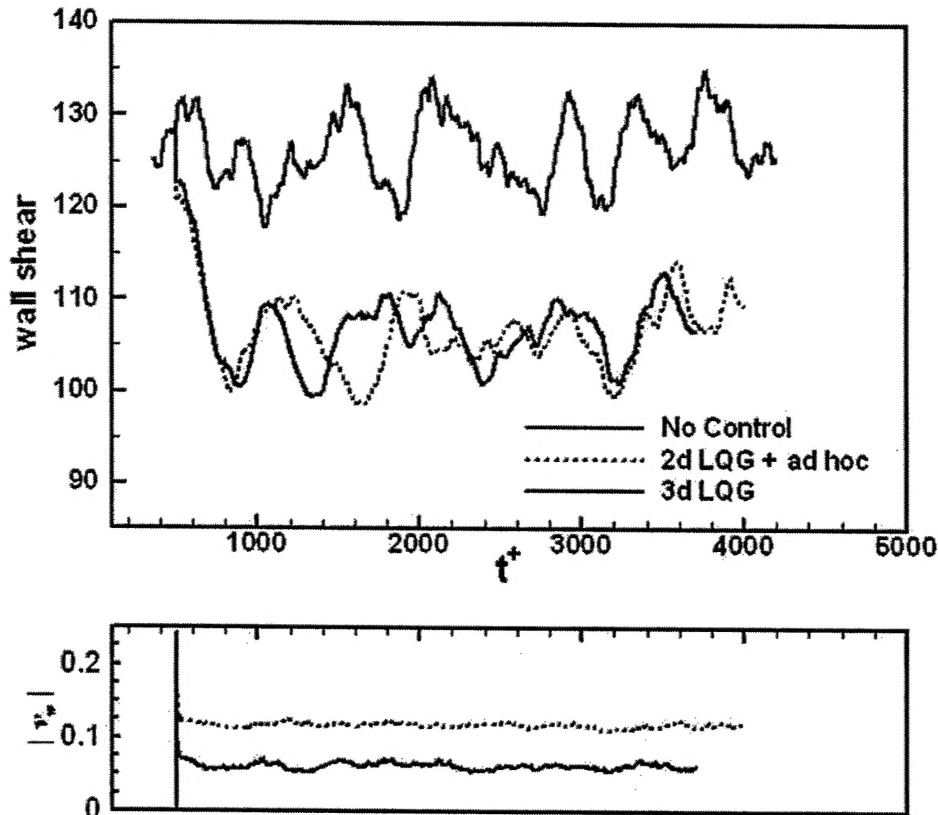


Figure 1: Controllers in DNS.

the numerical inaccuracies. However, now that we are considering changing the control cost criterion from wall-shear stress (which is measured) to other values (such as total flow field energy), the accuracy of the estimated internal state becomes paramount.

### 2.3 Robust Feedback Control of Rayleigh-Bénard Convection

Efforts with the Rayleigh-Bénard convection problem have been more straightforward. Starting with a linear plant model, we use two sensing and actuating models: the planar sensor model and the shadowgraph. By extending the planar sensor model to the multi-sensor case, a LQG controller has been developed, which stabilized the no motion state up to 14.5 times the critical Rayleigh number [20, Appendix C]. We characterize the robustness of the controller with respect to parameter uncertainties, unmodeled dynamics. Results indicate that the LQG controller provides robust performances even at high Rayleigh numbers ( $Ra$ ). Based on our results for Prandtl number of 7, we have shown that the robustness of the controller system is improved in two aspects: (i) the controller remains stable over a larger range of the parameter  $Ra$  and (ii) the robustness of the controller accommodates to a de-

gree the unmodeled dynamics and nonlinearities, as measured by gain and phase margins in the Nyquist diagram. It should be noted that although only one controller needed to be designed at  $(k^*, Ra^*)$ , this controller is implemented at each wavenumber  $k$  to span over the entire range of unstable wavenumbers. The number of sensors plays an important role in dramatically improving the robustness of the stabilization of the system operating at large  $Ra$ . Because multiple sensor planes can be easily incorporated into the planar sensor model, the performance of the planar sensor model is found to be superior to that of the shadowgraph sensor model, which only utilizes averaged temperature measurements. We have shown that the transient responses incurred at the initial time can be reduced significantly by increasing  $Ra$  to its operating value in small increments. This technique allows us to initialize the estimator at each increment of  $Ra$  and consequently avoid controller saturation. Furthermore, by making incremental changes in  $Ra$  and using a controller designed to stabilize the system in a region about the design values, the value of the maximum value of  $Ra$  could be increased further, even though there will be unstable regions formed below the stable regions in  $Ra$ .

We have also developed a fully non-linear, three-dimensional pseudospectral, time-splitting simulation of the feedback control of a layer of fluid heated from below [21, Appendix D]. Using a robust controller based on LQG synthesis, the initial condition, corresponding to a steady, large-amplitude preferred convection state at a Prandtl number of 7.0 and a Rayleigh number of 10.4, which is about six times the Rayleigh critical value, was stabilized to the zero convection state. Both sensors and actuators were assumed to be thermal-based, planar, and continuously distributed. The simulated results showed that the linear LQG controller could suppress large-amplitude steady-state convection rolls. The Green's function of the controller showed that the shape of the control action corresponds to a point measurement. Furthermore, for Rayleigh numbers below the proportional feedback control stability limit, this controller was also effective in damping out steady-state convection rolls. However, in a region very near the proportional control stability limit, direct numerical simulations demonstrated a subcritical g-type hexagonal convection induced by the proportional control action. However, well above this proportional control limit, the LQG controller was able to damp all convection.

In this phase, we have assumed that the order of the controller is equal to the order of the plant. In full numerical simulations and experiments, controller designs based on reduced-order models are more practical for implementation. The assumption that actuation is continuously distributed needs to be relaxed since in practice it will be discrete and implementation issues need to be addressed.

### 3 Schedule for Research Effort

Although we have achieved some success in designing effective controllers for turbulent channel flows, the research to date demonstrated many lingering numerical and theoretical issues which deserves further investigation. The results from the study of the Rayleigh-Bénard convection problem strongly suggests that even better results can be expected with the channel flow study. A more careful study of the numerical issues with the three-dimensional linearized Navir-Stokes equation is certainly warranted. Any further study, including more proper system identification, would require some confidence that the mathematics is being solve accurately, numerically speaking.

Furthermore, although the development of the controller design is structured with a concern for practical issues, no study has been made to what actuators and sensors could actually implement the controllers synthesized. The mathematics has been structured so that there is a great deal of parallelism built into the system, thus reducing the computation bandwidth required, but actuators and sensors will need to be investigated in terms of quantifying the uncertainties and noises associated with any mechanical device.

Although there are many issues which remain to be resolved and some that have been highlighted by this study, the current results certainly promises better results. Even with the unanswered questions and remaining numerical concerns, the controllers designed perform remarkably well in reducing the drag on a wall of a turbulent channel flow. The same design has certainly proven very effective (in simulation) in reducing the convection of a heated fluid layer.

## 4 References

1. Choi, H., Moin, P., and Kim, J., "Active Turbulence Control for Drag Reduction in Wall-Bounded Flows," *J. Fluid Mech.*, Vol. 262, p. 75, 1994.
2. Choi, H., Teman, R., Moin, P., and Kim, J., "Feedback Control for Unsteady Flow and its Application to the Stochastic Burgers Equation," *J. Fluid Mech.*, Vol. 253, p. 509, 1993.
3. Moin, P. and Bewley, T., "Application of Control Theory to Turbulence," Proc. 12th Australian Fluid Mechanics Conference, p. 109, December 10-15, Sydney, 1995.
4. Lee, C., Kim, J., and Choi, H., "Suboptimal Control of Turbulent Channel Flow for Drag Reduction," *J. Fluid Mech.*, Vol. 358, pp. 245-258, 1998.
5. Cortelezzi, L. and Speyer, J.L., "Robust Reduced-Order Controller of Laminar Boundary Layer Transitions," *Phys. Rev. E*, Vol. 58, No. 2, pp. 1906-1910, Aug. 1998.
6. Joshi, S.S., Speyer, J.L., and Kim, J., "A Systems Theory Approach to the Feedback Stabilization of Infinitesimal and Finite-Amplitude Disturbances in Plane Poiseuille Flow," *J. Fluid Mech.*, Vol. 332, p. 157, 1997.
7. Joshi, S.S., Speyer, J.L., and Kim, J., "Modeling and Control of Two-Dimensional Poiseuille Flow," Proc. 34th Conf. on Decision and Control, pp. 921-927, Dec. 1995.
8. Joshi, S.S., Speyer, J.L., and Kim, J., "Finite-Dimensional Optimal Control of Poiseuille Flow," *AIAA J. of Guidance, Control and Dynamics*, Vol. 22, No. 2, pp. 340-348, March-April 1999.
9. Cortelezzi, L., Lee, K.H., Kim, J., and Speyer, J.L., "Skin-Friction Drag Reduction via Robust Reduced-Order Linear Feedback Control," *Int'l. J. Comp. Fluid Dyn.*, Vol. 11, No. 1-2, pp. 79-92, 1998.
10. Tang, J. and Bau, H. H., "Stabilization of the No-Motion State in Rayleigh-Bénard Convection through the use of Feedback Control," *Phy. Rev. Letters*, Vol. 70, pp. 1795-1798, 1993.
11. Tang, J. and Bau, H. H., "Stabilization of the No-Motion State in the Rayleigh-Bénard Problem," *Proc. R. Soc. Lond. A*, Vol. 447, pp. 587-607, 1994.
12. Howle, L. E., "Linear Stability Analysis of Controlled Rayleigh-Bénard Convection Using Shadowgraphic Measurements," *Phy. Fluids*, Vol. 9, pp. 3111-3113, 1997.
13. Or, A. C. and Kelly, R. E., "Feedback Control of Weakly Nonlinear Rayleigh-Bénard-Marangoni Convection," *J. Fluid Mech.*, Vol. 440, pp. 27-47, 2001.
14. Kim, J. and Lim, J., "A Linear Process in Wall-Bounded Turbulent Shear Flows," *Phys. Fluids A*, Vol. 12, No. 8, pp. 1885-1888, 2000.
15. Ready, S. C. and Henningson, D. S., "Energy Growth in Viscous Channel Flows," *J. Fluid Mech.*, Vol. 252, p. 209, 1993.



16. Lee, K.H., Cortelezzi, L., Kim, J., and Speyer, J.L., "Application of Robust Reduced-Order Controller to Turbulent Flows for Drag Reduction," *Physics of Fluids*, Vol. 13, No. 5, pp. 1321-1330, 2001.
17. Kang, S.M., Ryder, V., Cortelezzi, L., and Speyer, J.L., "State-Space Formulation and Controller Design for Three-Dimensional Channel Flows," Proc. of the American Controls Conf., June 1999.
18. Butler, K.M. and Farrell, B.F., "Three-Dimensional Optimal perturbations in Viscous Shear Flow," *Phys. Fluids A*, Vol. 5, No. 11, 1993.
19. Farrell, B.F. and Ioannou, P.J., "Stochastic Forcing of the Linearized Navier-Stokes Equations," *Phys. Fluids A*, Vol. 5, No. 11, 1993.
20. Or, Arthur, Cortelezzi, Luca, and Speyer, Jason L., "Robust Feedback Control of Rayleigh-Bénard Convection," *J. Fluid Mech.*, Vol. 437, pp. 175-202, 2001.
21. Or, Arthur and Speyer, Jason L. "Active Suppression of Finite Amplitude Rayleigh-Bénard Convection," accepted to *J. Fluid Mech.*

APPENDIX A:  
A Linear Process in Wall-Bounded Turbulent Shear Flows

## LETTERS

*The purpose of this Letters section is to provide rapid dissemination of important new results in the fields regularly covered by Physics of Fluids. Results of extended research should not be presented as a series of letters in place of comprehensive articles. Letters cannot exceed four printed pages in length, including space allowed for title, figures, tables, references and an abstract limited to about 100 words. There is a three-month time limit, from date of receipt to acceptance, for processing Letter manuscripts. Authors must also submit a brief statement justifying rapid publication in the Letters section.*

## A linear process in wall-bounded turbulent shear flows

John Kim<sup>a)</sup> and Junwoo Lim

Department of Mechanical and Aerospace Engineering, University of California, Los Angeles, California 90095-1597

(Received 11 January 2000; accepted 12 April 2000)

A linear process in wall-bounded turbulent shear flows has been investigated through numerical experiments. It is shown that the linear coupling term, which enhances non-normality of the linearized Navier–Stokes system, plays an important role in fully turbulent—and hence, nonlinear—flows. Near-wall turbulence is shown to decay without the linear coupling term. It is also shown that near-wall turbulence structures are not formed in their proper scales without the nonlinear terms in the Navier–Stokes equations, thus indicating that the formation of the commonly observed near-wall turbulence structures are essentially nonlinear, but the maintenance relies on the linear process. Other implications of the linear process are also discussed. © 2000 American Institute of Physics. [S1070-6631(00)00708-X]

The transient growth due to non-normality of the eigenmodes of the linearized Navier–Stokes (N–S) equations has received much attention during the past several years (see, for example, Refs. 1–3). It has been shown that the energy of certain disturbances can grow to  $O(Re^2)$  in time proportional to  $O(Re)$ , where  $Re$  denotes Reynolds number of the flow.<sup>2</sup> It has been postulated that this transient growth, which is a linear process, can lead to transition to turbulence at a Reynolds number smaller than the critical Reynolds number, below which a classical linear stability theory based on the modal analysis predicts that all small disturbances decay asymptotically. As such, some investigators attributed this linear process as a possible cause for subcritical transition in some wall-bounded shear flows, such as plane Poiseuille flow and Couette flow.

Some investigators further postulated that the same linear process is also responsible for the observed wall-layer streaky structures in turbulent boundary layers.<sup>1,4</sup> The optimal disturbance, which has the largest transient growth according to their optimal perturbation theory, looks similar to the near-wall streamwise vortices that create the streaky structures in turbulent boundary layers. However, this optimal disturbance occupies the entire boundary layer, in contrast to the streamwise vortices in turbulent boundary layers, which are confined to the near-wall region. In order to relate their optimal perturbation theory to those structures observed in turbulent boundary layers, a time scale corresponding to the bursting process in turbulent boundary layers, which is essentially a nonlinear process, was introduced as an additional parameter.<sup>4</sup> It has been argued that the transient growth in turbulent boundary layers would be disrupted by turbulent motions on a time scale corresponding to the bursting process, which is smaller than the viscous time scale, and

hence, the globally optimal disturbance will never have a chance to grow to its maximum possible amplitude. The notion that commonly observed wall-layer structures are related to a linear process, although it is the nonlinear process that determines the proper length scale, suggests that the same linear process may play an important role in fully nonlinear turbulent boundary layers.

Other evidence that a linear process may play an important role in turbulent boundary layers can be found in the work of Joshi *et al.*<sup>5,6</sup> and others,<sup>7,8</sup> who successfully applied controllers developed based on a linear system theory to the nonlinear flow in their attempt to reduce the viscous drag in turbulent boundary layers. Bewley<sup>9</sup> applied linear optimal control theory to a nonlinear convection problem. Although it is not clear how controllers based on a linearized model work so well for nonlinear flows and it is a subject of further investigation, these results suggest that the essential dynamics of near-wall turbulence may well be approximated by a linear model.

Motivated by the above findings, we investigate the role of this linear process in fully nonlinear turbulent flows. In particular, we investigate the role of the linear coupling term (see below for its definition), which is a source of the non-normality of the eigenmodes of the linearized Navier–Stokes equations, in wall-bounded shear flows, using a turbulent channel flow as an example.

In this Letter, we shall use  $(x, y, z)$  for the streamwise, wall-normal, and spanwise coordinates, respectively, and  $(u, v, w)$  for the corresponding velocity components. Reynolds number,  $Re_\tau$ , is based on the wall-shear velocity,  $u_\tau = \sqrt{\tau_w/\rho}$ , and the channel half-width,  $h$ , where  $\tau_w = \nu dU/dy|_w$  is the mean shear stress at the wall, and  $U$ ,  $\nu$ , and  $\rho$  denote the mean velocity, viscosity, and density, re-

spectively. The superscript “+” denotes quantities nondimensionalized by  $\nu$  and  $u_\tau$ .

Representing the wall-normal velocity,  $v$ , and the wall-normal vorticity,  $\omega_y$ , in terms of Fourier modes in the streamwise ( $x$ ) and the spanwise ( $z$ ) directions, the linearized N-S equations can be written in an operator form

$$\frac{d}{dt} \begin{bmatrix} \hat{v} \\ \hat{\omega}_y \end{bmatrix} = [A] \begin{bmatrix} \hat{v} \\ \hat{\omega}_y \end{bmatrix}, \quad (1)$$

where

$$[A] = \begin{bmatrix} L_{os} & 0 \\ L_c & L_{sq} \end{bmatrix}, \quad (2)$$

and the hat denotes a Fourier-transformed quantity. Here  $L_{os}$ ,  $L_{sq}$ , and  $L_c$  represent the Orr–Sommerfeld, Squire, and the coupling operators, respectively, and defined as

$$\begin{aligned} L_{os} &= \Delta^{-1} (-ik_x U \Delta + ik_x (d^2 U / dy^2) + (1/Re) \Delta^2), \\ L_{sq} &= -ik_x U + (1/Re) \Delta, \\ L_c &= -ik_z (dU / dy), \end{aligned} \quad (3)$$

where  $k_x$  and  $k_z$  are the streamwise and spanwise wave numbers, respectively,  $k^2 = k_x^2 + k_z^2$ ,  $\Delta = \partial^2 / \partial y^2 - k^2$ , and  $U$  is the mean velocity about which the N-S equations are linearized. Note that the full nonlinear N-S equations can be written also as

$$\frac{d}{dt} \begin{bmatrix} \hat{v} \\ \hat{\omega}_y \end{bmatrix} = [A] \begin{bmatrix} \hat{v} \\ \hat{\omega}_y \end{bmatrix} + \begin{bmatrix} \mathcal{N}_v \\ \mathcal{N}_{\omega_y} \end{bmatrix}, \quad (4)$$

where all nonlinear terms are lumped into  $\mathcal{N}_v$  and  $\mathcal{N}_{\omega_y}$ . The operator  $A$  in this case, however, is a function of  $v$  and  $\omega_y$ , because  $U$  depends on  $v$  and  $\omega_y$ .

It has been shown that operator  $A$  in Eq. (2) is non-normal, and hence, its eigenmodes are nonorthogonal, thus allowing a transient growth of energy even if all individual modes are stable and decay asymptotically.<sup>1,3</sup> Note that the coupling term  $L_c$  vanishes for two-dimensional (2-D) disturbances ( $k_z = 0$ ), and therefore, there is no coupling between  $v$  and  $\omega_y$  for 2-D disturbances. For 3-D disturbances, however,  $v$  evolves independently, but  $\omega_y$  is forced by  $v$  through the coupling term. It should be noted that  $L_{os}$  itself is not self-adjoint, and hence, 2-D disturbances can have a transient growth, but it was shown that 3-D disturbances have much larger transient growth due to the coupling term, which causes larger non-normality. In the present study, we concentrate on the role of the coupling term in fully nonlinear turbulent flows, using a fully developed turbulent channel flow as an example.

In order to investigate the role of the coupling term in fully turbulent flows, we proceed to solve the following modified nonlinear equations:

$$\frac{d}{dt} \begin{bmatrix} \hat{v} \\ \hat{\omega}_y \end{bmatrix} = \begin{bmatrix} L_{os} & 0 \\ 0 & L_{sq} \end{bmatrix} \begin{bmatrix} \hat{v} \\ \hat{\omega}_y \end{bmatrix} + \begin{bmatrix} \mathcal{N}_v \\ \mathcal{N}_{\omega_y} \end{bmatrix}. \quad (5)$$

This modified system can be viewed as representing a synthetic turbulent flow without the coupling term, or a turbu-

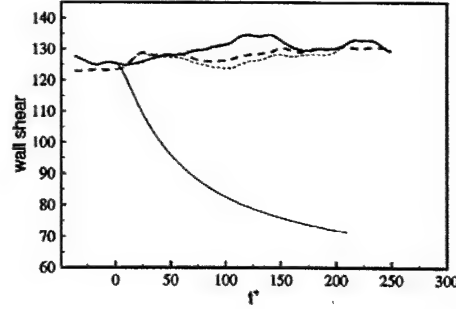


FIG. 1. Time evolution of mean shear at wall: —, upper wall; ---, lower wall. Thick lines are for a regular channel flow, while thin lines are for a channel flow with  $L_c = 0$  in the upper half of the channel starting from  $t^+ = 0$ .

lent flow with control by which the coupling term is suppressed. For instance, surface blowing and suction activated to eliminate (reduce) the spanwise variation of  $v$  (i.e.,  $\partial v / \partial z$ ) could eliminate (reduce) the effect of the coupling term.

A spectral channel code similar to that of Kim *et al.*<sup>10</sup> was used to solve the above modified nonlinear equations. To further contrast the role of the coupling term, we used the modified N-S equations only in the upper half of the channel and the regular N-S equations in the lower half of the channel. We used the same Reynolds number ( $Re_\tau = 100$ ) and grid ( $32 \times 65 \times 32$  in  $x, y, z$ ) as Lee *et al.*<sup>11</sup>

In the first numerical experiment, we used a regular turbulent velocity field obtained by Lee *et al.* as our initial field. Starting from this initial field, we integrated in time to see how the turbulent flow in the upper half of the channel evolves in the absence of the coupling term. Time evolution of the mean shear at both walls is shown in Fig. 1, which illustrates a drastic reduction in the wall shear without the coupling term. Several snapshots of the velocity field are shown in Fig. 2, where contours of streamwise vorticity in a

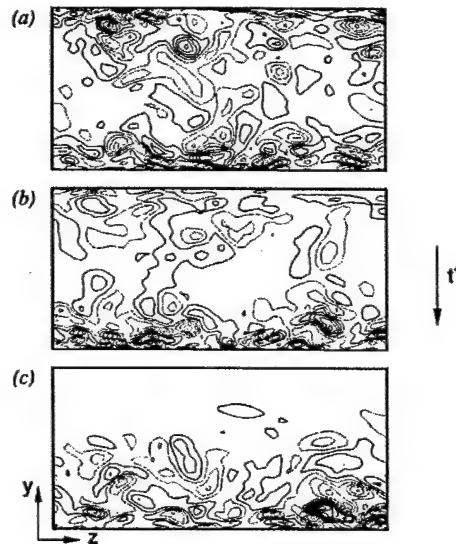


FIG. 2. Contours of streamwise vorticity in  $y$ - $z$  plane: (a)  $t^+ = 0$ ; (b)  $t^+ = 20$ ; (c)  $t^+ = 200$ .  $-80 < \omega_x < 80$  with 18 contour levels. Note that  $L_c = 0$  only in the upper-half of the channel.

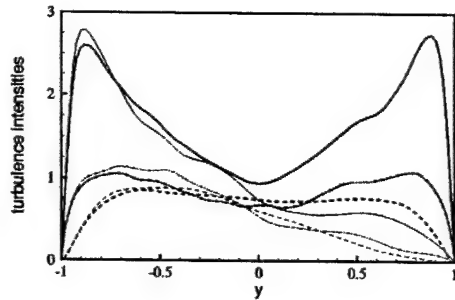


FIG. 3. Root-mean-square turbulence intensities: —,  $\sqrt{u^2}$ ; ---,  $\sqrt{v^2}$ ; - · -,  $\sqrt{w^2}$ . Thick lines are for  $t^+ = 0$ , while thin lines are for  $t^+ = 180$ .

$y$ - $z$  plane are shown to illustrate the effect of the coupling term on turbulence structures. It is evident that streamwise vortices quickly disappear without the coupling term. The reduction of the wall shear in conjunction with the disappearance of the streamwise vortices is a common feature of many drag-reduced turbulent flows.<sup>11</sup> Turbulence intensities shown in Fig. 3 indicate drastic reductions without the coupling term.

In the second numerical experiment, we used an initial velocity field consisting of the same mean velocity as the first experiment but with random disturbances, and hence, there are no organized turbulence structures present initially. A divergence-free white-noise spectrum was used for this purpose. The amplitude was chosen such that neither they decay too quickly (too small) nor they cause a numerical instability due to non-smoothness of the initial condition (too

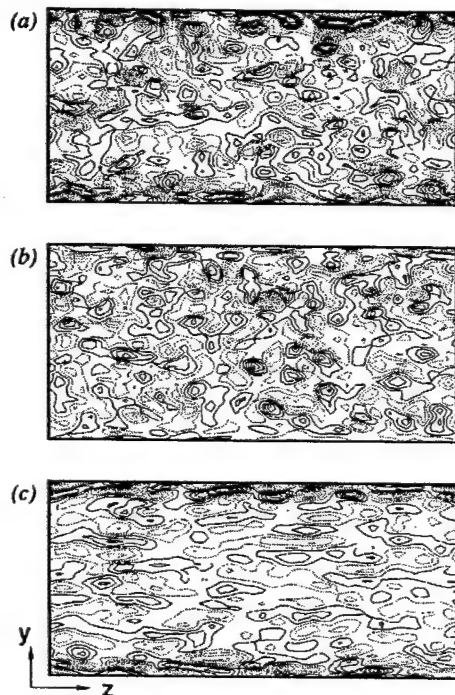


FIG. 4. Contours of streamwise vorticity in  $y$ - $z$  plane at  $t^+ = 20$ , started from an initial random field: (a) Case 1, regular turbulent flow; (b) Case 2, without the linear coupling term,  $L_c$ ; (c) Case 3, without the nonlinear terms. Contour levels are the same as Fig. 2.

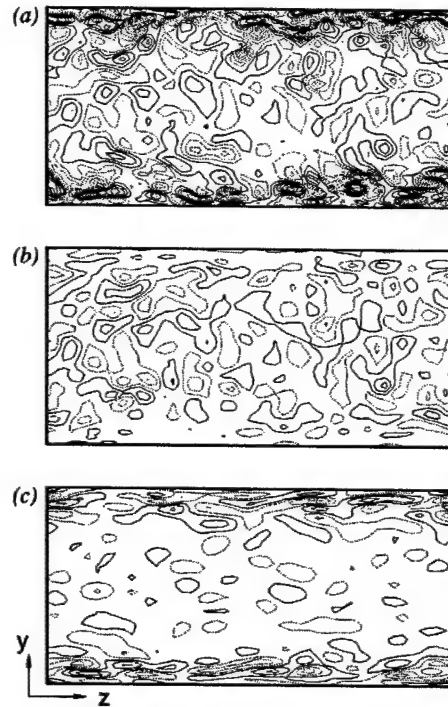


FIG. 5. Contours of streamwise vorticity in  $y$ - $z$  plane at  $t^+ = 40$ , started from a random initial field. See figure caption in Fig. 4 for legend.

large). Starting with the same random initial field, three different simulations were carried out: Case 1, with the full nonlinear N-S equations (i.e., regular turbulent flow); Case 2, with N-S equations without the linear coupling term; Case 3, with N-S equations without the nonlinear terms (i.e., linearized N-S). The purpose of these simulations is to investigate whether the linear coupling term is indeed responsible for formation of the streamwise vortices and near-wall streaks, and if so, whether the time scale associated with the formation of these structures corresponds to the bursting process ( $t^+ \approx 100$ ), as hypothesized by Butler and Farrell.<sup>4</sup>

Time evolution of the three velocity fields is shown in Figs. 4–6 with streamwise vorticity contours in a  $y$ - $z$  plane. Organized structures are discernible in all three cases as early as  $t^+ = 20$  (Fig. 4), but they look different from each other. For Case 3 (without the nonlinear terms), the structures that appear from the structureless random initial condition have larger spanwise scales than those in the regular flow (Figs. 4 and 5). For Case 2 (without the linear coupling term), the vortical structures appear briefly (Fig. 4) but disappear quickly, especially in the wall region (Figs. 5 and 6), since they cannot be maintained without the linear coupling term as demonstrated in the first experiment mentioned above. For Case 1, the time for these structures to appear is shorter than that implied by the optimal disturbance mechanism of Butler and Farrell.<sup>4</sup> Note that the structures in Case 3 are already substantially different from those in Case 1 at  $t^+ = 40$ , indicating that the effect of nonlinear terms is felt much earlier than the eddy turnover time ( $t^+ \approx 100$ ) as proposed by Butler and Farrell.<sup>4</sup> The present result is also consistent with Jiménez and Pinelli,<sup>12</sup> who showed that the formation of streaky structures can be prevented by damping

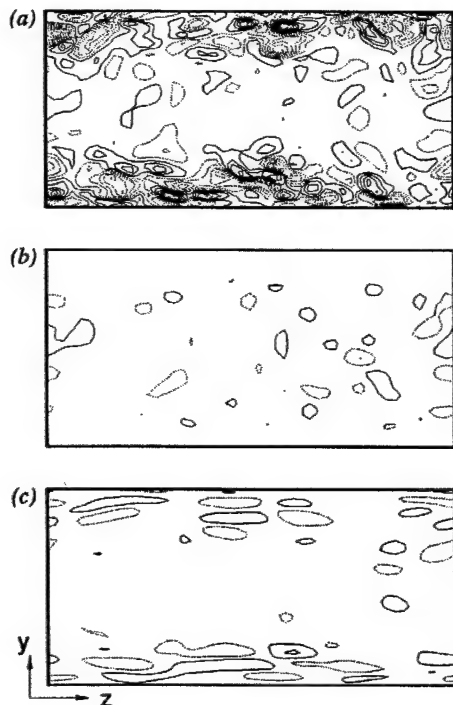


FIG. 6. Streamwise contours in  $y$ - $z$  plane at  $t^+ = 80$ , started from a random initial field. See figure caption in Fig. 4 for legend.

$(\overline{v\omega_z})$  [the  $(\overline{\quad})$  indicates streamwise average], which is related to the linear coupling term. While both results clearly demonstrate the essential role of the linear coupling term in the formation and maintenance of the wall-layer streaks, while the present work also indicates that a nonlinear mechanism is responsible for producing the proper streak spacing.

We have used several different initial conditions to determine whether the above results depend on initial conditions, but found no such evidence. It thus appears that both the nonlinear terms and the linear coupling term are necessary for the formation and maintaining of these structures at their proper scale. The nonlinear terms are necessary for the formation of streamwise vortices and the linear coupling term is necessary to generate the wall-layer streaks, the instability of which in turn strengthen the streamwise vortices through a nonlinear process. In the absence of either mechanism, turbulence ceases to exist. The result of this second experiment is consistent with Hamilton *et al.*<sup>13</sup> and Waleffe and Kim<sup>14</sup> in that the formation of the streamwise vortices is a result of a nonlinear process.

We have demonstrated that the linear process associated with the coupling term plays an important role even in fully nonlinear wall-bounded turbulent shear flows. Near-wall streamwise vortices, which play the essential role in the dynamics of wall-bounded shear flows, are seen to be formed but cannot be sustained without the coupling term.

This result is consistent with the analysis by Henningson and Reddy<sup>15</sup> who showed that non-normality of the linearized Navier-Stokes operator is a necessary condition for disturbances to grow for Reynolds number below the critical Reynolds number predicted by the traditional linear stability analysis. However, we believe this is the first direct demon-

stration that turbulence (nonlinear disturbance) decays when the non-normality of the underlying linear operator in non-linear flows is reduced. The time scale associated with the formation is found to be smaller than the bursting process used in the optimal perturbation theory. The fact that the coupling term plays an essential role in maintaining the streamwise vortices, which have been found to be responsible for high skin-friction drag in turbulent boundary layers, suggests that an effective control algorithm for drag reduction should be aimed at reducing the effect of the coupling term in the wall region. In fact, the opposition control used by Choi *et al.*<sup>16</sup> can be viewed as a control scheme trying to reduce the effect of the coupling term by suppressing the spanwise variation of  $v$  in the wall region. It should be interesting to design a control algorithm that directly accounts for the coupling term in a cost function to be minimized.

A portion of this work was carried out while the first author was visiting the Isaac Newton Institute for Mathematical Sciences at Cambridge University. This work has been supported by the Air Force Office of Scientific Research (F49620-97-10276, Dr. Marc Jacobs). The computer time has been provided by the San Diego Supercomputer Center.

<sup>a</sup>Author to whom correspondence should be addressed. Telephone: (310)825-4393; Fax: (310)206-4830. Electronic mail: jkim@seas.ucla.edu

<sup>1</sup>K. M. Butler and B. F. Farrell, "Three-dimensional optimal perturbations in viscous shear flow," *Phys. Fluids A* **4**, 1637 (1992).

<sup>2</sup>B. F. Farrell and P. J. Ioannou, "Stochastic forcing of the linearized Navier-Stokes equations," *Phys. Fluids A* **5**, 2600 (1993).

<sup>3</sup>S. C. Reddy and D. S. Henningson, "Energy growth in viscous channel flows," *J. Fluid Mech.* **252**, 209 (1993).

<sup>4</sup>K. M. Butler and B. F. Farrell, "Optimal perturbations and streak spacing in wall-bounded turbulent shear flow," *Phys. Fluids A* **5**, 774 (1993).

<sup>5</sup>S. S. Joshi, J. L. Speyer, and J. Kim, "A systems theory approach to the feedback stabilization of infinitesimal and finite-amplitude disturbances in plane Poiseuille flow," *J. Fluid Mech.* **332**, 157 (1997).

<sup>6</sup>S. S. Joshi, J. L. Speyer, and J. Kim, "Finite dimensional optimal control of Poiseuille flow," *J. Guid. Control Dyn.* **22**, 340 (1999).

<sup>7</sup>L. Cortez, K. H. Lee, J. Kim, and J. L. Speyer, "Skin-friction drag reduction via robust reduced-order linear feedback control," *Int. J. Comp. Fluid Dyn.* **11**, 79 (1998).

<sup>8</sup>K. H. Lee, *A Systems Theory Approach to Control of Transitional and Turbulent Flows*, Ph.D. dissertation, University of California at Los Angeles (1999).

<sup>9</sup>T. R. Bewley, "Linear control and estimation of nonlinear chaotic convection: Harnessing the butterfly effect," *Phys. Fluids* **11**, 1169 (1999).

<sup>10</sup>J. Kim, P. Moin, and R. K. Moser, "Turbulence statistics in fully developed channel flow at low Reynolds number," *J. Fluid Mech.* **177**, 133 (1987).

<sup>11</sup>C. Lee, J. Kim, D. Babcock, and R. Goodman, "Application of neural networks to turbulence control for drag reduction," *Phys. Fluids* **9**, 1740 (1997).

<sup>12</sup>J. Jiménez and A. Pinelli, "The autonomous cycle of near-wall turbulence," *J. Fluid Mech.* **389**, 335 (1999).

<sup>13</sup>J. M. Hamilton, J. Kim, and F. Waleffe, "Regeneration mechanisms of near-wall turbulence structures," *J. Fluid Mech.* **287**, 317 (1995).

<sup>14</sup>F. Waleffe and J. Kim, "How streamwise rolls and streaks self-sustain in a shear flow," in *Self-Sustaining Mechanisms of Wall Turbulence*, edited by R. L. Panton (Computational Mechanics Publications, Southampton, UK and Boston, USA, 1997), pp. 309-332.

<sup>15</sup>D. S. Henningson and S. C. Reddy, "On the role of linear mechanism in transition to turbulence," *Phys. Fluids* **6**, 1396 (1994).

<sup>16</sup>H. Choi, P. Moin, and J. Kim, "Active turbulence control for drag reduction in wall-bounded flows," *J. Fluid Mech.* **262**, 75 (1994).

APPENDIX B:  
Application of Robust Controller  
to Turbulent Flows for Drag Reduction



## Application of reduced-order controller to turbulent flows for drag reduction

Keun H. Lee, Luca Cortelezzi,<sup>a)</sup> John Kim,<sup>b)</sup> and Jason Speyer

*Department of Mechanical & Aerospace Engineering, University of California, Los Angeles, California 90095*

(Received 18 April 2000; accepted 29 January 2001)

A reduced-order linear feedback controller is designed and applied to turbulent channel flow for drag reduction. From the linearized two-dimensional Navier–Stokes equations a distributed feedback controller, which produces blowing/suction at the wall based on the measured turbulent streamwise wall-shear stress, is derived using model reduction techniques and linear-quadratic-Gaussian/loop-transfer-recovery control synthesis. The quadratic cost criterion used for synthesis is composed of the streamwise wall-shear stress, which includes the control effort of blowing/suction. This distributed two-dimensional controller developed from a linear system theory is shown to reduce the skin friction by 10% in direct numerical simulations of a low-Reynolds number turbulent nonlinear channel flow. Spanwise shear-stress variation, not captured by the distributed two-dimensional controller, is suppressed by augmentation of a simple spanwise *ad hoc* control scheme. This augmented three-dimensional controller, which requires only the turbulent streamwise velocity gradient, results in a further reduction in the skin-friction drag. It is shown that the input power requirement is significantly less than the power saved by reduced drag. Other turbulence characteristics affected by these controllers are also discussed. © 2001 American Institute of Physics. [DOI: 10.1063/1.1359420]

### I. INTRODUCTION

Much attention has been paid to the drag reduction in turbulent boundary layers. Skin friction drag constitutes approximately 50%, 90%, and 100% of the total drag on commercial aircraft, underwater vehicles, and pipelines, respectively.<sup>1</sup> The decrease of skin friction, therefore, entails a substantial saving of operational cost for commercial aircraft and submarines. Recent reviews<sup>1–3</sup> summarize achievements and open questions in boundary layer control.

With the notion that near-wall streamwise vortices are responsible for high skin friction in turbulent boundary layers, Choi *et al.*<sup>4</sup> manipulated the near-wall turbulence by applying various wall actuations. They achieved a 20% skin-friction reduction in a turbulent channel flow by applying a wall transpiration equal and opposite to the wall-normal velocity component measured at  $y^+ = 10$ . This control is shown to effectively make the streamwise vortices weaker. However, it is not easily implementable since it is difficult to place sensors inside the flow field. Other attempts at weakening the near-wall streamwise vortices have been made by imposing spanwise oscillation of the wall<sup>5</sup> and using external body force.<sup>6</sup> These methods, however, require a large amount of input energy. A reduction in skin friction must be accompanied with the required input energy much less than the energy saved by the reduction.

A systematic approach, not relying on physical intuition, has been tried in the past. A suboptimal control, which de-

termines the optimal control input by minimizing the cost functional for a short time interval, was successfully applied to the stochastic Burger's equation.<sup>7</sup> Bewley and Moin<sup>8</sup> extended the suboptimal control to a turbulent channel flow. This method, however, requires information about the whole flow field and excessive computation, so that it is impossible or at best extremely difficult to implement. It is necessary to develop a control scheme that utilizes easily measurable quantities.

Lee *et al.*<sup>9</sup> developed a neural network control algorithm that approximates the correlation between the wall-shear stresses and the wall actuation and then predicts the optimal wall actuation to produce the minimum value of skin friction. They also produced a simple control scheme from this neural network control, which determines the actuation as the sum of the weighted spanwise wall-shear stress,  $\partial w / \partial y|_w$ . Recently, Koumoutsakos<sup>10</sup> reported a substantial drag reduction obtained by applying a feedback control scheme based on the measurement and manipulation of the wall vorticity flux. Furthermore, he showed that the strength of unsteady mass transpiration actuators can be derived explicitly by inverting a system of equations.

Other systematic controls<sup>11–17</sup> have been developed by exploiting the tools recently developed in the control community.<sup>18–21</sup> Joshi *et al.*<sup>11–13</sup> and Bewley and Liu<sup>14</sup> developed an integral feedback controller, a linear quadratic (LQ) controller, and an  $\mathcal{H}_\infty$  controller (worst-case controller) to successfully stabilize unstable disturbances in transitional flow. In particular, Cortelezzi and Speyer<sup>15</sup> introduced the multi-input–multi-output (MIMO) linear-quadratic-Gaussian (LQG)/loop-transfer-recovery (LTR) synthesis,<sup>22</sup> combined with model reduction techniques, for designing an optimal linear feedback controller. This controller successfully sup-

<sup>a)</sup>Present address: Department of Mechanical Engineering, McGill University, Montreal, Quebec, Canada; electronic mail: cortlz@ametista.mecheng.mcgill.ca

<sup>b)</sup>Author to whom correspondence should be addressed. Telephone: (310) 825-4393; fax: (310) 206-4830; electronic mail: jkim@seas.ucla.edu

pressed near-wall disturbances, thus preventing a transition in two-dimensional laminar channel flows. This reduced-order controller<sup>16</sup> was applied to two-dimensional nonlinear transitional flows, illustrating that the controller designed from the linear model works remarkably well in nonlinear flows.

Our purpose in the present study is to develop a realistic robust optimal controller that systematically determines the wall actuation, in the form of blowing and suction at the wall, relying only on a measured streamwise velocity gradient to reduce skin friction in a fully developed turbulent channel flow. A dynamic representation of the flow field is required for controller design. Due to the complexity and nonlinearity of the Navier–Stokes equations, it is difficult to derive model-based controllers. Therefore, the linearized Navier–Stokes equations for Poiseuille flow are used as an approximation of the flow field and form the basis of system modeling. Several investigators (e.g., Farrel and Ioannou,<sup>23</sup> Kim and Lim,<sup>24</sup> to name a few) have shown that linearized models have a direct relevance to turbulent flows. A reduced-order controller has been designed based on this model and applied to linear and nonlinear transitional flows.<sup>15–17</sup> Encouraged by these results, in this paper we apply this distributed two-dimensional controller to a direct numerical simulation of turbulent channel flow at a low Reynolds number. We then augment our two-dimensional distributed controller by including an *ad hoc* control scheme to attenuate the residual disturbances in the spanwise direction.

In Sec. II, we derive the state-space equations from the linearized two-dimensional Navier–Stokes equations. In Sec. III, we reduce the order of the state-space equations and derive a reduced-order two-dimensional controller by using LQG/LTR synthesis. In Sec. IV, we construct and apply the distributed two-dimensional controller based on the linearized Navier–Stokes equations to a fully developed turbulent channel flow at  $Re_\tau = 100$ , where  $Re_\tau$  is the Reynolds number based on the wall-shear velocity,  $u_\tau$ , and the half-channel height,  $h$ . In Sec. V, this distributed two-dimensional controller augmented with a simple *ad hoc* control scheme is applied to the same flow. In Sec. VI, we present turbulence statistics associated with the controlled flows followed by conclusions in Sec. VII.

In this paper, we use  $(u, v, w)$  to represent the velocity components in the streamwise ( $x$ ), wall-normal ( $y$ ), and spanwise ( $z$ ) directions, respectively.

## II. THE STATE-SPACE EQUATIONS

One of the goals in the present study is to reduce the size of the controller. A controller with a large number of states is of no practical interest in engineering applications because of the amount of hardware and computer power necessary to compute a real-time control law. Consequently, it is crucial to reduce the order of the controller.

Figure 1 shows the configuration of the turbulent channel flow equipped with the controller tested for our study. Low-order controllers are usually preferred to high-order one because of the lower cost of hardware construction as well as the less computation time necessary to provide the control

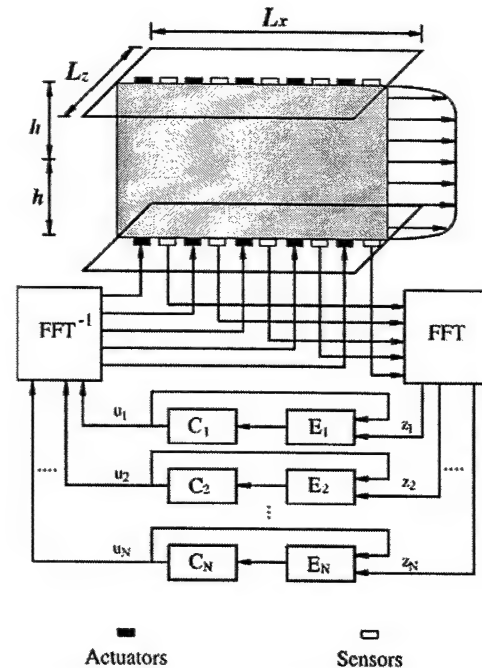


FIG. 1. Schematic representation of turbulent channel flow equipped with sensors and actuators distributed in the streamwise direction in each  $z$  plane.

input. Hence, we slice the channel with  $xy$  planes equally spaced in the  $z$  direction in order to reduce the order of the controller. We then construct the distributed two-dimensional controller by applying the two-dimensional controller developed from the linearized two-dimensional Navier–Stokes equations<sup>15</sup> to each plane. It is shown<sup>16</sup> that the two-dimensional controller is effectively able to reduce the skin-friction drag of the finite-amplitude disturbances in a two-dimensional channel flow.

We follow the same derivation of the state-space equation as given in Cortez et al.<sup>16</sup> We give a brief outline here for completeness; the interested reader is referred to Cortez et al.<sup>16</sup> for details. The wall transpiration is applied to both top and bottom walls in a fully developed turbulent channel flow. For simplicity, though, we derive the state-space equations assuming that blowing and suction is applied only at the bottom wall. The application of blowing and suction to both walls is a trivial extension.

We consider two-dimensional incompressible Poiseuille flow in a periodic channel of streamwise length,  $L_x$ , and channel height,  $2h$ . The undisturbed velocity field has a parabolic profile with centerline velocity  $U_c$ . The linearized two-dimensional Navier–Stokes equations can be written in terms of the perturbation streamfunction,  $\psi$ ,

$$(\partial_t + U \partial_x) \Delta \psi - U'' \psi_x = Re^{-1} \Delta \Delta \psi, \quad (1)$$

where all variables are normalized with  $U_c$  and  $h$  and  $Re = U_c h / \nu$  is the Reynolds number.

To suppress perturbations evolving within the bottom boundary layer, we apply blowing and suction at the bottom wall (see Fig. 1). For simplicity, we assume that the actuators are continuously distributed. The corresponding boundary conditions are

$$\psi_x|_{y=-1} = -v_w(x, t), \quad \psi_y|_{y=\pm 1} = \psi|_{y=1} = 0, \quad (2)$$

where the control function  $v_w$  indicates blowing and suction at the bottom wall. We impose the wall transpiration of zero net mass flux.

To detect the near-wall disturbances, we measure the gradient of the streamwise disturbance velocity at given point  $x = x_i$  along the bottom wall (see Fig. 1),

$$z(x_i, t) = \psi_{yy}|_{y=-1}. \quad (3)$$

In other words, we measure the first term of the disturbance wall-shear stress,  $\tau_{yx} = \text{Re}^{-1}(\psi_{yy} - \psi_{xx})|_{y=-1}$ . The second term of the wall-shear stress is zero in the uncontrolled case and is known in the controlled case.

We define a performance index  $\tilde{J}$ , or cost criterion, to design a controller for the LQG ( $\mathcal{H}_2$ ) problem. Since we are interested in suppressing the disturbance wall-shear stress,  $\tau_{yx}$ , we define

$$\tilde{J} = \lim_{t_f \rightarrow \infty} \int_t^{t_f} \int_0^L (\psi_{yy}^2 + \psi_{xx}^2)|_{y=-1} dx dt. \quad (4)$$

The integrand represents the cost of the disturbance wall-shear stress,  $\tau_{yx}$ , being different from zero. Moreover, the integrand implicitly accounts for the cost of implementing the control itself. There are two reasons to minimize the cost of the control. In any engineering application the energy available to drive the controller is limited, and a large control action may drive the system away from the region where the linear model is valid.

By using the same procedure described in Cortez et al.,<sup>16</sup> Eqs. (1)–(3) are converted into the state-space equations:

$$\frac{dx}{dt} = \mathbf{A}x + \mathbf{B}u, \quad z = \mathbf{C}x + \mathbf{D}u, \quad (5)$$

with the initial condition  $x(0) = x_0$ , where  $x$  is the internal state vector,  $u$  is the control vector,  $z$  is the measurement vector. Matrices  $\mathbf{A}, \mathbf{B}, \mathbf{C}$  contain the dynamics of the two-dimensional plane Poiseuille flow, actuators, and sensors, respectively. Matrix  $\mathbf{D}$  contains the coupling between sensors and actuators. The cost criterion, Eq. (4), becomes

$$\tilde{J} = \lim_{t_f \rightarrow \infty} \int_t^{t_f} [z^T z + u^T \mathbf{F}^T \mathbf{F} u] dt, \quad (6)$$

where the superscript  $T$  denotes a transposed quantity. The matrix  $\mathbf{F}$  is obtained by spectrally decomposing the last term in the cost criterion, Eq. (4).

The advantage of the present formulation is that the whole problem decouples with respect to the wave number when Eqs. (5) and (6) are transformed into Fourier space in the streamwise direction. All matrices in Eqs. (5) and (6) are block diagonal, which allows the above state-space system into equivalent  $N$  state-space subsystems.<sup>25</sup> For a given wave number,  $\alpha$ , the state-space subsystem equations are

$$\frac{dx_\alpha}{dt} = \mathbf{A}_\alpha x_\alpha + \mathbf{B}_\alpha u_\alpha, \quad z_\alpha = \mathbf{C}_\alpha x_\alpha + \mathbf{D}_\alpha u_\alpha, \quad (7)$$

with the initial condition  $x_\alpha(0) = x_{\alpha 0}$ . It can be shown that the cost criterion, Eq. (6), also decouples with respect to the wave number (otherwise the wave number decoupling is not possible while the system itself is decoupled), and we obtain  $N$  performance indexes. For a given wave number,  $\alpha$ , the cost criterion is defined as

$$\tilde{J}_\alpha = \lim_{t_f \rightarrow \infty} \mathcal{J}_\alpha = \lim_{t_f \rightarrow \infty} \int_t^{t_f} [z_\alpha^T z_\alpha + u_\alpha^T \mathbf{F}_\alpha^T \mathbf{F}_\alpha u_\alpha] dt. \quad (8)$$

Consequently, the design of a two-dimensional controller for the system, Eq. (5), with a specified cost criterion, Eq. (6), has been reduced to the independent design of  $N$  single-wave number controllers for the subsystems, Eq. (7), along with Eq. (8).

### III. MODEL REDUCTION AND CONTROLLER DESIGN

In this section we derive a lower-order two-dimensional controller in two steps.<sup>15</sup> First, we construct a lower-order model of Eq. (7), and subsequently, design a single-wave number controller for the reduced-order model. To obtain a lower-order model, we transform Eq. (7) into a Jordan canonical form. The matrices  $\hat{\mathbf{A}}_\alpha, \hat{\mathbf{B}}_\alpha, \hat{\mathbf{C}}_\alpha, \mathbf{D}_\alpha$  that describe the dynamics of the reduced-order model are obtained from the matrices,  $\mathbf{A}_\alpha, \mathbf{B}_\alpha, \mathbf{C}_\alpha, \mathbf{D}_\alpha$  in the Jordan canonical form by retaining rows and columns corresponding to equally well controllable and observable states. The overcaret denotes the quantities associated with the reduced-order model.

Although a rigorous mathematical framework for the design of disturbance attenuation ( $\mathcal{H}_\infty$ ) linear controllers is provided by the control synthesis theory,<sup>18,19</sup> for this study LQG ( $\mathcal{H}_2$ ) synthesis is preferred. A brief review will be given in a self-contained manner to provide the necessary governing equations for closed-loop stability analysis.<sup>20</sup>

The LQG problem for each wave number  $\alpha$  is formulated as a stochastic optimal control problem described by equations

$$\dot{\hat{x}}_\alpha = \hat{\mathbf{A}}_\alpha \hat{x}_\alpha + \hat{\mathbf{B}}_\alpha u_\alpha + \Gamma_\alpha w_\alpha, \quad (9)$$

$$\dot{\hat{z}}_\alpha = \hat{\mathbf{C}}_\alpha \hat{x}_\alpha + \mathbf{D}_\alpha u_\alpha + v_\alpha, \quad (10)$$

where  $\Gamma_\alpha$  is an input matrix,  $w_\alpha$  and  $v_\alpha$  are both white noise processes with zero means and autocorrelation functions,

$$\begin{aligned} E[w_\alpha(t)w_\alpha^T(\tau)] &= \mathbf{W}_\alpha \delta(t - \tau), \\ E[v_\alpha(t)v_\alpha^T(\tau)] &= \mathbf{V}_\alpha \delta(t - \tau), \end{aligned} \quad (11)$$

where  $E[\cdot]$  is the expectation operator averaging over all underlying random variables and  $\delta(t - \tau)$  is the delta function. Note that  $\mathbf{W}_\alpha$  and  $\mathbf{V}_\alpha$ , the power spectral densities, will be chosen here as design parameters to enhance system performance. An additional comment on the controller design process will be given at the end of this section.

The LQG controller is determined by finding the control action  $u_\alpha(Z_t)$ , where  $Z_t = \{z(\tau); 0 \leq \tau \leq t\}$  is the measurement history, which minimizes the cost criterion,

$$J_\alpha = \lim_{t_f \rightarrow \infty} \frac{1}{t_f - t} \times E \left( \int_t^{t_f} (\hat{\mathbf{x}}_\alpha^T \mathbf{Q}_\alpha \hat{\mathbf{x}}_\alpha + 2 \hat{\mathbf{x}}_\alpha^T \mathbf{N}_\alpha \mathbf{u}_\alpha + \mathbf{u}_\alpha^T \mathbf{R}_\alpha \mathbf{u}_\alpha) d\tau \right), \quad (12)$$

subject to the stochastic dynamics system model equations Eqs. (10)–(11). Note that, from Eqs. (7)–(8),  $\mathbf{Q}_\alpha = \hat{\mathbf{C}}_\alpha^T \hat{\mathbf{C}}_\alpha$ ,  $\mathbf{N}_\alpha = \hat{\mathbf{C}}_\alpha^T \mathbf{D}_\alpha$ , and  $\mathbf{R}_\alpha = \mathbf{D}_\alpha^T \mathbf{D}_\alpha + \mathbf{F}_\alpha^T \mathbf{F}_\alpha$ . The division by  $(t_f - t)$  ensures that the cost criterion remains finite in the presence of uncertainties in the infinite-time problem ( $t_f \rightarrow \infty$ ). Note that Eq. (12) can include Eq. (8), where

$$J_\alpha = \lim_{t_f \rightarrow \infty} \frac{1}{t_f - t} E[J_\alpha], \quad (13)$$

and the limit in Eq. (8) is explicitly denoted in Eq. (13). Note that even though the time interval is infinite, the time response is still measured by the eigenvalues of the closed-loop system. We consider the infinite-time problem with time-invariant dynamics because the controller gains become constants.

By nesting the conditional expectation with respect to  $Z_t$  within the unconditional expectation of Eq. (13), i.e.,  $E[J_\alpha] = E[E[J_\alpha/Z_t]]$ , where  $E[\cdot/Z_t]$  denotes the expectation ( $\cdot$ ) conditioned on  $Z_t$ , the cost criterion can be written as

$$J_\alpha = \lim_{t_f \rightarrow \infty} \frac{1}{t_f - t} \times E \left( \int_t^{t_f} [\tilde{\mathbf{x}}_\alpha^T \mathbf{Q}_\alpha \tilde{\mathbf{x}}_\alpha + 2 \tilde{\mathbf{x}}_\alpha^T \mathbf{N}_\alpha \mathbf{u}_\alpha + \mathbf{u}_\alpha^T \mathbf{R}_\alpha \mathbf{u}_\alpha + \text{tr}(\mathbf{P}_\alpha)] d\tau \right), \quad (14)$$

where  $\tilde{\mathbf{x}}_\alpha = E[\hat{\mathbf{x}}_\alpha/Z_t]$  is the conditional mean estimate of the state  $\hat{\mathbf{x}}$  and  $\mathbf{P}_\alpha$  is the conditional error variance. This cost criterion is now minimized subject to the estimation equations discussed below. Note that  $\mathbf{P}_\alpha$  does not depend on the control [see Eq. (18) below] and, therefore, does not enter into the optimization process.

The solution to the regulator problem<sup>20</sup> is a compensator composed of a state reconstruction process, known here as a filter (in the no-noise case it is known as an observer) in cascade with a controller (see Fig. 1, where  $E_i$  is the estimator and  $C_i$  is the controller). The state estimate (conditional mean)  $\tilde{\mathbf{x}}_\alpha$  is governed by the so-called Kalman filter as

$$\begin{aligned} \dot{\tilde{\mathbf{x}}}_\alpha &= \hat{\mathbf{A}}_\alpha \tilde{\mathbf{x}}_\alpha + \hat{\mathbf{B}}_\alpha \mathbf{u}_\alpha + \hat{\mathbf{L}}_\alpha \mathbf{v}_\alpha, \\ \mathbf{v}_\alpha &= \hat{\mathbf{z}}_\alpha - \tilde{\mathbf{z}}_\alpha = \hat{\mathbf{C}}_\alpha (\hat{\mathbf{x}}_\alpha - \tilde{\mathbf{x}}_\alpha) + \mathbf{v}_\alpha. \end{aligned} \quad (15)$$

If the reduced-order system were the actual system, then  $\mathbf{v}_\alpha$  in Eq. (15) is correct. When the actual system is considered and the filter is implemented based on the reduced-state space,  $\mathbf{z}$  rather than  $\hat{\mathbf{z}}$  is the measurement and the filter residual becomes

$$\mathbf{v}_\alpha = \mathbf{z}_\alpha - \hat{\mathbf{C}}_\alpha \tilde{\mathbf{x}}_\alpha - \mathbf{D}_\alpha \mathbf{u}_\alpha. \quad (16)$$

The Kalman gain matrix  $\mathbf{L}_\alpha$ , constructed to trade the accuracy of the new measurements against the accuracy of the state propagated from the system dynamics, is given by

$$\hat{\mathbf{L}}_\alpha = \mathbf{P}_\alpha \hat{\mathbf{C}}_\alpha^T \mathbf{V}_\alpha^{-1}, \quad (17)$$

where  $\mathbf{P}_\alpha$  is the error variance in the statistical problem.

In the infinite-time stationary formulation, the error  $\mathbf{P}_\alpha$  is the solution to the algebraic Riccati equation (ARE),

$$\hat{\mathbf{A}}_\alpha \mathbf{P}_\alpha + \mathbf{P}_\alpha \hat{\mathbf{A}}_\alpha^T + \Gamma_\alpha \mathbf{W}_\alpha \Gamma_\alpha^T - \mathbf{P}_\alpha \hat{\mathbf{C}}_\alpha^T \mathbf{V}_\alpha^{-1} \hat{\mathbf{C}}_\alpha \mathbf{P}_\alpha = 0. \quad (18)$$

If the system is  $(\hat{\mathbf{A}}_\alpha, \hat{\mathbf{C}}_\alpha)$  observable and  $(\hat{\mathbf{A}}_\alpha, \hat{\mathbf{B}}_\alpha)$  controllable, then  $\mathbf{P}_\alpha$  is positive definite. Under these assumptions, it can be shown that the difference between the internal state  $\hat{\mathbf{x}}_\alpha$  and the estimate state  $\tilde{\mathbf{x}}_\alpha$ , i.e., the error,

$$\mathbf{e}_\alpha = \hat{\mathbf{x}}_\alpha - \tilde{\mathbf{x}}_\alpha, \quad (19)$$

goes to zero as time goes to infinity. In other words, the evolution equation,

$$\dot{\mathbf{e}}_\alpha = \mathbf{A}_f \mathbf{e}_\alpha + \hat{\mathbf{L}}_\alpha \mathbf{v}_\alpha + \Gamma_\alpha \mathbf{w}_\alpha, \quad (20)$$

is stable, i.e., all the eigenvalues of the matrix,

$$\mathbf{A}_f = \hat{\mathbf{A}}_\alpha - \hat{\mathbf{L}}_\alpha \hat{\mathbf{C}}_\alpha, \quad (21)$$

have a negative real part.

Minimizing the infinite-time cost function  $J$ , Eq. (14) subject to Eq. (15) yields the following control law:

$$\mathbf{u}_\alpha = -\hat{\mathbf{K}}_\alpha \tilde{\mathbf{x}}_\alpha, \quad (22)$$

where

$$\hat{\mathbf{K}}_\alpha = \mathbf{R}_\alpha^{-1} (\hat{\mathbf{B}}_\alpha^T \mathbf{S}_\alpha + \mathbf{N}_\alpha), \quad (23)$$

and  $\mathbf{S}_\alpha$  is the solution of the algebraic Riccati equation (ARE),

$$\hat{\mathbf{A}}_\alpha \mathbf{S}_\alpha + \mathbf{S}_\alpha \hat{\mathbf{A}}_\alpha^T + \mathbf{Q}_\alpha - (\mathbf{S}_\alpha \hat{\mathbf{B}}_\alpha + \mathbf{N}_\alpha) \mathbf{R}_\alpha^{-1} (\hat{\mathbf{B}}_\alpha^T \mathbf{S}_\alpha + \mathbf{N}_\alpha) = 0. \quad (24)$$

It should be remarked that the control gain matrix  $\hat{\mathbf{K}}_\alpha$  is determined from functions only of the known dynamics coefficients  $(\hat{\mathbf{A}}_\alpha, \hat{\mathbf{B}}_\alpha)$  and the weighting in the cost criterion  $(\mathbf{Q}_\alpha, \mathbf{R}_\alpha)$ , and not the statistic of the input  $(\mathbf{V}_\alpha, \mathbf{W}_\alpha)$ . Consequently,  $\hat{\mathbf{K}}_\alpha$  is determined from a performance index as Eq. (12), independent of the stochastic inputs. If  $(\hat{\mathbf{A}}_\alpha, \hat{\mathbf{B}}_\alpha)$  is controllable and  $(\hat{\mathbf{A}}_\alpha, \mathbf{Q}_\alpha^{1/2})$  observable, then the loop coefficient matrix,

$$\mathbf{A}_c = \hat{\mathbf{A}}_\alpha - \hat{\mathbf{K}}_\alpha \hat{\mathbf{B}}_\alpha, \quad (25)$$

is stable and  $\mathbf{S}_\alpha$  is positive definite. The controllable and observable conditions can be weakened to stabilizable and detectable.<sup>21</sup>

When we combine the estimator and the regulator together, the dynamic system composed of the controlled process and filter becomes

$$\begin{pmatrix} \dot{\mathbf{e}}_\alpha \\ \dot{\tilde{\mathbf{x}}}_\alpha \end{pmatrix} = \begin{bmatrix} \mathbf{A}_f & \mathbf{0} \\ \hat{\mathbf{L}}_\alpha \hat{\mathbf{C}}_\alpha & \mathbf{A}_c \end{bmatrix} \begin{pmatrix} \mathbf{e}_\alpha \\ \tilde{\mathbf{x}}_\alpha \end{pmatrix} + \begin{pmatrix} \hat{\mathbf{L}}_\alpha \mathbf{v}_\alpha + \Gamma_\alpha \mathbf{w}_\alpha \\ \hat{\mathbf{L}}_\alpha \mathbf{v}_\alpha \end{pmatrix}. \quad (26)$$

Note that any choice of two between  $\mathbf{e}_\alpha$ ,  $\hat{\mathbf{x}}_\alpha$ , and  $\tilde{\mathbf{x}}_\alpha$  produce the same dynamics because they are algebraically related by



Eq. (19). Under the above controllability and observability assumptions,  $A_f$  and  $A_c$  have only stable eigenvalues if optimal gains  $\hat{L}_\alpha$  and  $\hat{K}_\alpha$  of Eqs. (17) and (23) are used. If the actual linear system is used, then  $x_\alpha$  and the reduced-order state estimate  $\tilde{x}_\alpha$  are used to form the closed-loop dynamic system rather than that given in Eq. (26). The eigenvalues of the dynamical matrix now dictate the system stability and will differ from the ideal case of Eq. (26).

The parameters used in our LQG design are now addressed. Since the power spectral density is not known, for simplicity of the design we consider  $V_\alpha$  and  $W_\alpha$  to be of the form  $V_\alpha = \beta I$  and  $W_\alpha = \rho I$ , where  $\beta$  and  $\rho$  are scalar and  $I$  is an identity matrix. Only the ratio of  $\beta$  and  $\rho$  is important. Furthermore, by choosing  $\Gamma_\alpha = \hat{B}_\alpha$ , loop-transfer recovery (LTR) of the LQG controller to full-state feedback<sup>18</sup> guarantees that robust performance occurs when the process noise power spectral density goes to infinity, i.e.,  $\rho \rightarrow \infty$ , provided there exists no nonminimal-phase zero in the plant. In our case, there are no nonminimal-phase zeros and robust performance means approximately obtaining 60° of phase margin and 6 db of the gain margin. Note that the choice of  $\Gamma_\alpha = \hat{B}_\alpha$  implies that the noise is generated along the wall as is the control and could be interpreted as due to wall roughness. Furthermore, the values of  $\rho$  and  $\beta$  were determined by tuning the controller in the presence of turbulent flow. The degree of loop transfer recovery varied from controller to controller.

As described above using LQG/LTR assumes that the uncertainty is at the wall and effects the dynamics in the same way as the control. Since the system has the same controllability with respect to both the control and disturbances, state-space reduction for controller design was straightforward. This is in contrast to  $\mathcal{H}_\infty$  control used by Bewley and Liu,<sup>14</sup> where uncertainty is assumed uniformly throughout the channel. Since controllability of the disturbances is different from that of the control, model reduction may not be straightforward. Furthermore, robustness in terms of traditional measures of the gain and phase margin in control engineering are also obtained by using LQG/LTR. For these reasons LQG/LTR is used for the present study instead of the unstructured uncertainty  $\mathcal{H}_\infty$  controllers.

Figure 1 links the mathematical formulation to its computational implementation by summarizing in a block diagram the control strategy described above. The two-dimensional distributed controller can be programmed in a computer routine whose input is a matrix containing the gradients of the streamwise velocity component and whose output is a matrix containing the blowing and suction at the wall. Each column of the measurement matrices contains the gradients of the streamwise velocity component along the wall at a given spanwise location. Each column is processed in parallel by a fast Fourier transform (FFT) and converted into  $z_\alpha$ 's. Each single-wave number controller, Eqs. (9)–(10), is integrated in time by, for example, a third-order low-storage Runge–Kutta scheme. The  $u_\alpha$ 's are computed in parallel. An inverse FFT converts  $u_\alpha$ 's into the columns of the matrix containing the blowing and suction at the wall along the streamwise direction. This routine can be embedded in

any Navier–Stokes solver able to handle time-dependent boundary conditions for the control of three-dimensional channel flows.

Figure 1 also provides the basic architecture for the potential implementation of the present distributed two-dimensional controller in practical engineering applications. For instance, the gradients of the streamwise velocity component can be measured by microelectromechanical-systems (MEMS) hot-film sensors.<sup>26</sup> For each  $xy$  plane, analog-to-digital converters (A/D) and digital signal processors (DSP) convert the measured gradients into  $z_\alpha$ 's. Each single-wave number controller, Eqs. (9)–(10), is replaced by a microprocessor, and parallel computation produces  $u_\alpha$ 's. A DSP and a digital-to-analog converter (D/A) produce the actuating signal in each  $xy$  plane. A variety of actuators, such as synthetic jets, microbubble actuators, and thermal actuators, can mimic small-amplitude blowing and suction at the wall.<sup>26</sup>

Although the structure of this compensator is simplified by the parallel computation (for all spanwise directions), it does require processing of all the sensor measurements (for all streamwise directions). The controller is essentially centralized because all information is used and the actuators are activated spatially over the assumed channel. Controllers based explicitly on the spatial distribution of the control, suggested by Bamieh *et al.*,<sup>27</sup> show that there is a spatial decay rate. Our controller can be constructed to represent a discrete form of their controller and given the spatial decay rate for our configuration, i.e., the size of the channel could be chosen consistent with that decay rate. Nevertheless, our representation allows a significant decrease in on-line computation by identifying the Fourier modes and the number of states associated with those modes that best reduce turbulence as discussed in the next section.

#### IV. PERFORMANCE OF A TWO-DIMENSIONAL CONTROLLER

For the purpose of testing the performance of a controller, we performed direct numerical simulations of a turbulent channel flow at  $Re_\tau = 100$ . A spectral code was used with a computational domain of  $(4\pi, 2, 4\pi/3)$  and a grid resolution of  $(32, 65, 32)$  in the  $(x, y, z)$  directions. The numerical technique used in this study is essentially the same as that of Kim *et al.*<sup>28</sup> except that the time advancement for the nonlinear terms is a third-order Runge–Kutta (RK3) method. The second-order accurate Crank–Nicolson (CN) method is used for the linear terms.

We designed a distributed two-dimensional controller in two steps. First, we designed reduced-order controllers for two-dimensional Poiseuille flow in a periodic channel of streamwise length  $L_x = 4\pi$  at  $Re = 5000$ , which has the same mean wall-shear stress as turbulent channel flow at  $Re_\tau = 100$ . Subsequently, we fine-tuned the single-wave number reduced-order controllers in order to minimize the magnitude of the Fourier coefficients of the wall-shear stresses in turbulent channel flow at  $Re_\tau = 100$ . We used  $N = 32$  and  $M = 60$  in this linear model flow. Controllers operate at both top and bottom walls in parallel. If the two-dimensional controllers without model reduction were applied at each  $z$

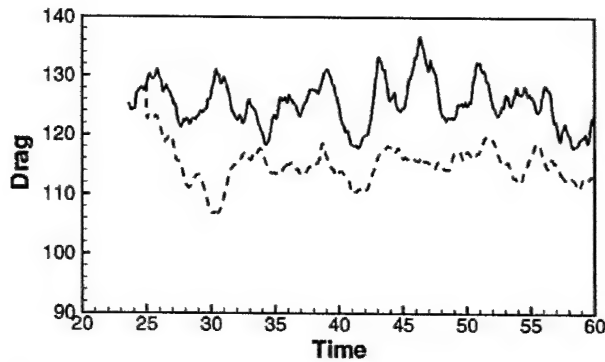


FIG. 2. Time history of the drag for the controlled and uncontrolled flows: ---, controlled flow; —, uncontrolled flow.

plane, then the order of the ensemble of controllers would be  $64 \times 3904 = 249\,856$ . Using the model reduction technique previously described, we designed eight single-wave number controllers of order 12, corresponding to the eight lowest wave numbers. Since we use the eight lowest single-wave number controllers in our simulation, the combined order of the controllers is  $64 \times 96 = 6144$ . It represents a state-space reduction of about 97.5%, with respect to the full-order system.

Figure 2 shows the time history of the drag in the uncontrolled and controlled flows. Drag is measured by the mean value of the wall-shear stresses averaged over each top and bottom wall. This two-dimensional control yields about a 10% drag reduction. Choi *et al.*<sup>4</sup> reported that the in-phase  $u$  control measured at  $y^+ = 10$  also gives a 10% drag reduction. This in-phase streamwise velocity at the wall causes a similar effect,  $du'/dy|_w = 0$ , which is the to-be-minimized target of our cost criterion in our two-dimensional controller. Note that this observed drag reduction is a byproduct since our controller is designed to suppress the fluctuations of the streamwise wall-shear stress, not the mean wall-shear stress. Note also the sudden drop in the drag as soon as the controller is switched on at  $t = 25$ . This transient phenomena is also observed in other studies.<sup>8,9</sup>

Figure 3 compares the magnitude of Fourier coefficients of the wall-shear stresses in the controlled and uncontrolled flows. The wall-shear stresses are measured at the bottom wall at a given spanwise location. Figures 3(a) and 3(b) show the comparisons corresponding to wave numbers  $k_x = 0.5$  and  $k_x = 1.0$ , respectively. Both figures show an order-of-magnitude reduction between the controlled and uncontrolled cases. The magnitude of the Fourier coefficients of wall-shear stress decreases very quickly as soon as the controller is activated at  $t = 25$ . These results indicate that our distributed two-dimensional linear reduced-order controller suppresses disturbance wall-shear stress remarkably well, even in a fully developed turbulent flow. The high wave number components of the wall-shear stress in Fig. 3(c) do not show any reduction since only the lowest eight single-wave number controllers (up to  $k_x = 4.0$ ) are used in the control of flow. Examinations of other spanwise locations show similar results.

Contours of the disturbance wall-shear stresses at the

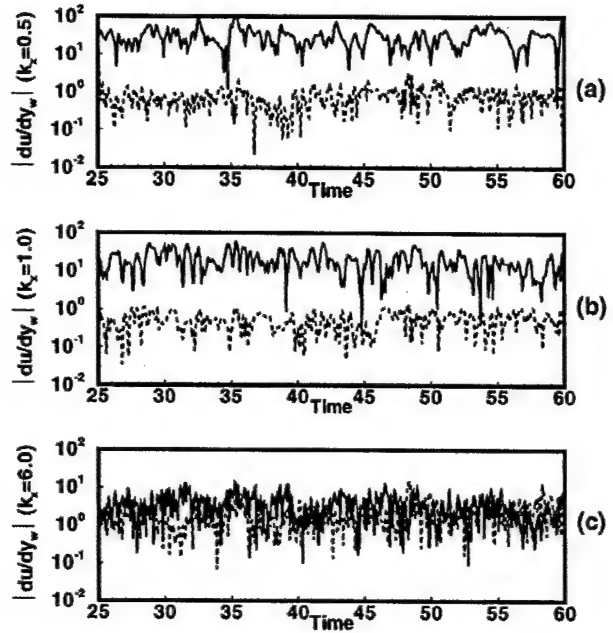


FIG. 3. Time history of the magnitude of the Fourier coefficients of the wall-shear stresses measured at the bottom wall at a given spanwise location for the controlled and uncontrolled flows: —, uncontrolled flow; ---, controlled flow. (a)  $k_x = 0.5$ , (b)  $k_x = 1.0$ , and (c)  $k_x = 6.0$ .

bottom wall in the controlled and uncontrolled flows at  $t = 30$  are shown in Fig. 4. Contours for the uncontrolled flow show the usual elongated regions of low- and high-shear stress. Note that contours for the controlled flow show the dramatic effect of the distributed two-dimensional controller. The long streaky wall-shear stress region spans almost the entire streamwise direction, indicating that the low wave number components (except the zero wave number that we do not control) are completely suppressed, which is consistent with Fig. 3. The remaining spanwise variations, i.e., the alternating regions of high- and low-shear stress, are due to

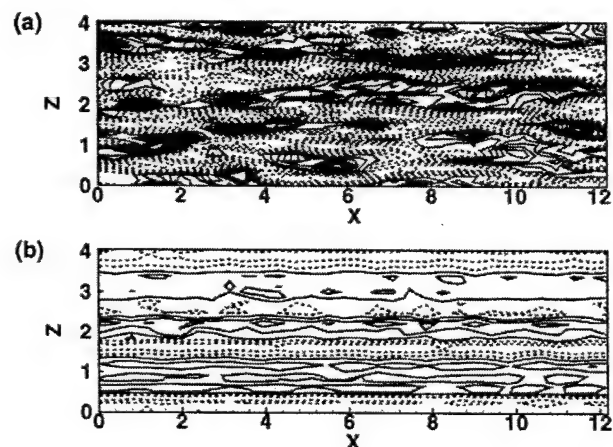


FIG. 4. Contours of disturbance wall-shear stresses at the bottom wall at  $t = 30$ : (a) uncontrolled flow; (b) 2-D-controlled flow. Negative contours are dashed.

the fact that the two-dimensional controllers distributed along the streamwise direction are operated independently from one  $z$  plane to another.

The above results demonstrate that our distributed two-dimensional controller designed from the linear model works remarkably well in suppressing near-wall disturbances in the fully developed turbulent flow. The reduction of fluctuating wall-shear stress led to drag reduction. However, this distributed two-dimensional controller has a limited impact on the total drag since it cannot control the spanwise variation of the wall-shear stress. In the next section an augmentation to the distributed two-dimensional controller is presented and implemented.

## V. AUGMENTED THREE-DIMENSIONAL CONTROLLER

In the previous section, successful control of fully developed turbulent channel flow has been obtained by applying a distributed two-dimensional controller. However, it has been observed that this controller does not account for the spanwise variations of fluid motion. An augmentation to the distributed two-dimensional controller that accommodates the three-dimensional characteristics of a fully developed turbulent flow is developed in this section.

A simple *ad hoc* control augmentation scheme is introduced in an attempt to capture the remaining spanwise variations of the controlled flow. This additional control, which generates blowing/suction to attenuate the spanwise variation of the wall-shear stress, is given as follows:

$$v_{ad}(z) = C \left( \frac{\partial u}{\partial y} \Big|_w^{(x,z)} - \frac{\partial u}{\partial y} \Big|_w^x \right), \quad (27)$$

where  $\partial u / \partial y|_w^{(x,z)}$  and  $\partial u / \partial y|_w^x$  are the streamwise velocity gradients averaged over the  $xz$  plane and the  $x$  direction, respectively, and  $C$  is a constant to be adjusted for the best performance. The subscript *ad* indicates the *ad hoc* control, and  $v_{ad}$  is a function of only  $z$ . Therefore, the new control input is defined by

$$v_w(x, z) = v_{ad} + v_{2-D}, \quad (28)$$

where  $v_{2-D}$  is the actuation velocity generated by the distributed two-dimensional controller used in the previous section.

Using the distributed two-dimensional controller augmented with this *ad hoc* control scheme, the control of the fully developed turbulent flow with  $Re_\tau = 100$  increased drag reduction to about 17%, as shown in Fig. 5. As before, the turbulent flow is left free to evolve without any wall actuation until  $t = 25$ . As soon as the controller is activated at  $t = 25$ , the drag drops sharply within a very small time period. The constant,  $C$ , in Eq. (27) is adjusted such that the root-mean-square (rms) value of the actuation is maintained at  $0.1u_\tau$ , where  $u_\tau$  is the wall-shear velocity for the uncontrolled flow. We have found empirically that  $C$  between  $0.05u_\tau$  and  $0.2u_\tau$  gives a similar performance. An introduction of this simple control augmentation enhances the drag reduction, indicating that more sophisticated controllers that best take into account the three-dimensionality of turbulent flow may produce even more efficient suppression of skin-friction drag.

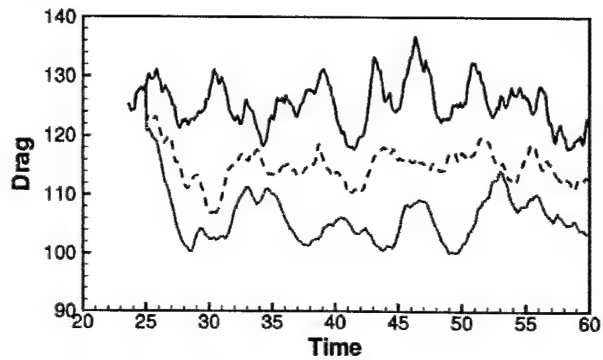


FIG. 5. Time history of the drag for the controlled and uncontrolled flows: —, uncontrolled flow; ---, 2-D-controlled flow; ···, *ad hoc*-controlled flow.

Figure 6 presents the comparison of contours of the disturbance wall-shear stresses at the bottom wall between the *ad hoc* controlled flow and the uncontrolled flow at  $t = 30$ . Compared to Fig. 4, additional effort in the spanwise direction,  $v_{ad}$ , removes the pronounced peak-valley variation of the wall-shear stress that is observed in the controlled flow with the distributed two-dimensional controllers [see Fig. 4(b)]. Note that the high wave number components of the wall-shear stress are persistently sustained because of the lowest eight single-wave number controllers adopted in the control of flow.

## VI. TURBULENCE STATISTICS

Some turbulence statistics of the flow field associated with the two controllers applied in this paper were examined to investigate the effect of the controllers on turbulence. All statistical quantities were averaged over a sufficiently long interval of time as well as over the planes parallel to the wall. For simplicity, the flows controlled by the distributed two-dimensional controller only and the distributed two-

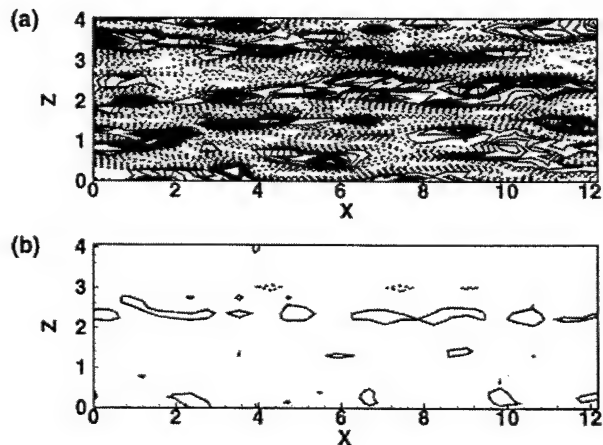


FIG. 6. Contours of disturbance wall-shear stresses at the bottom wall at  $t = 30$ : (a) uncontrolled flow; (b) *ad hoc*-controlled flow. Negative contours are dashed.



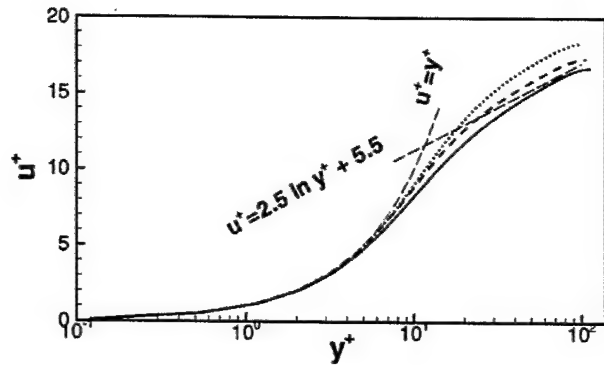


FIG. 7. Mean-velocity profiles:  $\cdots$ , *ad hoc*-controlled flow;  $---$ , 2-D-controlled flow;  $—$ , uncontrolled flow.

dimensional controller augmented with the *ad hoc* control scheme are called “2-D-controlled” and “*ad hoc*-controlled” flows, respectively.

The mean velocity profiles normalized by the actual wall-shear velocities are shown in Fig. 7 for three different channel flows. These profiles show the same trend shown in the Choi *et al.*<sup>4</sup> drag-reduced flow: the slope of the log law for controlled flows remains the same while the mean velocity itself is shifted upward in the log-law region.

The root-mean-square (rms) values of turbulent velocity fluctuations are shown in Fig. 8 and compared to those of the

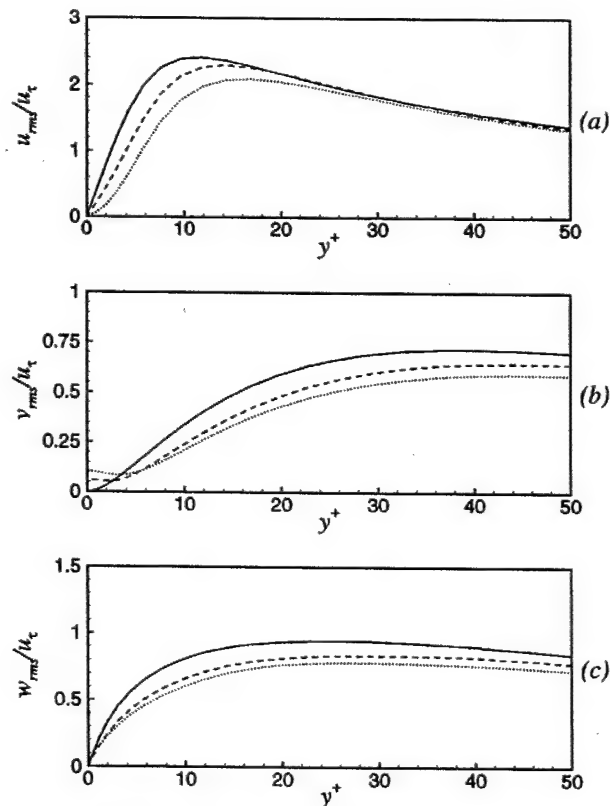


FIG. 8. Root-mean-square values of turbulent velocity fluctuations normalized by the wall-shear velocity,  $u_\tau$  for the uncontrolled flow:  $—$ , uncontrolled flow;  $---$ , 2-D-controlled flow;  $\cdots$ , *ad hoc*-controlled flow.

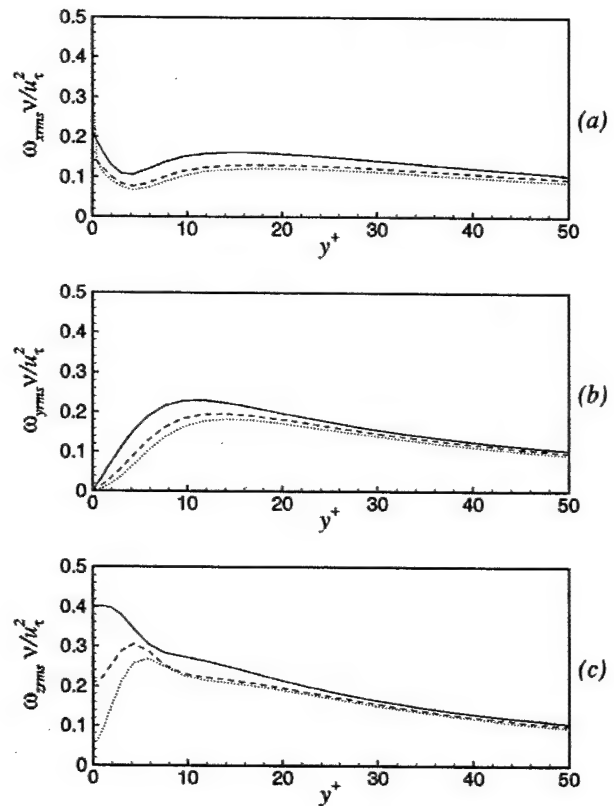


FIG. 9. Root-mean-square values of vorticity fluctuations normalized by the wall-shear velocity in wall coordinates:  $—$ , uncontrolled flow;  $---$ , 2-D-controlled flow;  $\cdots$ , *ad hoc*-controlled flow.

uncontrolled flow. Note that all quantities in this figure are normalized by the wall-shear velocity of the uncontrolled flow. The controllers reduce the value of turbulent intensity significantly throughout the channel, especially for the wall-normal and spanwise components. The reduction of these quantities in the *ad hoc*-controlled flow is greater than that in the 2-D-controlled flow. The increase in  $v_{rms}$  very near the wall is due to the control input. A similar feature is also observed by Choi *et al.*<sup>4</sup> and Lee *et al.*<sup>9</sup> Both controllers mitigate the rms of spanwise velocity fluctuation throughout the channel compared to that in uncontrolled flow. However, the introduction of  $v_{ad}$  in Eq. (27) causes this value to increase very close to the wall, which also leads to an increase in the streamwise vorticity at the wall.

Root-mean-square values of vorticity fluctuations for the controlled flows are compared with those for the uncontrolled flow in Fig. 9. All components of vorticity fluctuations are significantly reduced throughout the channel. Very close to the wall, however, the increase of streamwise vorticity in the *ad hoc*-controlled flow is due to the streamwise vorticity built at the wall by the *ad hoc* controller. The high streamwise vorticity at the wall slows the sweeping motion of high-momentum fluid induced by the streamwise vorticity away from the wall, thus resulting in a significant reduction in skin friction. A similar feature is also observed in Lee *et al.*<sup>9</sup> Note that the streamwise vorticity at the wall for the 2-D-controlled flow, however, is less than that for the uncon-

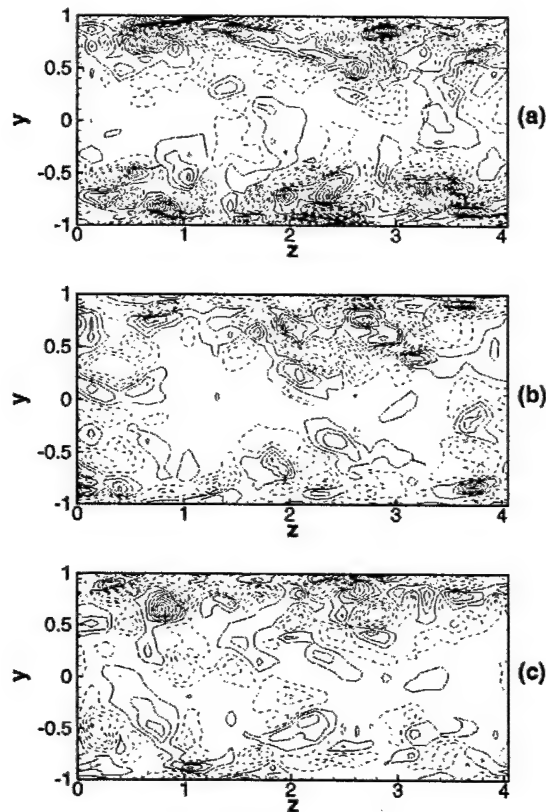


FIG. 10. A comparison of streamwise vorticity contours in a  $yz$  plane between controlled and uncontrolled flows: (a) uncontrolled flow; (b) 2-D controlled flow; (c) *ad hoc*-controlled flow. Negative contours are dashed.

trolled flow. The reduction of  $\omega_z$  is a direct consequence of the controller, which was designed to reduce  $\partial u'/\partial y|_w$ . The reduction of  $\omega_y$  also indicates that our controllers weaken the strength of near-wall streaks. This also decreases the streak instability, which is shown to be responsible for regenerating the near-wall streamwise vortices.<sup>29,30</sup>

Figure 10 compares the streamwise vorticity fields in the uncontrolled and controlled flows. The strength of the near-wall streamwise vorticity for the controlled flows are greatly attenuated due to the wall transpiration produced by the controllers. It is discernible that the *ad hoc* controller diminishes the streamwise vorticity substantially more. The reduction of the strength of the streamwise vorticity has also been observed by Lee *et al.*<sup>9</sup> While Lee *et al.*<sup>9</sup> suppressed the streamwise vorticity field with the physical understanding that the control based on the weighted sum of  $\partial w/\partial y|_w$  can prevent the physical eruption at the wall, the present controllers attenuate the streamwise vorticity strength by minimizing the streamwise disturbance wall-shear stress systematically. The present results further support the notion that a successful attenuation of the near-wall streamwise vortices results in a significant reduction in skin-friction drag.<sup>4</sup>

## VII. CONCLUSIONS

A reduced-order linear feedback control based on a distributed two-dimensional controller design is applied to a

turbulent channel flow. A controller based on a reduced model of the linearized Navier–Stokes equations for a laminar Poiseuille flow was designed by using LQG ( $\mathcal{H}_2$ )/LTR synthesis. This controller was implemented using input measurements that are the gradients of the streamwise disturbance velocity and output controls that are the blowing and suction at the wall.

First, we applied the distributed two-dimensional controller to both walls of a turbulent channel flow at  $Re_\tau = 100$ . Eight single-wave number controllers corresponding to eight lowest wave numbers, reducing the order of the controller about 2.5% of the order of the full size system, are applied to attain a skin-friction reduction of 10% with respect to the uncontrolled turbulent flow. Next, a simple *ad hoc* augmented control scheme of the distributed two-dimensional controller is introduced to capture the three-dimensionality of turbulent flow. The control of fully developed turbulent flow by the distributed two-dimensional controller augmented by the *ad hoc* control scheme produces a 17% reduction in skin-friction drag. Motivated by this result, we are currently developing controllers to more efficiently account for the three-dimensionality of turbulent flow.

It should be noted that the present controller, which is based on a reduced-order linear system, has achieved its design objective, i.e., minimization of the wall-shear stress disturbances, quite remarkably when applied to the nonlinear flow. It was anticipated that the reduction of disturbances would also lead to a substantial reduction of the mean wall-shear stress. Unfortunately, this turned out not to be the case, suggesting that some other cost functions should be explored. By comparing with our previous results,<sup>9,31</sup> it was found that the present controller is not as effective in diminishing the strength of the streamwise vortices in the buffer layer, which was the primary target for other controllers, but achieved its design goal by mainly affecting the region very close to the wall. In this regard, minimization of the total disturbance energy in the flow field<sup>32</sup> or minimization of the linear coupling term<sup>24</sup> appears to be a good candidate to be explored. Whether either of these cost criterion is indeed controllable in nonlinear flows, however, remains to be investigated.

This study is carried out at low Reynolds number. Whether our controller, based on the reduced-order linear model, would work in other turbulent flows, should be drawn from real experiments or simulations at high Reynolds number. However, we expect that it should work equally well for high Reynolds number flow since our controller, derived from LQG/LTR synthesis, recovers the robustness of LQR, whose characteristics have been partially tested over the different Reynolds number flows.<sup>33</sup>

The statistics of controlled and uncontrolled flows are compared. The mean velocity profile is shifted upward in the log region, a typical characteristic of drag-reduced flow. Velocity and vorticity fluctuations as well as Reynolds shear stress (not shown) are significantly reduced due to the blowing/suction generated by the controller. However, a major change is confined to the wall region. Instantaneous flow fields show that the distributed two-dimensional controller

attenuates and modifies the streaky structure of the boundary layer. Streaks are observed to span the entire streamwise direction with velocity variations in the spanwise direction. These variations are substantially reduced by the augmented controller.

The three-dimensional aspect of the distributed two-dimensional controller by the augmentation of the *ad hoc* control further reduced the skin-friction drag. This three-dimensional controller produces secondary streamwise vorticity at the wall, which slows the sweeping motions of high-momentum fluid induced by the streamwise vorticity away from the wall. This induced retarding of the primary streamwise vorticity leads to additional drag reduction, which was also observed in Choi et al.<sup>4</sup>

Regarding the scaling factor  $C$  in Eq. (27), we found an optimal value of  $C$  that yields the blowing/suction of  $0.1u_\tau$ . With this optimal  $C$ , the augmented controller generates wall transpiration with a rms value of about  $0.12u_\tau$ . The required power input per unit area to the system,  $p_w v_w + 0.5\rho v_w^3 \approx 0.1\rho u_\tau^3$ , is significantly less than the power saved from the drag reduction,  $\Delta C_f / C_f \tau_w U_c \approx 3.2\rho u_\tau^3$ , where  $p_w$ ,  $\rho$ ,  $C_f$ ,  $\tau_w$ , and  $U_c$  are the wall pressure, density, skin-friction coefficient, averaged wall-shear stress, and the centerline velocity, respectively.

Although the present two-dimensional controller augmented by an *ad hoc* three-dimensional controller has shown a promising result, it is apparent that we need to develop a three-dimensional controller using the same formulation presented in this paper. Extensions of LQG( $\mathcal{H}_2$ )/LTR design by using three-dimensional channel flow models are in progress.<sup>34,35</sup>

## ACKNOWLEDGMENTS

We thank Dr. S. Joshi and Professor R. T. McCloskey for the enlightening discussions during the course of this work. We also thank V. Ryder and Sungmoon Kang for their proofreading.

This work is supported by AFOSR Grant No. F49620-97-1-0276 and by NASA Grant No. NCC 2-374 Pr 41.

- <sup>1</sup>M. Gad-el-Hak, "Interactive control of turbulent boundary layers—A futuristic overview," *AIAA J.* **32**, 1753 (1994).
- <sup>2</sup>V. J. Modi, "Moving surface boundary-layer control: A review," *J. Fluids Struct.* **11**, 627 (1997).
- <sup>3</sup>H. L. Reed, W. S. Saric, and D. Arnal, "Linear stability theory applied to boundary layers," *Annu. Rev. Fluid Mech.* **28**, 389 (1996).
- <sup>4</sup>H. Choi, P. Moin, and J. Kim, "Active turbulence control for drag reduction in wall-bounded flows," *J. Fluid Mech.* **262**, 75 (1994).
- <sup>5</sup>R. Akhavan, W. J. Jung, and N. Mangiavacchi, "Turbulence control in wall-bounded flows by spanwise oscillations," *Appl. Sci. Res.* **51**, 299 (1993).
- <sup>6</sup>T. Berger, C. Lee, J. Kim, and J. Lim, "Turbulent boundary layer control utilizing the Lorentz force," *Phys. Fluids* **12**, 631 (2000).
- <sup>7</sup>H. Choi, R. Temam, P. Moin, and J. Kim, "Feedback control for unsteady flow and its application to the stochastic Burgers equation," *J. Fluid Mech.* **253**, 509 (1993).
- <sup>8</sup>T. Bewley and P. Moin, "Optimal control of turbulent channel flow," ASME Conference, ASME DE-Vol. 75, 1994.

- <sup>9</sup>C. Lee, J. Kim, D. Babcock, and R. Goodman, "Application of neural networks to turbulence control for drag reduction," *Phys. Fluids* **9**, 1740 (1997).
- <sup>10</sup>P. Koumoutsakos, "Vorticity flux control for a turbulent channel flow," *Phys. Fluids* **11**, 248 (1999).
- <sup>11</sup>S. Joshi, J. L. Speyer, and J. Kim, *Proceedings of the 34th Conference on Decision and Control*, New Orleans, Louisiana, December 1995.
- <sup>12</sup>S. Joshi, J. L. Speyer, and J. Kim, "A systems theory approach to the feedback stabilization of infinitesimal and finite-amplitude disturbances in plane Poiseuille flow," *J. Fluid Mech.* **332**, 157 (1997).
- <sup>13</sup>S. Joshi, J. L. Speyer, and J. Kim, "Finite dimensional optimal control of Poiseuille flow," *J. Guid. Control Dyn.* **22**, 340 (1999).
- <sup>14</sup>T. Bewley and S. Liu, "Optimal and robust control and estimation of linear paths to transition," *J. Fluid Mech.* **365**, 305 (1998).
- <sup>15</sup>L. Cortelezzi and J. L. Speyer, "Robust reduced-order controller of laminar boundary layer transitions," *Phys. Rev. E* **58**, 1906 (1998).
- <sup>16</sup>L. Cortelezzi, K. H. Lee, J. Kim, and J. L. Speyer, "Skin-friction drag reduction via robust reduced-order linear feedback control," *Int. J. Comput. Fluid Dyn.* **11**, 79 (1998).
- <sup>17</sup>L. Cortelezzi, K. H. Lee, J. L. Speyer, and J. Kim, "Robust reduced-order control of turbulent channel flows via distributed sensors and actuators," in *Proceedings of the 37th Conference on Decision and Control*, Tampa, Florida, December 1998.
- <sup>18</sup>K. Zhou, J. C. Doyle, and K. Glover, *Robust and Optimal Control* (Prentice-Hall, Englewood Cliffs, NJ, 1996).
- <sup>19</sup>I. Rhee and J. L. Speyer, "A game theoretic approach to a finite time disturbance attenuation problem," *IEEE Trans. Autom. Control* **36**, 1021 (1991).
- <sup>20</sup>A. E. Bryson and Y. C. Ho, *Applied Optimal Control* (Wiley, New York, 1969).
- <sup>21</sup>H. Kwakernaak and R. Sivan, *Linear Optimal Control Systems* (Wiley Interscience, New York, 1972).
- <sup>22</sup>J. C. Doyle and G. Stein, "Multivariable feedback design: Concepts for a classical/modern synthesis," *IEEE Trans. Autom. Control* **AC-26**, 4 (1981).
- <sup>23</sup>B. F. Farrell and P. J. Ioannou, "Stochastic forcing of the linearized Navier-Stokes equations," *Phys. Fluids A* **4**, 1637 (1992).
- <sup>24</sup>J. Kim and J. Lim, "A linear process in wall-bounded turbulent shear flows," *Phys. Fluids* **12**, 1740 (2000).
- <sup>25</sup>A referee pointed out that the wave number decoupling of this control problem was also recognized by others. See, for example, Bewley and Liu (Ref. 14) and Bewley and Agarwal in *CTR Proceedings of the 1996 Summer Program*, Stanford University, December 1996.
- <sup>26</sup>C. M. Ho and Y. C. Tai, "Microelectro-mechanical-systems (MEMS) and fluid flows," *J. Fluids Eng.* **118**, 437 (1996).
- <sup>27</sup>B. Bamieh, F. Paganini, and M. A. Dahleh, "Distributed control of spatially invariant systems," to appear in *IEEE Trans. Automatic Control*.
- <sup>28</sup>J. Kim, P. Moin, and R. Moser, "Turbulence statistics in fully-developed channel flow at low Reynolds number," *J. Fluid Mech.* **177**, 133 (1987).
- <sup>29</sup>J. M. Hamilton, J. Kim, and F. Waleffe, "Regeneration mechanisms of near-wall turbulence structures," *J. Fluid Mech.* **287**, 317 (1995).
- <sup>30</sup>W. Schoppa and F. Hussain, "A large-scale control strategy for drag reduction in turbulent boundary layers," *Phys. Fluids* **10**, 1049 (1998).
- <sup>31</sup>C. Lee, J. Kim, and H. Choi, "Suboptimal control of turbulent channel flow for drag reduction," *J. Fluid Mech.* **401**, 245 (1998).
- <sup>32</sup>P. Moin and T. Bewley, "Application of control theory to turbulence," *12th Australian Fluid Mechanics Conference*, Sydney, Australia, 10–15 December 1995.
- <sup>33</sup>K. H. Lee, "A system theory approach to control of transitional and turbulent flows," Ph.D. dissertation, Department of Mechanical Engineering, University of California, Los Angeles, CA, September 1999.
- <sup>34</sup>S. M. Kang, V. Ryder, L. Cortelezzi, and J. L. Speyer, "State-space formulation and control design for three-dimensional channel flows," *1999 American Control Conference*, San Diego, California, 2–4 June 1999.
- <sup>35</sup>S. M. Kang, L. Cortelezzi, and J. L. Speyer, "Performance of a linear controller for laminar boundary layer transition in three dimensional channel flow," in *Proceedings of the 38th Conference on Decision and Control*, Phoenix, Arizona, 7–10 Dec. 1999.

APPENDIX C:  
Robust Feedback Control of  
Rayleigh-Bénard Convection

## Robust feedback control of Rayleigh–Bénard convection

By A. C. OR<sup>1</sup>, L. CORTELEZZI<sup>2</sup> AND J. L. SPEYER<sup>1</sup>

<sup>1</sup>Department of Mechanical & Aerospace Engineering, University of California,  
Los Angeles, CA 90095-1597, USA

<sup>2</sup>Department of Mechanical Engineering, McGill University, Montreal, Canada H3A 2K6

(Received 28 July 2000 and in revised form 7 December 2000)

We investigate the application of linear-quadratic-Gaussian (LQG) feedback control, or, in modern terms,  $\mathcal{H}_2$  control, to the stabilization of the no-motion state against the onset of Rayleigh–Bénard convection in an infinite layer of Boussinesq fluid. We use two sensing and actuating methods: the planar sensor model (Tang & Bau 1993, 1994), and the shadowgraph model (Howle 1997a). By extending the planar sensor model to the multi-sensor case, it is shown that a LQG controller is capable of stabilizing the no-motion state up to 14.5 times the critical Rayleigh number. We characterize the robustness of the controller with respect to parameter uncertainties, unmodelled dynamics. Results indicate that the LQG controller provides robust performances even at high Rayleigh numbers.

### 1. Introduction

When a layer of fluid at rest is heated from below, fluid motion will develop into well-organized convection patterns if the temperature difference across the layer is sufficiently large (Cross & Hohenberg 1993). For certain industrial applications, developing a temperature gradient across the fluid layer is unavoidable but at the same time preventing convective fluid motions is desirable. Some examples involving undesirable effects of convection are materials processing, solidification, semiconductor melts, welding, evaporative coating and crystal growth. Our aim is to use robust modern control methodologies to inhibit the onset of convection while permitting a large thermal gradient across the layer of fluid.

The idea of stabilizing the fluid layer against the onset of cellular motions has been advanced by Tang & Bau (1993, 1994, 1998a,b) and Howle (1997a–c, 2000). Tang & Bau assumed that the temperature field can be measured continuously on a horizontal plane in  $x, y$  and  $t$  (see figure 1). The measurements are then used to control the temperature at the lower wall, in order to cancel the thermal disturbances in the fluid that drive the overturning motions. Howle (1997a) investigated a similar control problem, except in his case the measurements consist of shadowgraph images of the fluid. The shadowgraph images capture the horizontal distribution of the vertical-mean temperature. Moreover, in Howle's model, heat flux rather than temperature is prescribed at the lower wall. Both types of sensor and actuator models will be considered in this study using a more sophisticated form of control synthesis.

Based on proportional feedback control, the results of Tang & Bau and Howle show that both sensor models exhibit a maximal achievable stable value of Rayleigh number  $Ra$ , beyond which this simple controller is ineffective for stabilization. For the

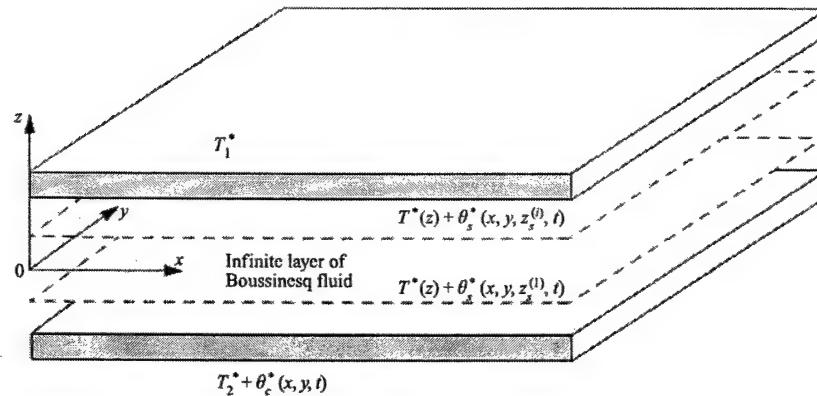


FIGURE 1. Planar sensor model.

planar-sensor model Tang & Bau (1993, 1994) showed that the controller can inhibit convection up to a maximum of about 3.8 times  $Ra_{c0}$  at  $Pr = 7$ , where  $Ra_{c0} = 1707.76$  is the uncontrolled critical value. This value is  $Pr$ -dependent. Furthermore, they (Tang & Bau 1994) considered a velocity actuator which inhibits convection up to 10 times the critical Rayleigh number. For the shadowgraph sensor model this maximum is about 3.13 times  $Ra_{c0} = 1295.78$ . In §4 the differences in performance between the two sensor models using only the thermal actuators, and the limitations of the proportional feedback control will be discussed.

The degree of stabilization can be improved significantly by using synthesis methods for multiple-input/multiple-output systems which produce dynamic compensators. However, in this study a distributed single-input/multiple-output strategy will be considered, since normal modes of different wavenumbers decouple and each normal mode can be controlled individually.

One such synthesis method is known as the linear-quadratic-Gaussian (LQG) control (Bryson & Ho 1969), or, in modern terms,  $\mathcal{H}_2$  control. Other methods such as  $\mathcal{H}_\infty$  synthesis (Rhee & Speyer 1991) could also be applied, but we suspect with similar results. The LQG approach allows us to consider a nominal design Rayleigh number ( $Ra^*$ ) significantly higher than that considered in the previous studies. For values of  $Ra$  sufficiently near  $Ra^*$ , stabilization with the LQG controller appears always to be achievable. Moreover, for  $Ra^*$  below a certain threshold, the complete range of  $Ra$  up to a critical value can be stabilized. In this study, we show that the system can be stabilized up to  $Ra = 14.8Ra_{c0}$ . In this range the first even and odd modes of convection can become unstable. However, these two modes are damped by the LQG controller. The higher modes are naturally damped within this range of  $Ra$ . Our aim is to ensure stability over the entire range of  $Ra$  up to a maximum critical Rayleigh number, without the formation of isolated unstable regions within this range. This requires the determination of the value of  $Ra^*$  to produce this maximum critical Rayleigh number.

Unlike the proportional control method, the LQG synthesis method requires some elaboration. This synthesis method consists of two steps: (i) a reconstruction of the internal states of the plant based on the measured information, and (ii) a regulation of the plant states in order to drive the estimated perturbations to a zero level. To



accomplish these two steps, the LQG controller is formed by a Kalman filter and an optimal regulator in cascade.

The LQG synthesis method has recently been used in the study of drag reduction in channel flow by Joshi, Speyer & Kim (1999) and by Cortelezzi & Speyer (1998) based on Joshi, Speyer & Kim (1997) who first introduced the system theory approach. Cortelezzi & Speyer (1998) presented a framework suited to practical implementations and demonstrated the performance of the design in numerical simulations. Following this framework, our investigations focus on a robust stability analysis of the closed-loop system as applied to Rayleigh-Bénard convection. Design parameters of the filter and regulator are carefully chosen to enhance the robustness of the stabilization. Several integrated design aspects are discussed.

This study is intended to provide a design of controllers for future experiments. The design goal is to maximize the stability range of Rayleigh number. This implies designing controllers at the highest possible design value  $Ra^*$ , without causing an unstable, isolated region to form below  $Ra^*$ . Since the controllers are implemented at each wavenumber and only  $Ra$  is being varied, one form of robustness being demonstrated is the robustness of the system with respect to variations in  $Ra$  away from  $Ra^*$ . Another form of robustness is concerned with uncertainties in the system apart from the mismatch in  $Ra$ , for example uncertainties due to nonlinearities or unmodelled dynamics. The objective of this paper is to produce a robust design based on classical relative stability measures of gain and phase margins that accommodates to a degree unmodelled dynamics and nonlinearities. Nonlinear simulation is required to validate the design. We will show that the gain and phase margins depends crucially on the number of sensors used. More measurements implies better knowledge about the internal states of the system. In this study we are interested in determining the minimum number of sensor planes, as well as their locations, for achieving a reasonable degree of robustness. From a theoretical point of view, the planar sensor model appears to be more effective and accurate than the shadowgraph sensor model, mainly because a multiple planar sensor configuration can be readily incorporated. As the results will show, increasing the number of sensors, i.e. the measured information about the internal states, is crucial for achieving the desirable robustness.

We now proceed to §2 to derive the standard state-space equations for both sensor models. In §3, we review the theory of the LQG optimal control synthesis. In §4, the results are discussed and in §5, we conclude the paper.

## 2. State-space formulation

In this Section, we derive the state-space equations. Following the framework presented by Cortelezzi & Speyer (1998), we start from the governing equations and subsequently transform them into a set of ordinary differential equations expressed in state-space form. This procedure includes a transformation of variables, a spectral decomposition of the resulting equations and expressing these equations in the standard state-space form.

### 2.1. Governing equations

We consider an infinite layer of Boussinesq fluid heated from below, which is parallel to the  $(x, y)$ -plane and bounded by non-permeable walls at  $z = \pm d/2$  (see figure 1). Our aim is to compare the performance of the LQG controller with the performance of the proportional feedback control method based on two known models. Therefore, in our formulation the boundary conditions used in these two models will be preserved.



For both models, the upper wall is assumed to be infinitely conductive at constant temperature  $T_1^*$ . For the planar sensor model (Tang & Bau 1993, 1994, 1998a,b) temperature is measured on an interior plane (see figure 1,  $T^*(z)$  denotes the basic state). These measurements are used to modify the constant lower wall temperature  $T_2^*$  with the actuator temperature  $\theta_c^*(x, y, t)$ . For the shadowgraph sensor model (Howle 1997a,b) measurements of the vertical-mean temperature distribution are obtained in the form of a shadowgraph. These measurements are used to modify the constant heat flux  $Q^*$  at the lower wall with the actuator heat flux  $q_c^*(x, y, t)$ . Different actuators are used to allow direct comparisons between the performances of the LQG controllers and the proportional controllers used in the original models.

We scale length, time, velocity, pressure relative to the hydrostatic pressure, and temperature, respectively, by  $d$ ,  $d^2/\kappa$ ,  $\kappa/d$ ,  $\rho v \kappa/d^2$  and  $(T_2^* - T_1^*)$  or  $Q^* d/K$  depending on the model chosen, where  $\rho$ ,  $\kappa$ ,  $v$  and  $K$  are, respectively, density, thermal diffusivity, kinematic viscosity and thermal conductivity of the fluid. The linear stability equations for the vertical perturbation velocity  $w(x, y, z, t)$  and perturbation temperature  $\theta(x, y, z, t)$  are

$$(Pr^{-1} \partial_t - \nabla^2) \nabla^2 w = Ra \nabla_\perp^2 \theta, \quad (2.1)$$

$$(\partial_t - \nabla^2) \theta = w, \quad (2.2)$$

where  $\nabla_\perp^2 = \nabla^2 - \partial_{zz}$  (e.g. Chandrasekhar 1961). The Prandtl number is  $Pr = \nu/\kappa$ . The Rayleigh number for the planar and shadowgraph cases are defined, respectively, as  $Ra = \alpha g (T_2^* - T_1^*) d^3 / \nu \kappa$  and  $Ra = \alpha g Q^* d^4 / K \nu \kappa$ , where  $\alpha$  is the coefficient of volume expansion and  $g$  is the gravitational acceleration.

The boundary conditions on velocity are

$$w(x, y, \pm 1/2, t) = \partial_z w(x, y, \pm 1/2, t) = 0. \quad (2.3)$$

For the thermal boundary conditions, the upper wall is considered isothermal so that the perturbation temperature must satisfy

$$\theta(x, y, 1/2, t) = 0. \quad (2.4)$$

Based on the planar and shadowgraph sensor models (Tang & Bau 1993, 1994; Howle 1997a), we apply a continuous time-dependent control temperature along the lower wall for the planar sensor case,

$$\theta(x, y, -1/2, t) = \theta_c(x, y, t), \quad (2.5)$$

while for the shadowgraph model we apply a continuous time-dependent heat flux  $q_c$  instead,

$$\partial_z \theta(x, y, -1/2, t) = q_c(x, y, t). \quad (2.6)$$

The planar sensor model measures the temperature distribution at a number  $I$  of  $(x, y)$ -planes located at  $z = z_s^{(i)} \in [-1/2, 1/2]$ , where  $i = 1, 2, \dots, I$ . The measurement equations are

$$\theta_s^{(i)}(x, y, t) = \theta(x, y, z_s^{(i)}, t), \quad i = 1, 2, \dots, I, \quad (2.7)$$

where  $z_s^{(i)}$  is the  $z$ -coordinate of the  $i$ th sensor plane. The shadowgraph model measures the average density over the whole layer,  $\rho_s$ , which is expressed in terms of temperature by

$$\rho_s(x, y, t) = \int_{-1/2}^{1/2} \nabla_\perp^2 \theta(x, y, z, t) dz, \quad (2.8)$$

where  $\rho_s$  is the measurement function in density. We refer readers to Howle (1997a) for the derivations of this integral expression.

## 2.2. Transformation of dependent variables and cost criterion

We transform the perturbation temperature so that equations (2.1)–(2.8) have homogeneous thermal boundary conditions. The perturbation velocity remains unchanged. With the perturbation temperature as  $\theta \equiv \phi + \xi$ , we obtain for both sensor models

$$(Pr^{-1}\partial_t - \nabla^2)\nabla^2 w - Ra\nabla_{\perp}^2 \phi = Ra\nabla_{\perp}^2 \xi, \quad (2.9)$$

$$(\partial_t - \nabla^2)\phi - w = -(\partial_t - \nabla^2)\xi, \quad (2.10)$$

subject to the boundary conditions

$$w(x, y, \pm 1/2, t) = \partial_z w(x, y, \pm 1/2, t) = \phi(x, y, 1/2, t) = 0. \quad (2.11)$$

Furthermore, for the planar sensor model  $\phi$  must satisfy the boundary condition

$$\phi(x, y, -1/2, t) = 0, \quad (2.12)$$

while for the shadowgraph sensor model  $\phi$  must satisfy the boundary condition

$$\partial_z \phi(x, y, -1/2, t) = 0. \quad (2.13)$$

The forcing function  $\xi$  satisfies a non-homogeneous boundary condition at the lower wall and a homogeneous boundary condition at the upper wall. For the planar case these conditions are

$$\xi(x, y, -1/2, t) = \theta_c(x, y, t), \quad \xi(x, y, 1/2, t) = 0, \quad (2.14)$$

and for the shadowgraph case we have instead

$$\partial_z \xi(x, y, -1/2, t) = q_c(x, y, t), \quad \xi(x, y, 1/2, t) = 0. \quad (2.15)$$

The two set of measurement equations in terms of the new variables for the planar and shadowgraph cases become

$$\theta_s^{(i)}(x, y, t) = \phi(x, y, z_s^{(i)}, t) + \xi(x, y, z_s^{(i)}, t), \quad i = 1, 2, \dots, I, \quad (2.16)$$

and

$$\rho_s(x, y, t) = \int_{-1/2}^{1/2} \nabla_{\perp}^2 (\phi(x, y, z, t) + \xi(x, y, z, t)) dz. \quad (2.17)$$

Note that the sensors could be located at discrete points in the  $(x, y)$ -plane, but to be consistent with Tang & Bau (1993, 1994) we have considered continuously distributed sensors. Furthermore, Tang & Bau's (1998a) experiment using discrete sensors and actuators shows consistency with their theoretical work using continuously distributed sensors and actuators.

Finally, we introduce the cost criterion. Our goal is to design a controller able to drive the measured perturbation temperature to zero, without using unnecessarily large control action, hopefully resulting in little saturation of the actuators. Thus, the performance index includes weighting on the control. We consider a layer of fluid with large aspect ratios  $L_x$  and  $L_y$  with periodic boundary conditions (see figure 1), assuming that the influence of the lateral boundary conditions in a finite layer of fluid is negligible. The LQG controller is determined by finding the control action which minimizes the cost criterion. For the planar sensor model we define the cost criterion

as

$$\mathcal{J} = \int_t^T \left\{ \int_0^{L_x} \int_0^{L_y} \left[ \sum_{i=1}^I (\theta_s^{(i)})^2 + \gamma \theta_c^2 \right] dx dy \right\} d\tau, \quad (2.18)$$

and for the shadowgraph sensor model it is

$$\mathcal{J} = \int_t^T \left\{ \int_0^{L_x} \int_0^{L_y} \int_t^T (\rho_s^2 + \gamma q_c^2) dx dy \right\} d\tau. \quad (2.19)$$

### 2.3. Modal decomposition

A periodic boundary condition permits us to perform a Fourier decomposition in the horizontal coordinates. The vertical dependence of the flow field and thermal field is constrained by the upper and lower wall boundary conditions. The vertical dependence will be decomposed separately in §2.4. We describe an infinitesimal three-dimensional disturbance to the no-motion state. Consequently, we have a double sum of the Fourier normal modes for the disturbances:

$$\left. \begin{aligned} w(x, y, z, t) &= \sum_{m=1}^M \sum_{n=1}^N \left\{ \frac{1}{2} [W_{r,mn}(z, t) + iW_{i,mn}(z, t)] e^{i(mk_x x + nk_y y)} + \text{c.c.} \right\}, \\ \phi(x, y, z, t) &= \sum_{m=1}^M \sum_{n=1}^N \left\{ \frac{1}{2} [\Phi_{r,mn}(z, t) + i\Phi_{i,mn}(z, t)] e^{i(mk_x x + nk_y y)} + \text{c.c.} \right\}, \\ \xi(x, y, z, t) &= \sum_{m=1}^M \sum_{n=1}^N \left\{ \frac{1}{2} [\Xi_{r,mn}(z, t) + i\Xi_{i,mn}(z, t)] e^{i(mk_x x + nk_y y)} + \text{c.c.} \right\}, \end{aligned} \right\} \quad (2.20)$$

where c.c. denotes the complex conjugate. The measurement and control functions are represented by

$$\left. \begin{aligned} \theta_s^{(j)}(x, y, t) &= \sum_{m=1}^M \sum_{n=1}^N \left\{ \frac{1}{2} [\Theta_{sr,mn}^{(j)}(t) + i\Theta_{si,mn}^{(j)}(t)] e^{i(mk_x x + nk_y y)} + \text{c.c.} \right\}, \quad j = 1, \dots, I, \\ \rho_s(x, y, t) &= \sum_{m=1}^M \sum_{n=1}^N \left\{ \frac{1}{2} [R_{sr,mn}(t) + iR_{si,mn}(t)] e^{i(mk_x x + nk_y y)} + \text{c.c.} \right\}, \\ \theta_c(x, y, t) &= \sum_{m=1}^M \sum_{n=1}^N \left\{ \frac{1}{2} [\Theta_{cr,mn}(t) + i\Theta_{ci,mn}(t)] e^{i(mk_x x + nk_y y)} + \text{c.c.} \right\}, \\ q_c(x, y, t) &= \sum_{m=1}^M \sum_{n=1}^N \left\{ \frac{1}{2} [Q_{cr,mn}(t) + iQ_{ci,mn}(t)] e^{i(mk_x x + nk_y y)} + \text{c.c.} \right\}, \end{aligned} \right\} \quad (2.21)$$

where the subscripts  $r$  and  $i$  indicate real and imaginary parts, respectively. The two fundamental wavenumbers are  $k_x = 2\pi/L_x$  and  $k_y = 2\pi/L_y$ . From the classical theory without control, a normal mode disturbance is unstable in the region above a neutral curve  $Ra_0(k)$  (Chandrasekhar 1961), where  $Ra_0$  is the Rayleigh number at neutral stability in the open-loop system and  $k = \sqrt{k_x^2 + k_y^2}$  is the magnitude of the wavevector. We truncate the infinite series above to  $M \times N$  horizontal modes, which span the unstable range. Since the basic equations depend only on the horizontal Laplacian  $\nabla_{\perp}^2$ , the wavenumbers appear only in even powers and can be described

in terms of an internal parameter  $k(m, n)$ , where  $k(m, n) = \sqrt{m^2 k_x^2 + n^2 k_y^2}$ . We further substitute (2.20) and (2.21) into equations (2.9)–(2.17) and separate the real and imaginary parts. It should be remarked that the linear structure includes all patterns at the onset. Certain realizable patterns, such as rolls and hexagons, will be selected when the nonlinear and symmetry-breaking effects are included in the model. The paper is focused on the stabilization of the no-motion state. Suppression of selected convection patterns and return to the no-motion state will be addressed by applying our LQG controller to a direct numerical simulation of convection.

Since the governing equations contain only even derivatives with respect to  $x$  or  $y$ , the real and imaginary parts of the dependent variables decouple and satisfy the same set of equations. Furthermore, since the problem is linear, we can consider each normal mode separately. For simplicity of notation, we drop the indices of the Fourier coefficients, and define  $W \equiv W_{r,mn} = W_{i,mn}$ ,  $\Phi \equiv \Phi_{r,mn} = \Phi_{i,mn}$ ,  $\Xi \equiv \Xi_{r,mn} = \Xi_{i,mn}$ ,  $\Theta_c \equiv \Theta_{cr,mn} = \Theta_{ci,mn}$ ,  $Q_c \equiv Q_{cr,mn} = Q_{ci,mn}$ ,  $\Theta_s^{(i)} \equiv \Theta_{sr,mn}^{(i)} = \Theta_{si,mn}^{(i)}$  and  $R_s \equiv R_{sr,mn} = R_{si,mn}$ . The governing equations are reduced as follows:

$$[Pr^{-1}(\partial_z^2 - k^2)\partial_t - (\partial_z^2 - k^2)]W + Rak^2\Phi = -Rak^2\Xi, \quad (2.22)$$

$$[\partial_t - (\partial_z^2 - k^2)]\Phi - W = -[\partial_t - (\partial_z^2 - k^2)]\Xi. \quad (2.23)$$

The boundary conditions are homogeneous. For the planar case we have

$$W(\pm 1/2, t) = \partial_z W(\pm 1/2, t) = \Phi(\pm 1/2, t) = 0, \quad (2.24)$$

and for the shadowgraph sensor model we have instead

$$W(\pm 1/2, t) = \partial_z W(\pm 1/2, t) = \Phi(1/2, t) = 0, \quad \partial_z \Phi(-1/2, t) = 0. \quad (2.25)$$

The forcing function  $\Xi$  satisfies the non-homogeneous boundary condition at the lower wall and the homogeneous boundary condition at the upper wall. For the planar case the forcing function is given by

$$\Xi(-1/2, t) = \Theta_c(t), \quad \Xi(1/2, t) = 0, \quad (2.26)$$

and the corresponding measurement functions are

$$\Theta_s^{(i)}(t) = \Phi(z_s^{(i)}, t) + \Xi(z_s^{(i)}, t), \quad i = 1, 2, \dots, I. \quad (2.27)$$

For the shadowgraph sensor model, the forcing function  $\Xi$  is

$$\partial_z \Xi(-1/2, t) = Q_c(t), \quad \Xi(1/2, t) = 0, \quad (2.28)$$

and the corresponding measurement function is

$$R_s(t) = -k^2 \int_{-1/2}^{1/2} (\Phi(z, t) + \Xi(z, t)) dz. \quad (2.29)$$

In our approach, each distinct horizontal normal mode is controlled by a separate controller. Therefore, for the implementation  $M \times N$  controllers are required. As a simple illustration for the analysis, consider an aspect ratio  $L_x/d$  and  $L_y/d$  equal to  $20\pi$ . In this case, the only wavenumbers present are the fundamental wavenumber  $k_f = 2\pi/L = 0.05$ , and its harmonics: for  $Ra$  up to  $15Ra_{c0}$ , the wavenumbers are from  $k = k_f$  to  $k = 12$  (equal to  $240k_f$ ). These wavenumbers represent the ensemble of normal modes used to represent the convection field.

In a physical implementation of the planar sensor model, both the measurements and control action occur in physical space but the controllers operate in the Fourier

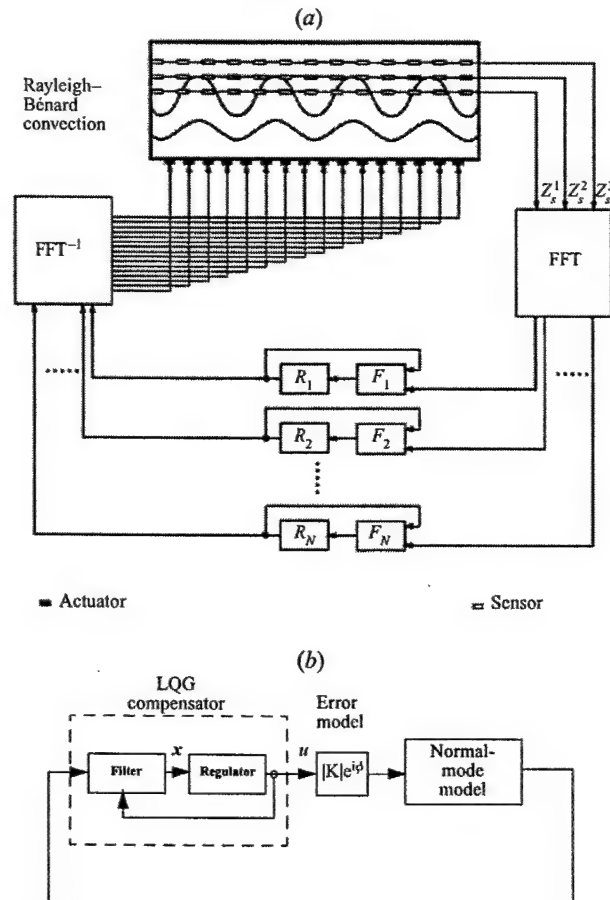


FIGURE 2. (a) Schematic for the physical implementation of the multi-wavenumber controller:  $R_n$ , regulator;  $F_n$ , filter; and FFT, fast Fourier transform. (b) Block diagram of the control loop for a single wavenumber.

space. Sensors and actuators are interfaced to the controllers by fast Fourier transforms (FFT). Figure 2(a) links with simplicity the mathematical formulation to its computational implementation by summarizing in a block diagram the control strategy described above. The controllers can be programmed in a computer routine whose inputs are the arrays containing the temperatures measured by the planar sensors and whose output is an array containing the temperatures to be applied at the bottom the wall. The temperature measurements obtained by the planar sensors are converted by a fast Fourier transform into a set of modal sensor variables. Each pair of estimator and control blocks is integrated in time. Parallel computation produces the modal control variables. An inverse FFT converts the modal control variables into the actuating temperature at the bottom wall. This routine can be embedded in any Navier-Stokes solver able to handle time-dependent boundary conditions for the control of more realistic simulations of Rayleigh-Bénard convection.

Figure 2(a) also provides the basic architecture for the potential implementation

of the present controller in an experiment and, eventually, in practical engineering applications. The temperature distribution at a given plane ( $z_s^{(i)}$ ) ( $i = 1, 2, \dots, I$ ) could be measured by a planar sensor constructed with an array of micro-electro-mechanical-system (MEMS) diode sensors (see Tang & Bau 1998a,b). Analog to digital converters (A/D) and digital signal processors (DSP) would convert the measured temperatures  $z_s^{(i)}$  into the modal sensor variables. Each pair of estimator and control blocks would be replaced by a microprocessor, and a parallel computation produces the modal control variables. A DSP and a digital to analog converter (D/A) would produce the actuating signal. Finally, an array of MEMS heaters would provide the temperature distribution at the bottom wall (Tang & Bau 1998a,b).

#### 2.4. State-space representation of temporal dynamics

In this subsection, we consider a numerical procedure to represent the vertical dependence of the velocity and thermal field. We use the Galerkin approach (Gottlieb & Orszag 1981) for the representation of the vertical dependence of the normal modes. The beam functions  $\{\varphi_m\}$  are used as the basis functions for  $W$  which has to satisfy four boundary conditions. On the other hand the sinusoidal functions  $\{\beta_m\}$  are used as basis functions for  $\Phi$  which only has to satisfy two boundary conditions. In our numerical computations, we truncate the infinite set to the first  $N_z$  terms for both  $W$  and  $\Phi$ . We use the same truncation number for both fields mainly for numerical convenience.

In general the Chebyshev polynomials have good convergence properties. However, in our application an individual polynomial does not satisfy the homogeneous boundary conditions. In contrast, individual beam functions do satisfy the homogeneous boundary conditions naturally and they converge reasonably fast for our stability analysis. Also, since we have transformed the thermal boundary condition at the lower wall to a homogeneous form, our results are not affected by Gibb's phenomenon in the vertical dependence. In practical applications when realistic lateral boundary conditions are incorporated, Gibb's phenomenon can affect the horizontal dependence (at small wavenumbers) and therefore the performance of the controller. However, the detrimental effects of Gibb's phenomenon can be substantially reduced using appropriate windowing techniques.

The Fourier coefficients for the vertical velocity  $W(z, t)$  are expanded as follows:

$$W(z, t) = \sum_{m=1}^{N_z} A_m(t) \varphi_m(z) = \sum_{m=1}^{N_z} A_m(t) \left[ \frac{\sinh(a_m z + im\pi/2)}{\sinh(a_m + im\pi/2)} - \frac{\sin(a_m z + m\pi/2)}{\sin(a_m + m\pi/2)} \right]. \quad (2.30)$$

Since the thermal boundary conditions for the planar sensor model and shadowgraph sensor model are different, the sinusoidal basis functions  $\{\beta_m\}$  are different for the two cases. For the planar sensor model we let

$$\Phi(z, t) = \sum_{m=1}^{N_z} B_m(t) \beta_m(z) = \sum_{m=1}^{N_z} B_m(t) \sqrt{2} \sin[m\pi(z + 1/2)], \quad (2.31)$$

and for the shadowgraph sensor model we have instead

$$\Phi(z, t) = \sum_{m=1}^{N_z} B_m(t) \beta_m(z) = \sum_{m=1}^{N_z} B_m(t) \sqrt{2} \sin[(m - 1/2)\pi(z - 1/2)]. \quad (2.32)$$



A convenient choice for  $\Xi$  which satisfies the appropriate boundary conditions of the planar sensor case is

$$\Xi(z, t) = (1/2 - z)\Theta_c(t), \quad (2.33)$$

and one which satisfies the boundary conditions of the shadowgraph sensor case is

$$\Xi(z, t) = (z - 1/2)Q_c(t). \quad (2.34)$$

For the planar case, we now substitute (2.30), (2.31) and (2.33) into (2.22) and (2.23), and perform the Galerkin projection. The following equations are obtained:

$$\begin{aligned} Pr^{-1} \sum_{m=1}^{N_z} \langle \varphi_j, (\partial_z^2 - k^2) \varphi_m \rangle \dot{A}_m &= \sum_{m=1}^{N_z} \langle \varphi_j, (\partial_z^2 - k^2) \varphi_m \rangle A_m \\ &\quad - k^2 Ra \sum_{m=1}^{N_z} \langle \varphi_j, \beta_m \rangle B_m - k^2 Ra \langle \varphi_j, (1/2 - z) \rangle \Theta_c, \end{aligned} \quad (2.35)$$

$$\begin{aligned} \dot{B}_m &= \sum_{j=1}^{N_z} \langle \beta_j, (\partial_z^2 - k^2) \beta_m \rangle B_j + \sum_{j=1}^{N_z} \langle \beta_j, \varphi_m \rangle A_j \\ &\quad - \langle \beta_j, (1/2 - z) \rangle \dot{\Theta}_c + \langle \beta_j, (\partial_z^2 - k^2)(1/2 - z) \rangle \Theta_c, \end{aligned} \quad (2.36)$$

where the index  $j$  runs from 1 to  $N_z$  and the inner product  $\langle \cdot, \cdot \rangle$  denotes integration over  $z \in [-1/2, 1/2]$ . The corresponding equations for the shadowgraph model can be obtained from (2.35), (2.36) by replacing  $\Theta_c$  by  $Q_c$  and  $(1/2 - z)$  by  $(z - 1/2)$ . Therefore the shadowgraph model equations will not be presented explicitly.

After substituting (2.31) and (2.33) into (2.27), we obtain  $I$  measurement equations for the planar case,

$$\Theta_s^{(i)}(t) = \sum_{m=1}^{N_z} B_m(t) \beta_m(z_s^{(i)}) + (1/2 - z_s^{(i)}) \Theta_c, \quad i = 1, 2, \dots, I. \quad (2.37)$$

For the shadowgraph case, upon substitution of (2.32) and (2.34) into (2.29), we have a single measurement equation

$$R_s(t) = \sum_{m=1}^{N_z} B_m(t) \int_{-1/2}^{1/2} (-k^2) \beta_m(z) dz + Q_c \int_{-1/2}^{1/2} (-k^2)(z - 1/2) dz. \quad (2.38)$$

As a final step, we construct a state vector  $X$  by arranging the coefficients  $A_m$  and  $B_m$  as follows:

$$X \equiv [A_1, A_2, \dots, A_{N_z}, B_1, B_2, \dots, B_{N_z}]', \quad (2.39)$$

where superscript  $'$  denotes the transpose. Equations (2.35) and (2.36) can be rewritten in state-space form as

$$\dot{X} = AX + B_1 \Theta_c + B_2 \dot{\Theta}_c, \quad (2.40)$$

while the measurement equation (2.37) can be re-written as

$$\Theta_s = CX + D_3 \Theta_c. \quad (2.41)$$

In order to cast the matrix equation in a standard state-space form we can choose either  $\Theta_c$  or its time derivative as the control action variable. Here we define  $u = \Theta_c$ . The term  $\dot{\Theta}_c$  can be eliminated from (2.40) by defining a new state vector  $x = X - B_2 \Theta_c$ .

Upon transformation, the state-space equations can be written as

$$\dot{x} = Ax + Bu, \quad (2.42)$$

$$z = Cx + Du, \quad (2.43)$$

where  $B = B_1 + AB_2$ ,  $D = D_3 + CB_2$ ,  $u = \Theta_c$  and  $z = \Theta_s$ . Matrices  $A$ ,  $B$ , and  $C$  contain the dynamics of the plant, actuators, and sensors, respectively. Matrix  $D$  contains the direct coupling between sensors and actuators.

The cost function of each wavenumber can be minimized individually, because of the orthogonality between pairs of Fourier modes. From (2.18), (2.19), following the normal decomposition, the cost function in state-space form for wavenumber  $k$  is

$$\mathcal{J}(k) = \int_t^T (z'z + \gamma u'u) d\tau. \quad (2.44)$$

In §4, we allow  $z$  to be a vector but restrict  $u$  to a scalar quantity  $u$ .

### 3. Optimal control theory

In this section we describe the basic theory of the LQG control (Bryson & Ho 1969), or, in modern terms,  $\mathcal{H}_2$  control. A brief review will be given in a self-contained manner to provide the necessary governing equations for the closed-loop stability analysis.

The LQG problem is formulated as a stochastic optimal control problem described by equations

$$\dot{x} = Ax + Bu + \Gamma w, \quad (3.1)$$

$$z = Cx + Du + v, \quad (3.2)$$

where  $\Gamma$  is an input matrix,  $w$  and  $v$  are both white noise processes with zero means and auto-correlation functions

$$E[w(t)w'(\tau)] = W\delta(t-\tau), \quad E[v(t)v'(\tau)] = V\delta(t-\tau), \quad (3.3)$$

where  $E[\cdot]$  is the expectation operator averaging over all underlying random variables and  $\delta(t-\tau)$  is the delta function. Note that  $W$  and  $V$ , the power spectral densities, will be chosen here as design parameters to enhance system performance. In our case  $\Gamma$  will be taken as  $B$ , implying that the disturbances, in a manner similar to the control, enter the system dynamics at the wall.

The LQG controller is determined by finding the control action  $u(Z_t)$ , where  $Z_t = \{z(\tau); 0 \leq \tau \leq t\}$  is the measurement history, which minimizes the cost criterion

$$J = \lim_{T \rightarrow \infty} \frac{1}{T-t} E \left[ \int_t^T (x'Qx + 2x'Nu + u'Ru) d\tau \right] \quad (3.4)$$

subject to the stochastic dynamic system model equations (3.1) and (3.2). The division by  $(T-t)$  ensures that the cost criterion remains finite in the presence of uncertainties in the infinite-time problem ( $T \rightarrow \infty$ ). Note that (3.4) can include (2.44) where

$$J = \lim_{T \rightarrow \infty} \frac{1}{T-t} E[\mathcal{J}(k)]. \quad (3.5)$$

Note also that even though the time interval is infinite, time response is still measured by the eigenvalues of the closed-loop system. We consider the infinite-time problem with a time-invariant dynamics system because the controller gains become constants.

For  $Q$  and  $N$  chosen to be consistent with the cost criterion (2.44) (see (3.18)), the cost criterion will remain positive definite (see Bryson & Ho (1969) for necessary and sufficient conditions for optimality with general  $Q$  and  $N$ ).

By nesting the conditional expectation with respect to  $Z_t$  within the unconditional expectation of (3.4), i.e.  $E[\mathcal{J}(k)] = E[E[\mathcal{J}(k)/Z_t]]$  where  $E[\cdot/Z_t]$  denotes the expectation ( $\cdot$ ) conditioned on  $Z_t$ , the cost criterion can be written as

$$J = \lim_{T \rightarrow \infty} \frac{1}{T-t} E \left[ \int_t^T [\hat{x}' Q \hat{x} + 2\hat{x}' N u + u' R u + \text{tr}(P)] d\tau \right], \quad (3.6)$$

where  $\hat{x} = E[x/Z_t]$  is the conditional mean estimate of the state  $x$ . The term  $\text{tr}(P)$  is the trace of the error variance matrix which naturally occurs as a result of taking the conditional expectation into the integrand of the cost criterion. This cost criterion is now minimized subject to the estimation equations discussed below. Note that  $P$  does not depend on the control (see (3.9) below) and therefore does not enter into the optimization process.

The solution to the regulator problem (Bryson & Ho 1969) is a compensator composed of a state reconstruction process, known here as a filter (in the no-noise case it is known as an observer) in cascade with a controller (see figure 2b). The state estimate (conditional mean) is called the Kalman filter, and is governed by

$$\dot{\hat{x}} = A^* \hat{x} + B^* u + K_f v, \quad v = z - \hat{z} = C^*(x - \hat{x}) + v, \quad (3.7)$$

where the matrices with asterisk superscripts correspond to the nominal point ( $k^*, Ra^*$ ). The Kalman gain matrix  $K_f$ , constructed to trade the accuracy of the new measurements against the accuracy of the state propagated from the system dynamics, is given by

$$K_f = P C^{*'} V^{-1}, \quad (3.8)$$

where  $P$  is the error variance in the statistical problem. In the infinite-time stationary formulation, the error variance  $P$  is the solution to the algebraic Riccati equation (ARE),

$$A^* P + P A^{*'} + \Gamma W \Gamma' - P C^{*'} V^{-1} C^* P = 0. \quad (3.9)$$

If the system is  $(A^*, C^*)$  observable and  $(A^*, \Gamma)$  controllable, then  $P$  is positive definite. Under these assumptions, it can be shown that the difference between the internal state  $x$  and the estimated state  $\hat{x}$ , i.e. the error

$$e = x - \hat{x}, \quad (3.10)$$

goes to zero as time goes to infinity. In other words, the evolution equation

$$\dot{e} = A_f e + K_f v + \Gamma w, \quad (3.11)$$

is stable, i.e. all the eigenvalues of the matrix

$$A_f = A^* - K_f C^* \quad (3.12)$$

have negative real part.

Minimizing the infinite-time cost function  $J$ , (3.6) subject to (3.7) yields the following control law:

$$u = -K_c \hat{x}, \quad (3.13)$$

where

$$K_c = R^{-1}(B^{*'} S + N'), \quad (3.14)$$

and  $S$  is the solution of the algebraic Riccati equation (ARE)

$$A'^*S + SA^* + Q - (SB^* + N)R^{-1}(B'^*S + N') = 0. \quad (3.15)$$

It should be remarked that the control gain matrix  $K_c$  is determined from functions only of the known dynamic coefficients ( $A^*, B^*$ ) and weightings in the cost criterion ( $Q, R$ ), and not the statistics of the input ( $V, W$ ). Consequently,  $K_c$  is determined from a performance index such as (3.4), independent of the stochastic inputs. If ( $A^*, B^*$ ) is controllable and ( $A^*, Q^{1/2}$ ) observable, then the loop coefficient matrix

$$A_c = A^* - K_c B^* \quad (3.16)$$

is stable. The controllable and observable conditions can be weakened to stabilizable and detectable (Kwakernaak & Sivan 1972).

When we combine the estimator and the regulator, the dynamic system composed of the controlled process and filter becomes

$$\begin{pmatrix} \dot{e} \\ \dot{\hat{x}} \end{pmatrix} = \begin{bmatrix} A_f & 0 \\ K_f C^* & A_c \end{bmatrix} \begin{pmatrix} e \\ \hat{x} \end{pmatrix} + \begin{pmatrix} K_f v + \Gamma w \\ K_f v \end{pmatrix}. \quad (3.17)$$

Note that any choice of two among  $e$ ,  $\hat{x}$  and  $x$  produces the same dynamics because they are algebraically related by (3.10). Under the above controllability and observability assumptions,  $A_f$  and  $A_c$  have only stable eigenvalues if optimal gains  $K_f$  and  $K_c$  of (3.12), (3.16) are used. Other schemes such as  $\mathcal{H}_\infty$  could be proposed (Rhee & Speyer 1991), but from experience these schemes seem to produce only secondary modifications to the system performance over our LQG controller.

The infinite-time stationary formulation will be used in our study. The LQG control loop is shown in the block diagram of figure 2(b). Note that the cost function (2.44) can be expressed in the standard form (3.4), if we let

$$Q = C'^* C^*, \quad N = C'^* D^*, \quad R = (\gamma I + D'^* D^*). \quad (3.18)$$

Since the power spectral density is not known, for simplicity of the design we consider  $V$  and  $W$  to be of the form  $V = \alpha I$  and  $W = \beta I$  where  $\alpha$  and  $\beta$  are scalar and  $I$  is a unity matrix. Only the ratio of  $\alpha$  with  $\beta$  is important.

The process noise spectral density  $\beta$  and the weighting  $\gamma$  in the cost function are considered design parameters. The case where  $\gamma \rightarrow 0$  corresponds to unlimited control authority of the full-state feedback controller. The choice  $\Gamma = B^*$  allows for loop-transfer recovery (Doyle & Stein 1979). Loop-transfer recovery of the LQG controller to full-state feedback guarantees that robust performance occurs when the process noise goes to infinity, i.e.  $\beta \rightarrow \infty$ , provided there exists no non-minimal-phase zero in the plant. In our case, there are non-minimal-phase zeros, but a partial recovery is still shown to be possible (Turan, Mingori & Goodwin 1994).

As we have noted in §2, the analysis will be based on a single normal-mode model because the normal modes decouple. Although only one controller is needed at  $(Ra^*, k^*)$ , it is implemented for different  $k^*$  over a range of wavenumbers. The design point is determined so that when the controller is implemented, no unstable region appears below the neutral curve. Although the plant has multiple outputs, the system can be analysed in terms of robustness as a single-input/single-output (SISO) system by breaking the loop at the plant input (see figure 2b). We denote the output  $u$  of the controller by  $u_0$  and the input  $u$  to the plant by  $u_i$ . The open-loop system of equations formed by breaking the loop at the input to the plant is

$$\dot{x}_a = A_a x_a + B_a u_i, \quad u_0 = C_a x_a + D_a u_i, \quad (3.19)$$

where the augmented state composed of the plant and compensator in cascade is  $x_a = [x', \hat{x}']'$ . The coefficient matrices are given by

$$\left. \begin{aligned} A_a &= \begin{bmatrix} A & 0 \\ K_f C & (A^* - B^* K_c - K_f C^* + K_f D^* K_c) \end{bmatrix}, \quad B_a = \begin{bmatrix} B \\ K_f D \end{bmatrix}, \\ C_a &= [0, -K_c], \quad D_a = 0. \end{aligned} \right\} \quad (3.20)$$

The evolution equation for the closed-loop feedback system is

$$\begin{pmatrix} \dot{x} \\ \dot{\hat{x}} \end{pmatrix} = \begin{bmatrix} A & -BK_c \\ K_f C & (A^* - K_f C^* - B^* K_c + K_f (D^* - KD) K_c) \end{bmatrix} \begin{pmatrix} x \\ \hat{x} \end{pmatrix}, \quad (3.21)$$

where  $u_i = Ku_0$ . In the above equation, matrices with an asterisk superscript correspond to the design parameters  $k^*$  and  $Ra^*$ . Note that in the particular case when the plant operates at nominal design condition, i.e.  $k = k^*$ ,  $Ra = Ra^*$  and  $K = 1$ , the closed-loop poles will correspond to the ensemble of eigenvalues of  $A_f$  and of  $A_c$ . In other words, (3.21) reduces to (3.17) and the filter poles and regulator poles decouple. One can show this from the transformation

$$\begin{pmatrix} x \\ \hat{x} \end{pmatrix} = \begin{bmatrix} I & I \\ 0 & I \end{bmatrix} \begin{pmatrix} e \\ \hat{x} \end{pmatrix}, \quad (3.22)$$

where  $I$  is an identity matrix.

In general, the plant does not operate at the nominal design condition. Consequently, there is a mismatch between the parameters ( $k^*, Ra^*$ ) used to design the controller and the operating parameters ( $k, Ra$ ). Our analysis uses two methods to characterize the robustness of the stabilized system: neutral curves and gain and phase margins. In the first method, we select the nominal points ( $k^*, Ra^*$ ) and construct the region of stability of the dynamics system (3.21) as  $Ra$  and  $k$  vary with  $K = 1$ . The boundary of this region is where the real part of the least-stable closed-loop pole of (3.21) becomes zero. This boundary curve in the ( $k, Ra$ )-plane is called the neutral curve. We identify the minimum of  $Ra$  with respect to wavenumber on the neutral curve, so that the range of  $Ra$  from zero to this minimum, along with the whole range of wavenumbers, is stable. By robustness we mean constructing the largest range of  $Ra$  from zero up to this minimum.

The second method used to estimate robustness is the classical gain and phase margins approach. This approach allows us to characterize robustness with respect to more general uncertainties, such as unmodelled dynamics. To obtain the gain and phase margins, we consider an error model  $K = |K|e^{i\phi}$  (see figure 2b), with the plant operating at the nominal parameters  $k = k^*$  and  $Ra = Ra^*$ . The shifts of  $|K|$  and  $\phi$  from these nominal values ( $|K| = 1$ ,  $\phi = 0$ ) to where the system becomes unstable are essentially the gain and phase margins, respectively. Their values can be determined from accompanying Nyquist plots. The gain and phase margins are defined explicitly in §4.2.1 where these values indicate the amount of gain and phase change that the system can tolerate due to uncertainties in the system dynamics.

#### 4. Results

In this paper, we consider the condition of  $Pr = 7$  which enables us to compare our numerical results with those of Tang & Bau (1994, 1998b) and Howle (1997a). In their experiments, however, Howle (1997b, c) used a high- $Pr$  fluid ( $Pr \approx 200$ ) whereas

in Tang & Bau (1998a) the  $Pr$  value of their testing fluid was not given. It should be noted that while the stability properties in the uncontrolled case are independent of  $Pr$ , they are  $Pr$  dependent in the controlled case.

Our numerical results have been obtained using  $N_z = 26$  (see § 2.4) which appears to be adequate for our stability analysis. For example, consider the closed-loop eigenvalue problem of (3.21) with controller design values  $Ra^* = 14.8Ra_{c0}$  and  $k^* = 3.15$  and the system evaluated at  $k = 5.5$  and  $Ra = 14.52$  which lies on the neutral curve (see figure 8(d)), the norm of eigenvector (square root of the mean-square sum of entries) of the neutral eigenvalue of the coefficient matrix of (3.21) appears well converged. When  $N_z = 26$  is increased to 52, this norm changes only by less than 0.7%.

#### 4.1. Proportional feedback control

For convection in a layer of fluid bounded by rigid walls with prescribed temperatures, it is well known that the critical Rayleigh number  $Ra_{c0} = 1707.76$  occurs at wavenumber  $k_{c0} = 3.117$  (Chandrasekhar 1961). Instead, when heat flux is prescribed at the lower wall, the critical value  $Ra_{c0} \approx 1295.78$  occurs at  $k_c = 2.552$ .

In the case of proportional feedback control, the control law is  $u = -K_p z$ , where  $K_p$  is a constant proportional gain. We consider the planar sensor model to illustrate the effects of feedback control upon stability, and the results are shown in figure 3(a).

In this figure three neutral curves are shown: each curve consists of a heavy and a thin solid line, representing a monotonic mode and an oscillatory mode of convection, respectively. The oscillatory mode corresponds to a complex conjugate pair of eigenvalues. The three curves correspond to three sensor locations:  $z_s = 0$  at the mid-plane and  $z_s = \pm 0.1$ . The offset with respect to the mid-plane is 10% of the thickness of the fluid layer and gives a substantial shift in stability properties. The unstable and stable regions are separated by a neutral curve and are identified by the letters U and S, respectively. In each case the maximum  $Ra$  achievable corresponds to the crossing point between the heavy and thin line.

For  $z_s = 0$ , the monotonic mode is the lowest even mode of convection since the first odd mode is unobservable. In fact, in this case the sensor plane coincides with the node of the first odd mode. As  $K_p$  increases beyond the crossing point the critical  $Ra$  decreases. With this in mind, a pole-zero map and a root locus diagram are helpful to understand the stability behaviour. Figure 3(b) shows the open-loop poles ( $\times$ ) and zeros ( $\circ$ ) and figure 3(c) the corresponding root locus diagram. For a given  $Ra$ , as  $K_p$  increases from zero the unstable pole moves to the left while a stable pole moves to the right. Subsequently, the two poles coalesce. After coalescence a pair of complex conjugate poles (corresponding to the oscillatory mode) break off the real axis. The break-away point (where the coalescence occurs) moves to the right as  $Ra$  increases. The crossing point in figure 3(a) corresponds to the coalescence at the origin in figure 3(c). As  $Ra$  increases and keeping  $K_p$  constant, the closed-loop poles move to the right.

From the root locus of figure 3(c), the results of figure 3(a) can be interpreted as follows. For  $Ra$  above the crossing point, the system is unstable for any gain  $K_p$ . For  $Ra$  below the crossing point, there exists a finite range of gain  $K_p$  in which the system is stable. The lower end point of the range corresponds to the minimal value of  $K_p$  required in order to move the monotonic pole to left-half  $s$ -plane. The upper end point of the range corresponds to the maximal value of  $K_p$  that can be used before the pair of complex conjugate modes become unstable.

The stability diagram for the shadowgraph sensor model can be found in Howle



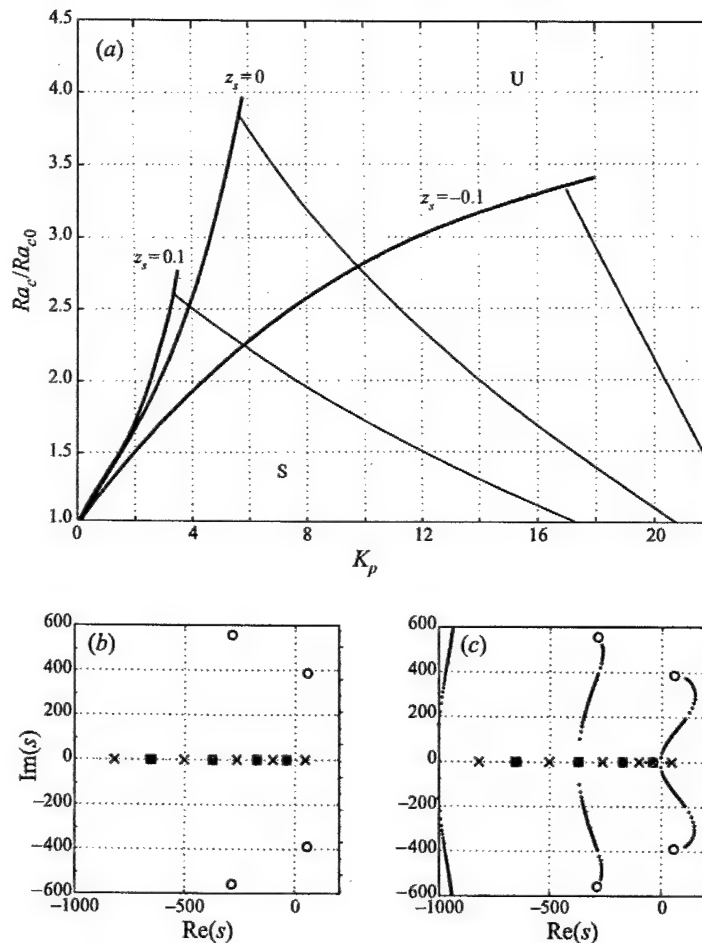


FIGURE 3. (a) Neutral curves for the planar sensor model using the proportional feedback control, corresponding to  $z_s = -0.1, 0$  and  $0.1$  (heavy and thin lines indicate monotonic and oscillatory onset, respectively). (b) Pole-zero diagram of the plant for  $k = 4.4$ ,  $Ra = 3.5Ra_{c0}$  and (c) corresponding root loci for  $K_p$  varied between 0 and 2000.

(1997a). In this case there are no unstable complex conjugate modes. As  $K_p$  increases to  $\infty$ , the critical  $Ra$  increases monotonically to about 3.13 times  $Ra_{c0}$ .

#### 4.2. LQG ( $\mathcal{H}_2$ ) control

The limitation in the performance of proportional feedback control provides the motivation for developing LQG controllers. We will apply the LQG synthesis method to both planar sensor and shadowgraph sensor models. We first seek to reduce the number of design parameters in our analysis. For a given set of physical parameters we examine the closed-loop eigenvalues and observe that for a stable system the real part of the least-stable eigenvalue has its largest magnitude when  $\gamma \rightarrow 0$  and  $\beta \rightarrow \infty$ . Since the observed improvements become less significant for  $\gamma < 0.1$  and  $\beta > 100$ , we let  $\gamma = 0.1$  and  $\beta = 100$ .

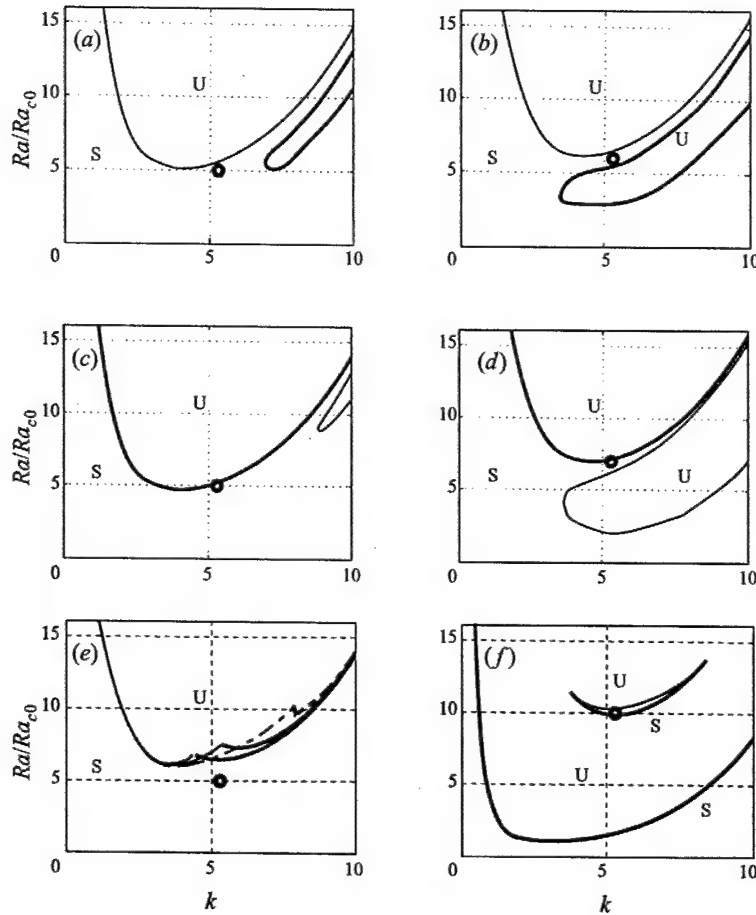


FIGURE 4. Stability diagrams for the planar sensor model with one sensor, using the LQG control. The nominal condition  $(k^*, Ra^*)$  is denoted by a solid circle. The heavy and thin lines correspond to the monotonic and oscillatory onsets, respectively. (a, b, f)  $z_s = 0.15$  and (c, d)  $z_s = -0.15$ . (a-e)  $Ra^* = 5Ra_{c0}$  and  $k^* = 5.3$  and (f)  $Ra^* = 10Ra_{c0}$  and the same  $k^*$ . In (e) the sensitivity about  $z_s = 0$  with respect to  $z_s$  is shown. In (f) a vast lower unstable region developed at a sufficiently high  $Ra^*$  is shown.

#### 4.2.1. Planar sensor model

##### (i) One-sensor control

The one-sensor model is especially convenient for understanding the closed-loop stability properties of the system. Once the qualitative properties of this case are understood, the performance of the controller will be improved by adding additional sensors.

Figure 4(a-f) shows the neutral stability diagram in the  $(k, Ra)$ -plane for a controller designed at the nominal values  $k^*$  and  $Ra^*$ . The nominal point  $(k^*, Ra^*)$  is indicated by a solid circle in the figures. The thin line and heavy line curves correspond to the neutrally stable oscillatory and monotonic modes, respectively. In figure 4(a, b) the sensor plane is located at  $z_s = 0.15$ . We use a larger sensor displacement with

respect to the mid-plane than the one used for the proportional feedback control to emphasize the effect on the neutral curve. Figure 4(a) shows the neutral curves for a controller designed at the nominal point  $Ra^* = 5Ra_{c0}$  and  $k^* = 5.3$ . The neutral curves have two minima, and the value  $k^* = 5.3$  has been chosen to make the minima nearly the same. The controller stabilizes the system for any  $Ra < Ra^*$ . To characterize the stability of the controlled system with respect to  $Ra^*$ , we re-design the controller for  $Ra^* = 6Ra_{c0}$  while maintaining  $k^*$  fixed. Figure 4(b) shows a dramatic change in the neutral curve: the banana-shaped branch moves downward giving rise to an unstable region below  $Ra^*$ .

To further characterize the stability of the controlled system with respect to the location of the sensor, we move the sensor plane at  $z_s = -0.15$ . We design a controller for  $k^* = 5.3$ , as before, and  $Ra^* = 5Ra_{c0}$  (figure 4(c)) and  $Ra^* = 7Ra_{c0}$  (figure 4(d)). Figures 4(c) and 4(d) show similar stability characteristics as those in figures 4(a) and 4(b). However, the two branches of the neutral stability curves switch roles. The left branch now represents the monotonic onset while the right branch represents the oscillatory onset.

The role switch in relation to the location of the sensor plane deserves a closer examination. We consider a smaller perturbation of the sensor location with respect to the mid-plane. Figure 4(e) shows the stability limits for three very close sensor locations. At  $z_s = 0$  (solid lines), the neutral curve is composed of an oscillatory segment on the left and a monotonic segment on the right. At  $z_s = 0.005$  (dashed-dotted lines), the monotonic segment of the neutral curve retreats rightward while the oscillatory segment dominates the range. At  $z_s = -0.005$  (dashed lines), the opposite effect occurs: the oscillatory segment of the neutral curve retreats to the left. These results are consistent with the results presented in figures 4(a-d). Since significant distortions and shifts of the stability limits have occurred within a very small perturbation of  $z_s$ , sensitivity to sensor location becomes an important factor for the practical implementation of the sensors. As subsequent results will show, this type of sensitivity is no longer present if three sensors are incorporated.

In order to show that the lower unstable region will become much larger with further increase of  $Ra^*$ , we design a controller at the nominal values  $Ra^* = 10Ra_{c0}$  and  $k^* = 5.3$  and place the sensor plane at  $z_s = 0.15$  for an illustration. Figure 4(f) shows a thin island of stability in the unstable region. This stable region is bounded by two neutral curves which coalesce on the right and intersect on the left. Figure 4(a-f) reveals the occurrence of an unstable region at  $Ra < Ra^*$  which severely restricts the achievable degree of stabilization.

The results of proportional feedback control have demonstrated the significance of the sensor location at  $z_s = 0$ . This location gives the maximum range of stabilization even for the LQG controller. We observe that  $Ra^*$  can be raised to  $10Ra_{c0}$  at properly chosen values of  $k^*$  (see figure 5a-c) without inducing a large lower unstable region, if the sensor is placed at the mid-plane. At this  $Ra^*$ , the system is stable up to the critical  $Ra$  of the first odd mode ( $Ra_c \approx 10.31Ra_{c0}$  and  $k_c = 5.36$ , see Chandrasekhar 1961), since the first odd mode is not stabilizable because it is unobservable.

Hence, there is no reason to place  $Ra^*$  above  $10.31Ra_{c0}$ . Below this value, however, the critical point of the neutral curve lies to the right of the nominal point if  $k^*$  is sufficiently small, or to the left of the nominal point if  $k^*$  is sufficiently large. For this case, we can use two nominal points to lift the overall neutral curve to coincide with the neutral curve of the first odd mode.

Consider  $Ra^* = 10Ra_{c0}$ , just below the  $Ra_c$  of the first odd mode. We choose the two nominal  $k^*$  on both sides of  $k_c = 5.36$ . The values  $k^* = 4$  and 6 (marked by solid

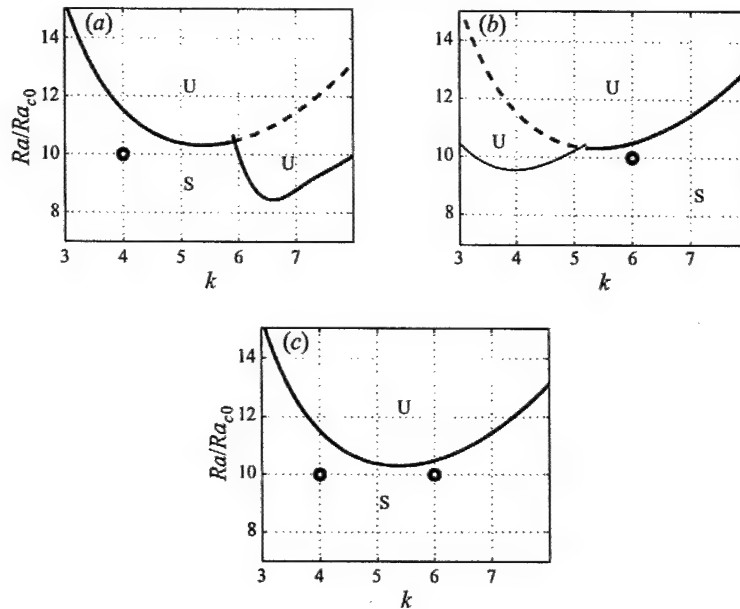


FIGURE 5. Stability diagrams for the planar sensor model with a single mid-plane sensor: (a) neutral curve for the nominal condition  $k^* = 4$  and  $Ra^* = 10Ra_{c0}$ ; (b) neutral curve for the nominal conditions  $k^* = 6$  and  $Ra^* = 10Ra_{c0}$ ; (c) the resulting neutral curve by incorporating the two sets of nominal conditions. This curve coincides with the neutral curve of the first odd mode of convection in the uncontrolled case.

circles) produce small dips in the unstable region and are reasonable to use as nominal points. Figure 5(a-c) illustrates how the stability limit is determined by the principle of superposition. The nominal point at  $k^* = 4$  in figure 5(a) corresponds to the unstable region delimited by the heavy solid lines which has a minimum  $Ra \approx 8.4Ra_{c0}$ . For  $k < 5.9$ , the stability limit corresponds to the neutral curve of the first odd mode. Similarly, in figure 5(b) the second nominal point at  $k^* = 6$  corresponds to the unstable region delimited by the thin and heavy solid lines which has a minimum at about  $9.5Ra_{c0}$ . The thin curve corresponds to an oscillatory onset. The heavy curve coincides with a segment of the neutral curve of the odd mode. If both nominal points are used for the controllers, then the overall stability limit coincides with the neutral curve of the first odd mode upon superposition. The controllers designed at the first nominal point  $k^* = 4$  operate over the band  $0 < k < k_c \approx 5.36$ , while the controller designed at  $k^* = 6$  operates over the wavenumbers greater than  $k_c$ .

The result shows that the degree of stabilization is significantly higher than that achievable with the proportional control. Unfortunately, the one-sensor design is not sufficiently robust with respect to the location of the sensor plane. This problem is significant because a perfect sensor placement is not achievable in practice. To demonstrate the sensitivity, in figure 6(a) we consider a planar sensor at  $z_{sl} = 0.01$ , i.e. slightly off the mid-plane, and re-design the controller for  $Ra^* = 10Ra_{c0}$  and  $k^* = 4$ . Figure 6(a) shows the presence of a thin stable region in the middle of the unstable region. This stable region is bounded from above by a neutral curve of an oscillatory mode (thin line) and below by a neutral curve of a monotonic mode (heavy solid

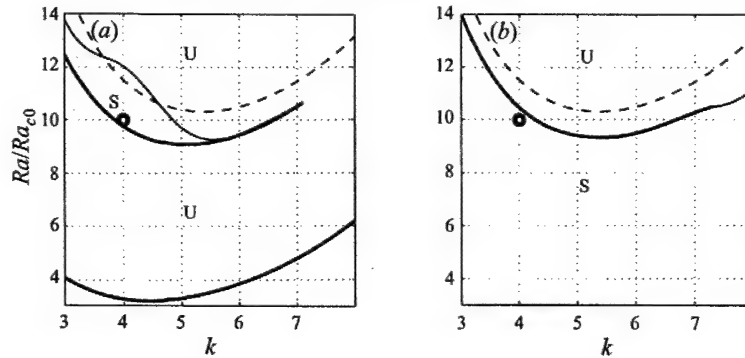


FIGURE 6. (a) Stability diagram for the one-sensor model with a small offset  $z_s = 0.01$ . Results show a vast lower unstable region below  $Ra^* = 10Ra_{c0}$ . The heavy (thin) solid line corresponds to a monotonic (oscillatory) onset. (b) Stability diagram for the two-sensor model, with a second sensor positioned at  $z_s = -0.01$ . As a result, the lower unstable region is eliminated.

line). The stable region exists for  $k < 3$ . As  $k$  increases it becomes a very narrow strip which eventually terminates at  $k \approx 7.1$ , similar to the behaviour in figure 4(f). For comparison the neutral curve for the  $z_s = 0$  case (thin dashed line) is also included in figure 6(a). Comparing figure 6(a) to figure 5(c), we see a dramatic difference in stability properties due to a small shift of sensor location of 0.01. Fortunately, this sensitivity can be significantly reduced by introducing a second sensor located close to the mid-plane. Figure 6(b) shows the stability diagram when a second sensor is included. This case will be discussed in the next subsection.

To characterize the robustness of the controlled system with respect to plant uncertainties we compute gain and phase margins at  $Ra = Ra^*$  and  $k = k^*$ . In all the cases considered, the open-loop system has one unstable pole so that for closed-loop stability the Nyquist locus encircles (counter-clockwise) the point  $(-1, 0)$  once. Because of this property, in general there exists an upper and lower value for each gain and phase margin. The upper and lower gain margins are designed to measure how much the gain  $K$  can be decreased, or increased, before the system becomes unstable (figure 2b). Likewise, the upper and lower phase margins are designed to measure how much the phase can be decreased, or increased, before the system becomes unstable. Accordingly, the lower and upper gain margins are defined as  $20 \log_{10}(1/X_1)$  (dB) and  $20 \log_{10}(X_2)$  (dB), respectively, where  $X_1$  ( $|X_1| < 1$ ) and  $X_2$  ( $|X_2| > 1$ ) are the smaller and larger  $x$ -distances of the two crossing points of the Nyquist locus with the  $x$ -axis. Since the angle is measured positive in the counter-clockwise direction, the lower phase margin is defined as  $180^\circ - \sin^{-1}(Y_1)$  and the upper phase margin is defined as  $\sin^{-1}(Y_2) - 180^\circ$ , where  $Y_1$  (positive) and  $Y_2$  (negative) are, respectively, the  $y$ -coordinates of the intersecting points between the Nyquist locus and the unit circle centred at origin.

For the one-sensor model, the gain and phase margins are too small. At  $Ra = Ra^* = 10Ra_{c0}$ , for example, the margins are typically about 0.5 dB and  $4^\circ$ . In engineering applications, margins below 3 dB and  $10^\circ$  are often considered marginal. Therefore, we conclude that as the system is stabilized for higher values of  $Ra$ , the magnitude of the gain increases, increasing the sensitivity, as indicated by the very small gain and phase margins. Sensitivity can be reduced by implementing multiple sensors, as indicated by the improved gain and phase margins (see next subsections).

## (ii) Two-sensor control

To eliminate the lower unstable region shown in figure 6(a), we place two sensors on opposite sides of the mid-plane at  $z_s = \pm 0.01$ . It is crucial that both sensors are close to the mid-plane. Placement of one sensor or both away from the mid-plane will give rise to a lower unstable region.

In the two-sensor model we re-design the controller at the nominal condition used for the case shown in figure 6(a). The two-sensor model result is shown in figure 6(b), in which the same dashed curve as in figure 6(a) is included for comparison. We observe that the lower unstable region has disappeared. The neutral curve of the monotonic mode (heavy solid line) terminates at  $k \approx 7.3$ . Beyond this wavenumber the neutral curve of an oscillatory mode replaces the stability limit (thin solid line). If we allow  $z_s$  to tend to zero, then the solid curve in figure 6(b) will approach the dashed curve. The gap between the two curves indicates that there is a trade-off between the large pole shifts due to the small sensor-plane offset, and the information gained by adding one more sensor near to the mid-plane. The gain and phase margins increase by roughly 10% to 20% by adding the second sensor. However, the improvements are still too small to be considered acceptable.

Better gain and phase margins (over 100% increase) can be obtained with sensors placed further away from the mid-plane. The sensors located at about  $z_s = \pm 0.25$  appear to give the best result. However, in this case a lower unstable region forms. The two-sensor model is still not suited for practical implementation. For this reason, we shall not devote more effort to analysing this case. Instead, we proceed to the three-sensor model.

## (iii) Three-sensor control

When three sensors are used, we can improve gain and phase margins by placing two outer sensors further away from the mid-plane without inducing any lower unstable region, provided that the remaining sensor is placed at the mid-plane. With two sensors placed significantly away from the mid-plane, it is observed that the sensor located at the mid-plane is no longer sensitive to a small offset. To determine the best sensor locations, we first observe that a lower unstable region always occurs when no sensor is placed at or very close to the mid-plane. With a mid-plane sensor in place, then by fixing one outer sensor and moving the other, it appears that the best locations are when the two outer sensors are at equal distance from the mid-plane. The best locations are determined in terms of the minimum of the real part of the least-stable closed-loop pole. Hence, for our design, we let the three sensor locations be  $z_s^{(1)} = -z_s$ ,  $z_s^{(2)} = 0$  and  $z_s^{(3)} = z_s$ .

In order to improve gain and phase margins, we consider the Nyquist plots for various values of  $z_s$ . In the subsequent results concerning the stability limit of the controlled system (see figure 8), a good nominal condition is found to be  $k^* = 3.15$  and  $Ra^* = 14.8$ . For this nominal condition, figure 7(a) shows the Nyquist curves for  $z_s = 0.1$  (dotted), 0.2 (dashed) and 0.3 (solid). Figure 7(b) provides a magnified view of figure 7(a) near the point  $(-1, 0)$ . The case  $z_s = 0.3$  presents no lower phase margin but has an upper phase margin of about  $20.5^\circ$ . The upper and lower gain margins are about 3.3 dB and 4.4 dB, respectively. These values of gain and phase margins are quite satisfactory. A slight improvement of the margins is still possible by increasing  $z_s$  further, at the expense of increasing the real part of the least-stable pole closer to zero, thus making the system less stable. Thus,  $z_s = 0.3$  appears to be our best choice. It is desirable to see how changing the values of  $k^*$  and  $Ra^*$  will affect the gain and phase margins for  $z_s = 0.3$ . In figure 7(c) we compare the Nyquist curves for three different nominal conditions:  $k^* = 3.15$  and  $Ra^* = 14.8Ra_{c0}$  (solid),



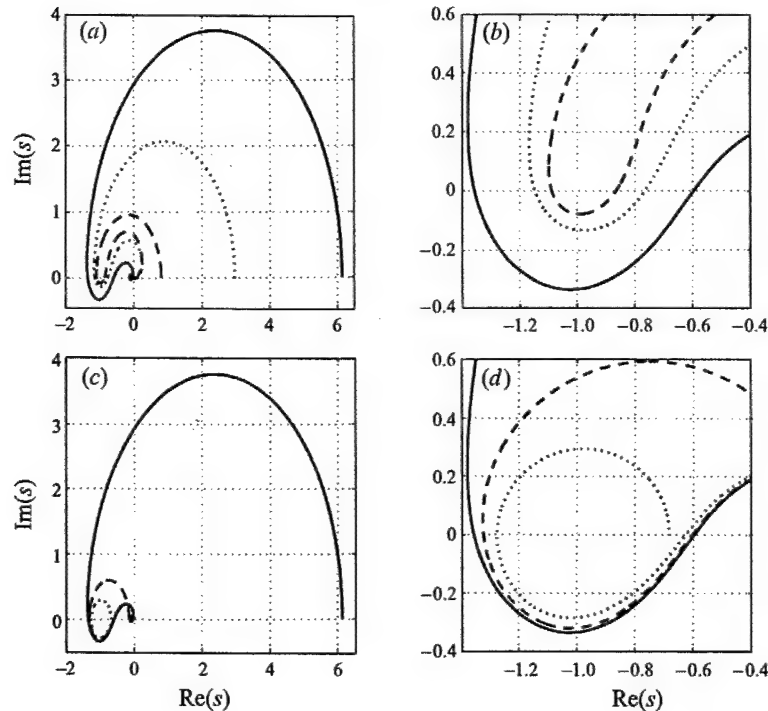


FIGURE 7. Nyquist plots for the three-sensor model: (a) at nominal condition  $k^* = 3.15$  and  $Ra^* = 14.5Ra_{c0}$  and sensor locations are  $z_s = 0.1$  (dashed),  $0.2$  (dotted) and  $0.30$  (solid); (b) magnified view of (a); (c) at  $z_s = 0.3$  and nominal conditions with  $k^* = 3.15$  and  $Ra^* = 14.5Ra_{c0}$  (solid),  $k^* = 4.5$  and  $Ra^* = 12.5Ra_{c0}$  (dashed) and  $k^* = 6.5$  and  $Ra^* = 15Ra_{c0}$  (dotted); (d) magnified view of (c).

$k^* = 4.5$  and  $Ra^* = 12.5Ra_{c0}$  (dashed) and  $k^* = 6.5$  and  $Ra^* = 15Ra_{c0}$  (dotted). This choice of nominal points is based on the subsequent analysis of the stability limit of the controlled system. As shown in the magnified view of figure 7(d), the upper phase margin and the upper and lower gain margins for the three nominal conditions are quite close, suggesting that these margins are not sensitive to the values of  $k^*$  and  $Ra^*$ . However, the lower phase margin decreases rapidly as  $k^*$  and  $Ra^*$  increase, as shown by the dotted line. The gain and phase margins for the design case (solid) are within values used in practice.

Now, we consider the stability limit of the controlled system. In order to understand how the choice of the nominal condition ( $k^*, Ra^*$ ) affects stability, we present the results for each set of nominal condition in figures 8(a)–8(c).

For each nominal point the stable region is delimited by the neutral curve. Our goal is to maximize the minimum of the neutral curve by appropriately choosing the nominal point. In figure 8(a) we consider  $k^* = 3$  and  $Ra^* = 15Ra_{c0}$ . There is no unstable region to the left of this nominal point and the neutral curve to its right corresponds to an oscillatory mode. The neutral curve in figure 8(b) corresponds to  $k^* = 4.5$  and  $Ra^* = 12.5Ra_{c0}$ . An unstable banana-shaped region (monotonic onset) is present on each side of the main unstable region. The minimum of the main unstable region is about  $Ra \approx 14.5Ra_{c0}$ . We have decreased  $Ra^*$  from  $15Ra_{c0}$  to  $12.5Ra_{c0}$

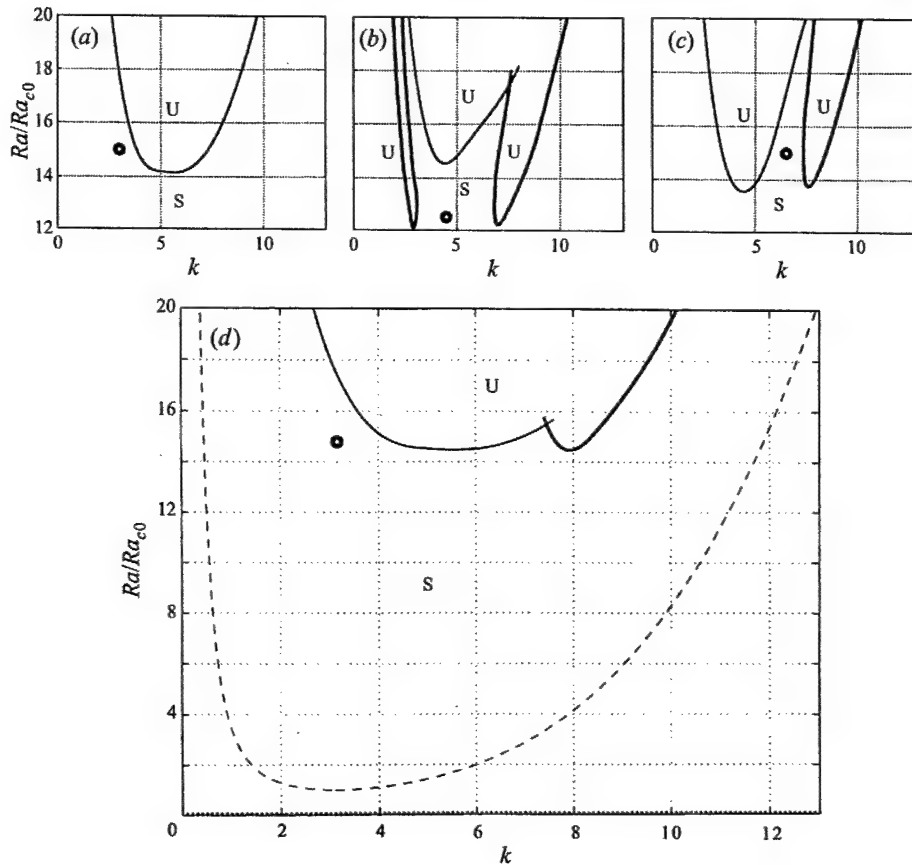


FIGURE 8. The stability diagrams for the three-sensor model with sensor planes located at  $z_s = -0.3$ , 0 and 0.3, and nominal conditions at (a)  $k^* = 3$  and  $Ra^* = 15Ra_{c0}$ , (b)  $k^* = 4.5$  and  $Ra^* = 12.5Ra_{c0}$ , (c)  $k^* = 6.5$  and  $Ra^* = 15Ra_{c0}$ , (d)  $k^* = 3.15$  and  $Ra^* = 14.8Ra_{c0}$  (the design conditions).

because at  $Ra^* = 15Ra_{c0}$  (not shown) the two banana-shaped unstable regions have merged generating a vast lower unstable region. However, because of the formation of an unstable region on each side, this nominal point is not desirable. Figure 8(c) shows the neutral curve for the system controlled by controllers designed at nominal condition  $k^* = 6.5$  and  $Ra^* = 15Ra_{c0}$ . The banana-shaped region on the left of the nominal point has disappeared, but the region on the right remains.

By considering additional nominal points to the right of the first nominal point it seems that there is no significant improvement in stability. In other words, when the nominal wavenumber  $k^*$  is larger than a certain value, the controllers become ineffective in stabilizing the entire region up to  $Ra = Ra^*$ , even though better local stabilization is always possible. Based on the results of figures 8(a)–8(c), it appears that nominal points to the right of the first point do not improve the situation. In fact, we have tried more cases involving different locations of the nominal points, but none seems to raise the minimum  $Ra$  of the unstable region. To achieve a maximum  $Ra$  for the stable range, we fine-tune the first nominal point and obtain  $k^* = 3.15$

and  $Ra^* = 14.8Ra_{c0}$ . For this point the stability diagram is shown in figure 8(d). Stabilization up to  $Ra \approx 14.5Ra_{c0}$  is achievable by using controllers designed at only one nominal point. The neutral curve is formed by an oscillatory mode (thin solid line) and a monotonic mode (heavy solid line). To illustrate the degree of stabilization with respect to the uncontrolled system, we include in the figure the neutral curve (dashed line) for the uncontrolled convection. Without feedback control, the region above the dashed curve is unstable to convection. Below the solid curves, however, the region is stabilized by the LQG control.

In §2, we described how in the practical implementation a controller is responsible for stabilizing an unstable normal mode whose wavenumber is indicated by a point on the  $k$ -axis in figure 8(d). Results suggest that we can use the design condition  $k^* = 3.15$  and  $Ra^* = 14.8Ra_{c0}$  for all controllers. Coincidentally, we note that the design wavenumber,  $k^* \approx 3.15$ , is quite close to the critical wavenumber of the uncontrolled convection,  $k_{c0} \approx 3.12$ .

We conclude the analysis of the planar sensor model by discussing the time response of the closed-loop system. Our design condition is at  $k^* = 3.15$  and  $Ra^* = 14.8Ra_{c0}$ . For high operating values of  $Ra$ , if we turn on the controller at this design condition with no initialization of the estimator, the transient response of the controlled system induces a large actuator signal  $u(t)$ , which will produce actuator saturation in practical applications. Therefore, in practical applications, the operating  $Ra$  value should be achieved in increments of  $Ra$ , so that for each increment the estimator remains initialized. For example, consider a controller operating at  $k = k_c \approx 5.5$ . Assume that we have increased the operating  $Ra$  value gradually up to  $Ra = 12Ra_{c0}$  so that the closed-loop system remains at the no-motion equilibrium. When approaching equilibrium, both the plant internal states and the estimator states tend to zero. As an example, we increase  $Ra$  from  $Ra = 12Ra_{c0}$  by an increment of  $2Ra_{c0}$  to the operating value  $Ra = 14Ra_{c0}$ . Figure 9 shows the transient time responses for this case. In particular, figure 9(a) shows the temperatures measured by the planar sensors as functions of time, while figure 9(b) shows the control action signal  $u(t)$ . The initial transient disappears and the system settles to a new no-motion equilibrium. If we use a smaller increment than  $2Ra_{c0}$ , an even better result can be expected in terms of smaller overshoot and a faster approach to equilibrium.

It is important to consider the parameters in a physical set up to see if the LQG controller can be applied to an experiment. We note that  $t$  is in the unit of diffusive time,  $d^2/\kappa$ . For example, in the case of a layer of water of thickness  $d = 0.8$  cm, this unit is about 438 s. A mildly supercritical condition  $Ra \approx 1800$  corresponds to  $\Delta T^* = 0.14^\circ\text{C}$ , while for  $Ra = 14Ra_{c0}$ , the basic temperature difference is about  $1.86^\circ\text{C}$ . Thus, the physical quantities are reasonably easy to achieve in practice.

Comparison between the stability achievable by the proportional feedback control (Tang & Bau 1993, 1994 as well as our figure 3a) and the LQG control is possible only from a qualitative point of view. The LQG controller is more complex, due to the additional filter dynamics. The neutral curve structure is complex because the unstable regions can occur above and below the design value  $Ra^*$ . However, a local stable region about  $Ra^*$  can always be maintained. In contrast, for proportional feedback there is no stable region beyond a certain value of  $Ra$ , regardless of the gain  $K_p$ .

#### 4.2.2. Shadowgraph sensor model

We now turn to the shadowgraph sensor model. The maximum  $Ra$  achievable over the stable range for the proportional feedback control is about  $3.13Ra_{c0}$ . We attempt

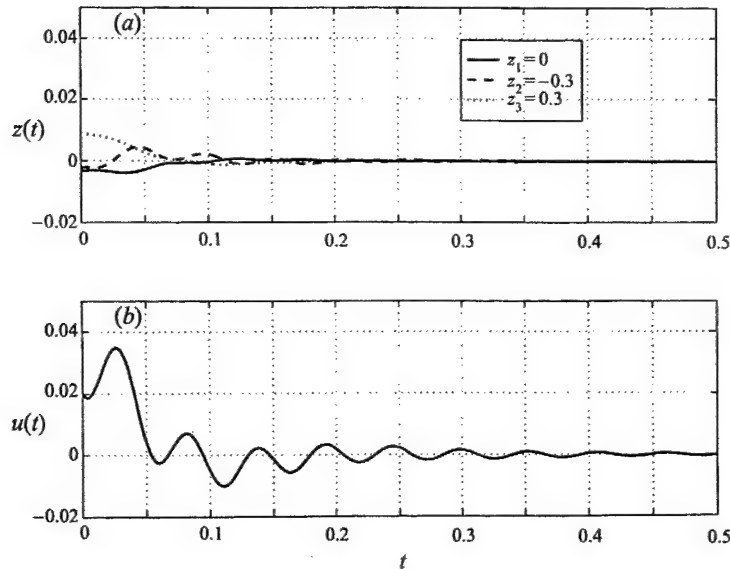


FIGURE 9. The time response of (a) the three measurements and (b) the control action  $u(t)$ , in the three-sensor model with the nominal condition  $k^* = 3.15$  and  $Ra^* = 14.8Ra_{c0}$ . The convection mode considered is at  $Ra = 14Ra_{c0}$  and the least-stable wavenumber about  $k = 5.5$ .

to increase the stable region using the LQG method. However, for this sensor model our results indicate a significantly weaker stabilization. We have first designed a controller for  $Ra^* \approx 10Ra_{c0}$  but encountered a vast lower unstable region. The second convection mode, which is closest to the imaginary axis, is destabilized in the control process. As a result, we gradually decreased the nominal condition  $Ra^*$ , down to a value of  $5Ra_{c0}$ . The drop in performance in the critical Rayleigh number with respect to the planar sensor model is probably due to the nature of the shadowgraph sensor, which only measures the averaged temperature of the fluid layer. Figure 10(a) shows the stability diagram when controllers designed at five nominal points are used. The nominal points have same  $Ra^*$  while  $k^*$  increases by a factor  $\Delta k^* = 1$ . The results show that, except for the first nominal point ( $k^* = 1$ ), each nominal point is enclosed by a left and a right stability limit (thin line for oscillatory mode and heavy line for monotonic mode). The stable range of wavenumbers associated with each nominal point is typically small. Figure 10(a) reveals two depressed unstable regions that reach below  $Ra = Ra^*$  (near  $k = 2.4$  and  $k = 3.4$ ). To demonstrate how these dips can be removed, we add two more nominal points: one is chosen at  $k^* = 2.4$  and the other at  $k^* = 3.3$ , both with a slightly higher  $Ra^* = 5.4Ra_{c0}$ . The improved result is shown in figure 10(b), which indicates that the minimum  $Ra$  of the unstable region is now above  $5Ra_{c0}$ .

Unlike the planar sensor model, the minimum  $Ra$  of the neutral curve obtained by applying a controller designed at a single nominal point over the whole wavenumber range is not that much higher than the value obtained using proportional feedback control. There may be further improvements on the LQG controller to be made, but we will not attempt further design in this study.

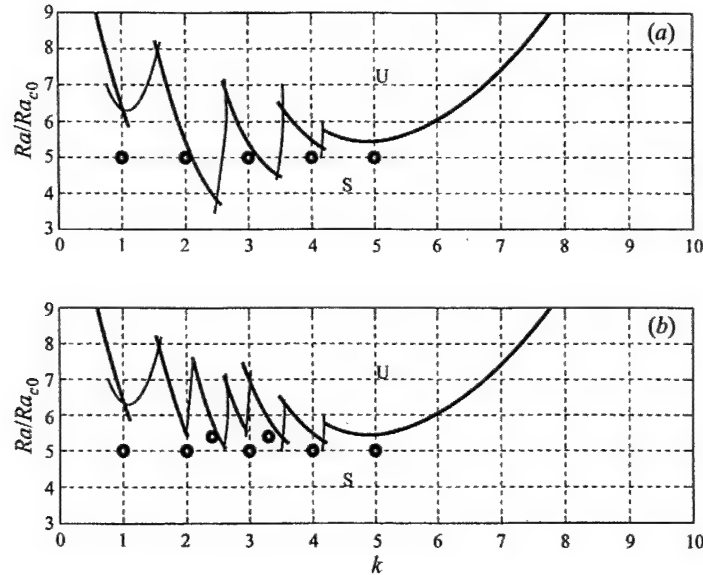


FIGURE 10. (a) The stability diagram for the shadowgraph sensor model showing the stability limit corresponding to five equally spaced nominal points at  $Ra^* = 5Ra_{c0}$ . (b) An improved design with two nominal points added. Stabilization for the entire range of wavenumbers up to  $Ra^* = 5Ra_{c0}$  is achievable for this improved case.

## 5. Conclusion

We have investigated the LQG ( $\mathcal{H}_2$ ) controller design for two sensor models (planar sensor model and shadowgraph sensor model) studied by previous authors (Tang & Bau 1994; Howle 1997a) using proportional controllers. Based on our results for  $Pr = 7$ , we have shown that the robustness of the controlled system is improved in two aspects: (i) the controller remains stable over a larger range of the parameter  $Ra$ , and (ii) the robustness of the controller accommodates to a degree unmodelled dynamics and nonlinearities, as measured by gain and phase margins on the Nyquist diagram. It should be noted that although only one controller is needed to be designed at  $(k^*, Ra^*)$ , this controller is implemented at each wavenumber  $k$  to span the entire range of unstable wavenumbers.

The number of sensors plays an important role in dramatically improving the robustness of the stabilization of the system operating at large  $Ra$ . Because multiple sensor planes can be easily incorporated into the planar sensor model, the performance of the planar sensor model is found to be superior to that of the shadowgraph sensor model, which only utilizes averaged temperature measurements. By using three planar sensors, it is possible to stabilize the no-motion state up to  $Ra \approx 14.5Ra_{c0}$ . The controller has 3 dB of gain margin and  $20^\circ$  of phase margin at the design parameter values. Beyond this value of  $Ra$ , stabilization in the region near to a nominal point can still be achieved, but an unstable region forms for  $Ra$  below  $Ra^*$ . It should be noted that in our design procedure, we designed the controllers to span the whole range of unstable wavenumbers and at the same time demanded that the whole  $Ra$  range from zero up to  $14.5Ra_{c0}$  be stable.

defined as the value of temperature gradient at either upper or lower wall,

$$Nu = 1 + \sum_{n=0}^N \theta_{00n} \frac{dT_n(z)}{dz} \Big|_{z=0,1}, \quad (3.1)$$

where the first 2 zero indices of  $\theta_{00n}$  correspond to  $k = m = 0$  so that the sum represents the temperature gradient averaged over the horizontal plane. In the absence of internal heat source the values of  $Nu$  evaluated at  $z = 0$  and  $z = 1$  should be equal. Our open-loop, steady state solutions are obtained at truncation numbers  $K = 16$ ,  $M = 8$  and  $N = 16$ , for  $\alpha_x = 3.117$  and  $\alpha_y = 0$  (transverse rolls). In Table 1 the values published in Clever & Busse (1974) are shown in parenthesis. In all cases, the difference between our and their values is less than 0.4%. For values of wavenumber  $\alpha_x = 2.2$  and 2.6, respectively, where  $Pr = 7$  and  $Ra = 10000$ , we obtain  $Nu = 2.465$  and 2.548 versus their values 2.473 and 2.557. We further note that  $Nu$  should not depend on the orientation of rolls. As a consistency check, we compare the  $Nu$  of our solutions between the longitudinal ( $\alpha_x = 0, \alpha_y \neq 0$ ) and transverse rolls ( $\alpha_x \neq 0, \alpha_y = 0$ ). The difference of the  $Nu$  values is found less than 0.02%.

Ra	Pr=0.71	Pr=7.0
2000	1.210 (1.212)	1.214 (1.214)
2500	1.472 (1.475)	1.475 (1.475)
10000	2.653 (2.661)	2.608 (2.618)

Table 1: Nusselt Number Values for 2D rolls

#### (b) proportional feedback control

We now turn to the proportional feedback control problem. From the results of Tang & Bau (1994) and our results in Or et al. (2001) the oscillatory convection occurs when the proportional gain  $K_p$  becomes sufficiently large. At  $K_p = 6$ , for instance, the linear



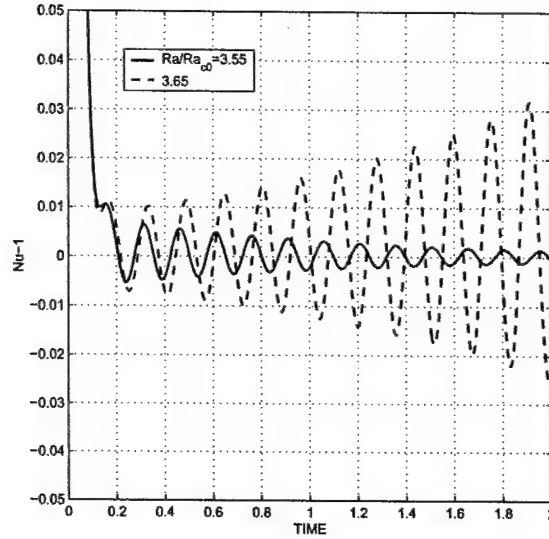


FIGURE 2. Nusselt number of Oscillatory Convection

theory at  $Pr = 7$  predicts that an oscillatory instability is more preferred than the steady state rolls. The closed-loop threshold of stability is  $\alpha_c = 3.73$  and  $Ra = 3.63Ra_{c0}$ , with the frequency of oscillation equal to 20.4. For the same values of  $Ra$  and wavenumber we use the steady state 2D rolls as the initial conditions for our time-domain simulation. Our results appear to be consistent with the prediction of linear theory. Figure 2 shows the behavior of  $Nu$  of the closed-loop solutions at  $K_p = 6$  for two values of  $Ra/Ra_{c0}$ : at 3.55 (solid) and 3.65 (dashed). In both curves, the open-loop steady, 2D rolls are used as the initial condition. These rolls are obtained at  $Ra/Ra_{c0} = 3.65$  and  $\alpha_x = 3.73$  which yield  $Nu = 2.273$ . In Fig. 2 the solid curve shows stable behavior whereas the dashed curve is unstable. The neutral curve has  $Ra/Ra_{c0}$  approximately equal to 3.60. This value is in close agreement with the result of linear theory. Furthermore, the oscillatory behavior in the curves indicate a frequency of about 40.3, again consistent with eigenvalue prediction of  $2 \times 20.4$  of the linear theory. It is noted that  $Nu$  has a harmonic frequency equal to 2 times the fundamental frequency.

The oscillatory convection appears to have a 2D roll planform. The more interesting finding according to the numerical simulations is that this oscillatory solution is not unique for the given set of external parameters. It turns out when we prescribe an additional small perturbation field in the  $y$ -dependence, for the same values of  $K_p$ ,  $Ra$  and  $\alpha_x$ , the closed-form solution will not settle at the 2D oscillatory branch if the cross-roll perturbation is not small. For sufficiently large cross-roll perturbations, the solution will settle down at a subcritical branch. In this case the horizontal planform solution is three-dimensional, which resembles the  $g$ -type hexagons (Or & Kelly, 2001). Depending on the asymmetry in the perturbation temperature, hexagon cells with sinking motion near the center of the cell and rising motion near the cell wall is referred to as the  $g$ -type. For the  $\ell$ -type hexagons the opposite is true. In Fig. 3, we show (a) the planform corresponding to temperature at the lower wall ( $z = 0$ ) and (b) the planform corresponding to horizontal velocity components at horizontal plane  $z = 0.1$  (the velocity components vanish at the lower wall due to a non-slip boundary condition). The 3D hexagonal convection is a steady state pattern and corresponds to  $Nu = 1.4352$ . The hexagonal solution induced by the controller action has been studied in considerable detail (see Shortis & Hall 1996, Or & Kelly 2001) based on weakly nonlinear analysis. Here, we actually obtain the solution from a direct numerical simulation. We summarize several important conclusions based on the results presented: (i) The solutions obtained from our fully nonlinear, 3D pseudospectral plant model have been checked and agree reasonably well against known published results from other independent methods. (ii) The proportional feedback controller induces a subcritical range of  $g$ -type hexagonal convection, which appears to be captured in the nonlinear simulations. Near the stability threshold of the closed-loop system with sufficiently large gain, both 2D oscillatory convection and 3D steady-state hexagonal convection can co-exist in the same parameter region. Next, we consider the

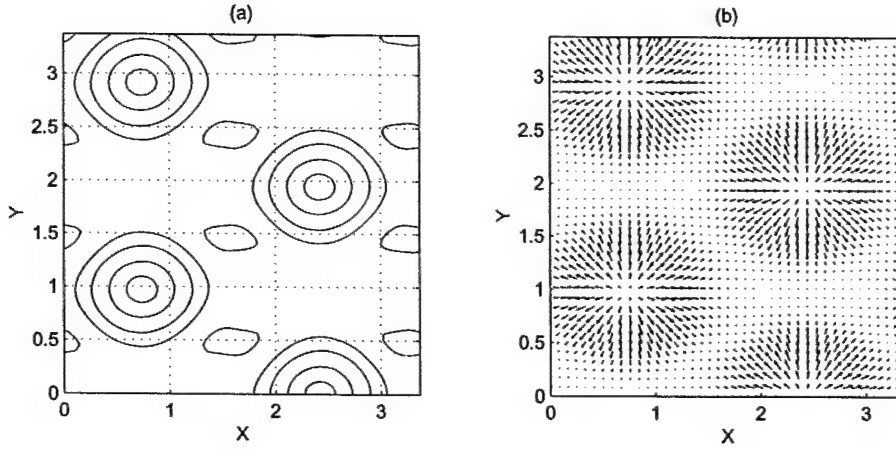


FIGURE 3. Closed-Loop Solution: g-Type Hexagon Pattern

closed-loop simulation using the LQG controller.

### (c) Closed-loop simulations using the LQG controller

We investigate the closed-loop system with an operating condition of the plant model at  $Pr = 7.0$  and  $Ra = 10^4$ . In the setup, the controller gains  $K_f$  and  $K_c$  are steady-states precomputed and stored. The actual controller and the nonlinear plant models are implemented in *FORTRAN* and *MATLAB*. This controller is implemented according to the description of subsection 2(c).

In Fig. 4 we provide a sketch of the stability diagram of the uncontrolled dynamics at  $Pr = 7$  (see Busse & Clever 1979, Fig. 1 for the original plot). The stability boundary of the purely conduction (static) state is the lowest parabolic-shape curves. At each  $Ra$  above the minimum of this neutral curve (supercritical) the linear theory predicts an outer band of wavenumbers in which the basic state is unstable. However, at each supercritical  $Ra$  the stable finite-amplitude convection occurs in a narrower band of wavenumbers.

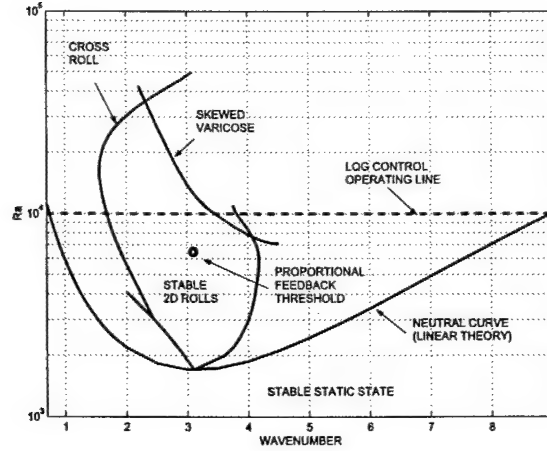


FIGURE 4. A Sketch of the Stability Boundaries for the Uncontrolled Layer at  $Pr = 7.0$

At  $Pr = 7$  the stable finite-amplitude convection in the inner band corresponds to steady 2D convection rolls. For  $Ra = 10^4$  (the dashed line in Fig. 4), the inner band of wavenumbers is bounded on the lower side by the cross-roll instability at  $\alpha \approx 1.75$  and on the higher side by the skew-varicose instability at  $\alpha \approx 3.5$ . At this  $Ra$  the inner band of wavenumbers is significantly smaller than the outer band obtained from the linear theory, which gives approximately 0.74 and 9.0, respectively. The stability boundaries are in general  $Pr$  dependent.

The stable 2D convection rolls are characterized by a single wavenumber but it can be any value within the inner band. Laboratory experiments (see Cross & Hohenberg 1993) using different initial conditions had demonstrated that the stable pattern can have non-unique wavenumber. On the other hand, certain experiments performed by letting  $Ra$  vary either as a slow function of time or by inducing a spatial ramp in the layer thickness indicate that the rolls are realized with a unique wavenumber. Since our goal here is to eliminate the convection pattern, the detailed properties of the nonlinear solution do not concern us other than as the initial condition for our closed-loop solutions.

The closed-loop simulation is demanding computationally in the sense that the entire outer band of wavenumber should be covered in the stabilization of the basic state. In our simulation, the fundamental wavenumbers  $\alpha_x$  and  $\alpha_y$  are selected so that the expansion covers the entire inner band but short of the outer band. We argue that this arrangement is reasonable and we use the truncation numbers  $K = M = N = 32$ . The nonlinearity has the role of limiting the wavenumber of the convection pattern to the inner band. As the initial condition for the closed-loop simulation, we let  $\alpha_x = 1.0$  in the open-loop run with appropriate initial condition. We obtain a steady, two-dimensional roll pattern with a wavenumber of 3.0. In the closed-loop simulation, we add in a small perturbation of cross-rolls superimposed on the steady finite amplitude rolls. The added perturbation assures that the initial condition used is three-dimensional.

The closed-loop simulation results are shown in Figs. 5(a)-(g). Since the transition is two-dimensional, it suffices to reveal the flow fields by showing the cross-sectional view in the  $z - x$  plane. In Figs. 5(a)-(c), we show the transient pattern of the perturbation isotherms in the  $x - z$  plane (with basic temperature subtracted). The three isotherm patterns (a)-(c) of the disturbance field are snapshots obtained at  $t = 0, 0.05$ , and  $0.2$  diffusive time units, respectively. Note that the upper and lower wall both are the perturbation isotherm of zero temperature. The solid (dashed) lines indicate positive (negative) increments of temperature. The same increment of temperature applies to all three panels. The upper panel (a) shows the cross section of the steady-state convection rolls used as the initial condition at  $t = 0$ . Shortly after the controller is turned on at  $t = 0$ , the middle panel (b) shows a steep thermal boundary-layer pattern develops near the lower wall at  $t = 0.05$ . This boundary temperature perturbation possesses an opposite sign to the perturbation in the bulk of the layer of fluid, and therefore exerts a cancelation effect, which tends to drive the fluid towards an isothermal state. The

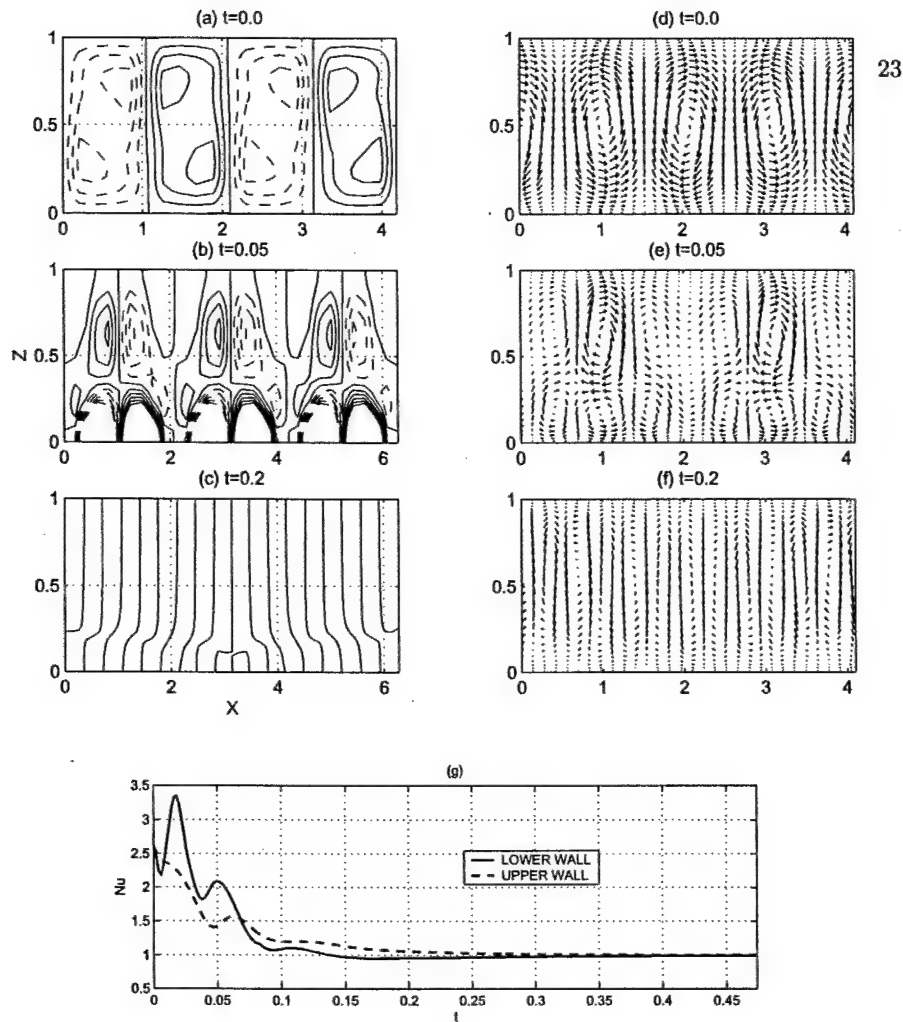


FIGURE 5. (a)-(c) Transient patterns of isotherm under controller action; (d)-(f) corresponding velocity quivers of the flow patterns; (g) Time response of Nusselt numbers at the lower and upper wall ( $Ra = 10^4$  and  $Pr = 7.0$ )

lower panel (c) shows at a later instant (at  $t = 0.2$ ) that the isotherm pattern indeed settles towards a static state. Here the isotherms correspond to a residual temperature distribution of about 1.5% of the temperature shown in the upper panel. The residual temperature continues to approach zero asymptotically in time.

In the right column of panels, Figs. 5(d)-(f) we show the quiver plots of the velocity field corresponding to the left column of panels of isotherms. The arrow sizes in Figs.

5(e)-(f) are according to the true relative scale. For illustration of the flow field we deliberately magnify the arrows in Fig. 5(f). Note that the velocity rolls are shifted by a phase of  $\pi/2$  relative to the isotherm rolls. The upward (downward) motion of fluid is associated with the positive (negative) isotherms, as indicated in the figures. From the middle panel 5(e), we observe that the upwelling and downwelling regions are significantly perturbed by the control action. As a result a secondary row of vortices near the lower wall is apparent. In the lower panel, the convective motion becomes so weak that the vortex structure is no longer visible. Finally, we show the two Nusselt numbers in Fig. 5(g) in time as the indicator for convective heat transport. The lower (solid) and upper (dashed) curves are based on the horizontal-mean temperature gradient at the lower and upper walls, respectively. The gradient is computed normal to the walls. As the thermal actuator action is switched on, a large transient perturbation develops near the lower wall, indicating an increase in local heat flux from the actuator action. The lower Nusselt number shoots up considerably higher than the upper Nusselt number initially for a brief duration. Subsequently to this the upper Nusselt number is greater than the lower value, as the heat in the bulk of fluid is transferred away. Between  $t = 0$  and  $t = 0.474$ , we determined through integration that the area under the curves are 0.5635 (solid line) and 0.5628 (dashed line). The two integral values will converge to the same value in time, as a constraint of the conservation of heat.

For a related drag reduction control problem, Cortelezzi and Speyer (1998) developed a robust reduced-order controller. It is beyond the present scope to consider a reduced-order controller for this nonlinear simulation. Here, on the other hand we determine the spatial roll-off characteristic of the controller based on the Green's function approach. The roll-off characteristics will shed light on the spatial resolution of the arrays of discrete sensors and actuators required for a successful control. A good spatial roll-off implies that



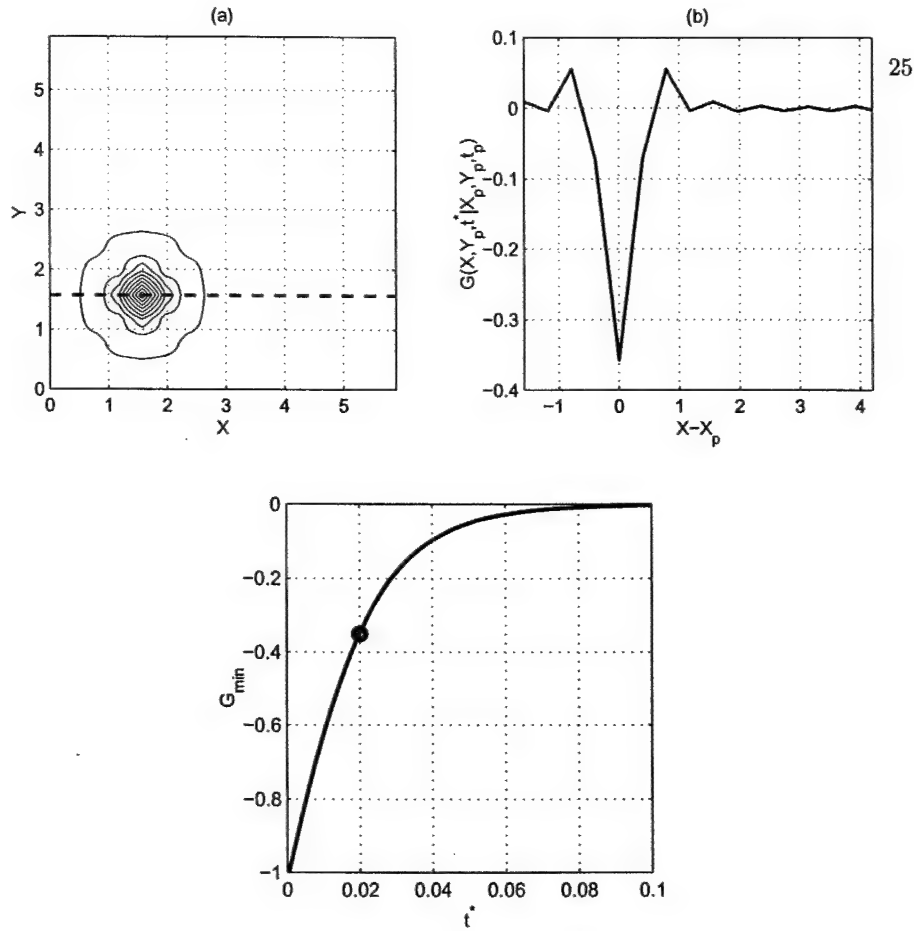


FIGURE 6. (a) isotherms of the response of temperature on the actuator plane due to an impulse source temperature on the sensor plane; (b) variation of the response temperature along the dashed line of Fig. 6(a); (c) change of  $G_{min}$  with  $t^*$

a relatively few measured points are needed to achieve an effective control (see Bamieh & Dahleh 2001). We refer to the description in section 2(d). Consider the same case in the numerical simulation for  $Pr = 7$  and  $Ra = 10^4$  and a length scale of the layer corresponding to  $\alpha_x = 1$  and  $\alpha_y = 1$ . Figure 6(a) shows the contour of the Green's function  $G(x, y, t | x_p, y_p, t_p)$ , which is the response temperature on the actuator plane  $z = 0$  due to an impulse temperature  $\delta(x - x_p)\delta(y - y_p)\delta(t - t_p)$  on the sensor plane  $z_s = 0.3$ . Here we let  $x_p = 1.5$ ,  $y_p = 1.5$  and  $t_p = 0$ ,  $t^* = 20\Delta t$  with  $\Delta t = 10^{-3}$ . Figure 6(b) shows the response temperature profile as a function of  $x - x_p$  along the dashed line

designated in Fig. 6(a). The response temperature corresponds to  $G(x, y_p, t^* | x_p, y_p, t_p)$  (with  $t^* > t_p$ ). The result shows that the function has a negative minimum, here denoted by  $G_{min}$ . The minimum is collocated horizontally with the sensor impulse. The negative temperature generated is intended to cancel the disturbance temperature created by the impulsive temperature. Of particular significance is to notice how steep the response curve (in V-shaped) is, implying that the influence zone about the sensor point is small. From Fig. 6(b), the base width of the V-shape curve is about the width of one roll, assuming that the length scale of the roll does not differ significantly from its critical value. In order for the controller to stabilize the convective disturbance, the spacing between successive points in the array cannot be greater than the effective width of the response temperature.

The plots in Fig. 6(a)-(b) represent a snapshot at  $t = t^*$ . We observed that as  $t^*$  increases from 0, the shape and width of the temperature profile (see Fig. 6(b)) have change little, but the magnitude of the minimum decreases rapidly. In Fig. 6(c), we show the change of the temperature at the minimum,  $G_{min}$ , with  $t^*$ . The large dot in Fig. 6(c) denotes the point corresponding to the snapshot of Figs. 6(a)-(b). Since the system is diffusive, the response temperature decays monotonically in time, as expected.

#### 4. Experimental Considerations

For implementation of the LQG feedback control design an experiment of RBC is considered. This effort will be guided by the result of the nonlinear simulation, modified for air at room temperature (with  $Pr \approx 0.7$ ) as the working fluid. Although the closed-loop numerical results presented earlier in the paper is for the case  $Pr = 7.0$  only, our supplementary analysis completed only recently at  $Pr = 0.71$  has revealed that there is

no significant difference in the closed-loop response between the 2 Prandtl numbers for the condition  $Ra = 10^4$ .

For RBC, previous experiments demonstrate that the initial and onset conditions, as well as the realized convection pattern are well predictable under controlled experimental conditions (Cross and Hohenberg, 1993). Complex situations in applications such as variations of material properties, occurrence of concentration gradient and solutal convection, presence of horizontal basic temperature gradient, side-wall effects, defects in pattern, etc., are not included.

In the experimental apparatus the upper and lower walls will be two types of material with a large range of heat conductivity. The two walls have large aspect ratio to the layer depth, and may have different thermal boundary conditions. Miniature strain gage type heaters will be strategically placed at the lower wall as actuator (with separation between heaters determined by the wavelength of the pattern to be controlled). For air, it is convenient to use the holographic interferometry as the sensing technique. Such a sensor can detect temperature differential to high precision. Our LQG controller design has been validated using simulated sensor data. Eventually, for implementation in the experiment, a reduced-order LQG controller will be developed. The 3D pseudospectral model will be modified to accommodate the spatial and temporal dynamics of the sensors and actuators, guided by laboratory observations and the experimental data.

## 5. Conclusion

The goal achieved in this study is a successful demonstration through numerical simulations that a fully nonlinear, steady and preferred state of convection in a horizontal layer of fluid can be reverted to the no-motion state by closed-loop controller action. The simulated results here show the performance of the LQG controller at  $Ra = 10^4$  and

$Pr = 7$ . At this  $Ra$  the proportional feedback controller is ineffective as according to the linear theory. For even higher values of  $Ra$ , stabilization is likely to be achievable with the LQG controller by using higher spatial resolution in the simulation, but we have not pushed for that result. The reason is that for realistic modeling at high  $Ra$  the effects of the discrete actuator and actuator delay are important considerations as well. Although a general stability proof cannot be inferred from the nonlinear simulation of a few initial conditions, the results do indicate that the linear controller appears quite response in suppressing important finite disturbances.

The numerical method used here to develop the nonlinear plant model is pseudospectral spatially. The integration of the model dynamics equation is performed by a time-splitting technique. We have adopted the conventional scheme developed in Marcus (1984) (also see Canuto et al. 1986). However, since some significant modification of the scheme has been made, we validate our fully nonlinear, three-dimensional plant model by performing a number of check cases to compare against published results, in particular, from Clever & Busse (1974) and Busse & Clever (1979). The agreement appears reasonably good. Moreover, the direct simulation verifies the results of the weakly nonlinear analysis (Or & Kelly 2001) about the presence of the controlled-induced subcritical  $g$ -hexagon solution.

We have also examined the shape function of the actuator response by computing the Green's function of the LQG controller. The shape of the actuation temperature determines the order of the horizontal distance between points of the sensor/actuator arrays in term of the layer gap thickness  $d$ . This information is of critical importance when the more realistic pointwise sensor and actuator are used instead of the continuous ones.

#### Acknowledgement

This research is supported by the United States Air Force (Grant no. F49620-00-1-0166).

#### REFERENCES

- BAMIEH, B. & DAHLEH, M. 2001 Energy amplification in channel flows with stochastic excitation. *Phy. Fluids*, **13**
- BODENSCHATZ, E., PESCH, W. & AHLERS, G. 2000 New developments in Rayleigh-Bénard Convection, *Ann. Rev. Fluid Mech.*, 709-778.
- BUSSE, F.H. & CLEVER, R.M. 1979 Instabilities of convection rolls in a fluid of moderate Prandtl number. *J. Fluid Mech.*, **91**, 319-335.
- CANUTO, C. HUSSAINI, N.Y., QUARTERONI, A. & ZANG, T.A. 1986 *Spectral Methods in Fluid Dynamics*, Springer-Verlag.
- CLEVER, R.M. & BUSSE, F.H. 1974 Transition to time-dependent convection. *J. Fluid Mech.*, **65**, 625-645.
- CORTELEZZI, L. & SPEYER, J.L. 1998 Robust reduced-order controller of laminar boundary layer transition. *Phys. Rev. E* **58**, 1906-1910.
- CROSS, M.C. & HOHENBERG, P.C. 1993 Pattern formation outside of equilibrium. *Rev. modern phy*, **65**, No. 3, part II.
- GOTTLIEB, D. & ORSZAG, S.A. 1977 *Numerical Analysis of Spectral Methods: Theory and Applications*, SIAM-CBMS, Philadelphia.
- HOWLE, L.E. 1996 A comparison of the reduced Galerkin and pseudospectral methods for simulation of steady Rayleigh-Benard convection, *Int. J. Heat Mass Transfer*, **39**, 2401-2407.
- HOWLE, L.E. 1997a Linear stability analysis of controlled Rayleigh-Bénard convection using shadowgraphic measurement. *Phys. Fluids*, **9**, 3111-3113.
- HOWLE, L.E. 1997b Control of Rayleigh-Bénard convection in a small aspect ratio container. *Int. J. Heat Mass Transfer*, **40**, 817-822.
- HOWLE, L.E. 1997c Active control of Rayleigh-Bénard convection. *Phy. Fluids*, **9**, 1861-1863.

- HOWLE, L.E. 2000 The effect of boundary properties on controlled Rayleigh-Bénard convection. *J. Fluid Mech.*, **411**, 39–58.
- MARCUS, P.S. 1984 Simulation of Taylor-Couette flow. Part I: Numerical methods and comparison with experiment. *J. Fluid Mech.*, **146**, 45–64.
- OR, A.C. & KELLY, R.E. 2001 Feedback control of weakly nonlinear Rayleigh-Bénard-Marangoni convection. *J. Fluid Mech.*, **440**, 27–47.
- OR, A.C., CORTELEZZI, L. & SPEYER, J.L. 2001 Robust feedback control of Rayleigh-Bénard convection. *J. Fluid Mech.*, **437**, 175–202.
- PRESS, W.H., TEUKOLSKY, S.A., VETTERLING, W.T. & FLANNERY, B.P. 1992 *Numerical Recipes The Art of Scientific Computing*, 2nd Ed.
- RHEE, I. & SPEYER, J.L. 1991 A game theoretic approach to a finite-time disturbance attenuation problem. *IEEE Trans. Automat. Contr.*, **36**, 1021–1032.
- SHORTIS, T.A. & HALL, P. 1996 On the effect of feedback control on Bénard convection in a Boussinesq fluid. *NASA Contractor Rep.* 198280: ICASE Rep. 96-9.
- TANG, J. & BAU, H.H. 1993 Stabilization of the no-motion state in Rayleigh-Bénard convection through the use of feedback control. *Phys. Rev. Letters*, **70**, 1795–1798.
- TANG, J. & BAU, H.H. 1994 Stabilization of the no-motion state in the Rayleigh-Bénard problem. *Proc. R. Soc. Lond. A*, **447**, 587–607.
- TANG, J. & BAU, H.H. 1998a Experiments on the stabilization of the no-motion state of a fluid layer heated from below and cooled from above. *J. Fluid Mech.*, **363**, 153–171.
- TANG, J. & BAU, H.H. 1998b Numerical investigation of the stabilization of the no-motion state of a fluid layer heated from below and cooled from above. *Phys. Fluids*, **10**, 1597–1610.

APPENDIX E:  
Control of Turbulent Boundary Layers  
*to appear in Physics of Fluids, May 2003*



# Control of Turbulent Boundary Layers\*

John Kim

Department of Mechanical and Aerospace Engineering  
University of California, Los Angeles, CA 90095-1597

The objective of this paper is to give an overview of recent progress on boundary layer control made by the author's research group at UCLA. A primary theme is to highlight the importance of a certain linear mechanism and its contribution to skin-friction drag in turbulent boundary layers – and the implication that significant drag reduction can be achieved by altering this linear mechanism. Examples that first led to this realization are presented, followed by applications of linear optimal control theory to boundary-layer control. Results from these applications, in which the linear mechanism in turbulent channel flow was targeted, indirectly confirm the importance of linear mechanisms in turbulent – and hence, nonlinear – flows. Although this new approach has thus far been based solely on numerical experiments and are yet to be verified in the laboratory, they show great promise and represent a fundamentally new approach for flow control. The success and limitations of various controllers and their implications are also discussed.

---

\*This paper is a written version of the author's 2001 Otto Laporte Award Lecture presented at the 54th Annual APS/DFD Meeting in San Diego, CA, November 16-18, 2001

# 1 INTRODUCTION

Control of turbulent flows, turbulent boundary layers in particular, has been a subject of much interest owing to the high potential benefits. Skin-friction drag, for example, constitutes a large fraction of the total drag on commercial aircrafts and cargo ships, and any reduction entails substantial savings of the operational cost for commercial airlines and cargo-shipping industries.<sup>1</sup> Enhanced mixing in combustion engines, enhanced heat transfer in heat exchangers, or reduced heat transfer to gas-turbine blades are only a few examples that also illustrate the immediate benefits of turbulence control. Successful control, however, requires both a thorough understanding of the underlying physics of turbulent flow and an efficient control algorithm, the current state of which leaves much room for improvement.

Significant progress has been made recently by combining computational fluid dynamics, control theories, and sensor/actuator technologies. Direct numerical simulation (DNS) and large-eddy simulation (LES), despite being limited to relatively simple and moderate Reynolds-number flows, have provided much needed detailed information, from which insight into turbulent flow physics can be gained. Our understanding of the physics of turbulent boundary layers and free-shear flows has been significantly improved in large part due to DNS and LES of these flows over the past two decades.<sup>2</sup>

Most early attempts of turbulence control were based on the investigator's intuition and/or on a trial-and-error basis. Several investigators have recently started applying more systematic approaches to controller design. These approaches are significantly different from previous ones in that modern control theories are incorporated into the controller design. Some of these new approaches and their relationships to each other will be discussed below.

Properly designed controllers require appropriate sensors and actuators. This has been a critical issue for turbulence control, boundary-layer control in particular, because the time and length scales associated with the turbulent eddies to be controlled are extremely small at the Reynolds numbers of engineering applications, thus requiring a large number of small sensors and actuators with high-frequency response. Micro-electro-mechanical systems (MEMS) technology will play an essential role in producing arrays of a large number of sensors and actuators at a reasonable cost. The possibility of utilizing MEMS technology in producing such sensors and actuators has been demonstrated recently by the UCLA-Caltech group. They were able to fabricate sensors, actuators,

and simple control logic onto a chip, thus illustrating, at least in principle, that MEMS technology can produce the large number of sensors and actuators necessary for turbulence control. Interested readers are referred to Tsao *et al.*<sup>3</sup> and Ho and Tai<sup>4</sup>, for applications of MEMS technology to boundary layer control and general fluid dynamics, respectively.

The objective of this paper is to provide an overview of recent progress made by the author's research group at UCLA. Particular emphasis is upon nontraditional approaches using modern control theory (see, for example, Zhou *et al.*<sup>5</sup>). Other research groups (UCSD, UCSB, Stanford in the US, and KTH in Sweden, to name a few) are conducting similar research, but they are not discussed here as they were outside the scope of the lecture upon which this paper is based. I mention in passing that the work carried out by researchers at UCSD, UCSB and KTH is very closely related to that described in Section 4.4, while that by the Stanford group is similar to those described in Section 4.1 and 4.3.

This paper is organized as follows. A brief account of the history of an early numerical simulation of turbulent channel flow, which is viewed by many as a starting point for establishing numerical simulation of turbulent flows as a viable tool for turbulence research, is given in Section 2. In Section 3 a brief discussion of the skin-friction drag in turbulent boundary layers is given. Various approaches aimed at reducing the skin-friction drag, especially from the perspective of controlling a key linear mechanism, are presented in Section 4. Issues and limitations associated with turbulence control, and a concluding remark, are given in Section 5.

In this paper, I shall use  $(x, y, z)$  for the streamwise, wall-normal, and spanwise directions, respectively, and  $(u, v, w)$  for the corresponding velocity components unless stated otherwise. The superscript  $+$  denotes flow quantities non-dimensionalized by the wall-shear velocity,  $u_\tau$ , and the kinematic viscosity,  $\nu$ .

## 2 ILLIAC IV AND TURBULENT CHANNEL SIMULATIONS

The direct numerical simulation of turbulent channel flow presented in this paper as examples of various control experiments has its origin in the late 1970s, when I began working at NASA Ames Research Center. The original computations<sup>6</sup> were carried out on a very unique computer called ILLIAC IV, which had just been brought into NASA Ames Research Center from the University of

Illinois.<sup>7</sup> The ILLIAC IV was, to the best of my knowledge, the first large-scale parallel computer with 64 processors (called processing elements or PEs). Although it was huge and required an entire building to house it, the computer had very limited power by present-day standards. For example, it had the total of only one megabyte of memory (each PE had 2,048 64-bit words of memory). Asynchronous data transfer between the core memory and external memory, which consisted of 13 4-foot diameter disks, each with 9.8 megabytes of memory (128 megabytes in total), was designed and used for 'large-scale' computations. Homemade compilers were written by Ames scientists Bob Rogallo (CFD) and Alan Wray (Vectoral) to replace the compiler supplied with the machine, since it was so unreliable. The ILLIAC IV typically ran with the clock at 12.5 MHz, and an optimized code like our plane-channel solver could achieve about 20 Mflops in 64-bit mode and 30 Mflops in 32-bit mode.<sup>8</sup>

With this then-powerful and unique computer, we performed the large-eddy simulation (LES) of turbulent channel flow.<sup>6</sup> At first, it was not very well received, especially by experimentalists, despite the fact that computed turbulence statistics were in good agreement with measured ones. In order to convince the skeptics, and perhaps to some extent ourselves, we produced computer-generated motion-picture visualizations from the simulated flow field, which closely mimicked laboratory visualizations using hydrogen-bubble wires in water<sup>9</sup> (see Fig. 1). This visualization, now common in computational fluid dynamics, was unusual at the time, and was instrumental in convincing many experimentalists who had previously been skeptical of the validity of numerical simulations. This computer-generated movie thus helped establish large-scale computations as an equal partner with laboratory experiments as a turbulence research tool.

### 3 SKIN-FRICTION DRAG IN TURBULENT BOUNDARY LAYERS

Although it has been common knowledge in fluid mechanics that the skin-friction drag in turbulent boundary layers is much higher than that in laminar boundary layers, it was not until recently that we began to understand why this was the case. Since the underlying physics of high skin-friction drag were not known, most attempts to reduce the drag were on a trial-and-error basis.

Existence of well-organized turbulence structures and the recognition that these structures play important roles in the wall-layer dynamics are among the major advances in turbulent boundary

layer research during the past several decades. The ubiquitous structural features in this region are low- and high-speed “streaks,” which consist mostly of a spanwise modulation of the streamwise velocity. These streaks are created by streamwise vortices, which are roughly aligned in the streamwise direction. It has now been recognized, in large part due to numerical investigations, that streamwise vortices are also responsible for the high skin-friction drag.<sup>10,11</sup> These vortices are primarily found in the buffer layer ( $y^+ = 10 - 50$ ) with their typical diameter in the order of  $d^+ = 20 - 50$ .<sup>12</sup> There is strong evidence that most high skin-friction regions in turbulent boundary layers are induced by nearby streamwise vortices (Fig. 2). These vortices are formed and maintained autonomously (independent of the outer layer) by a self-sustaining process, which involves the wall-layer streaks and an instability associated with them.<sup>13–16</sup>

In light of this description, we asked the following question for the purpose of boundary-control for drag reduction:

Can we suppress (or mitigate) the formation of these streamwise vortices through an actuation at the wall, and if so, would it lead to a significant reduction of the skin-friction drag?

The remainder of this paper addresses this question by reviewing various approaches that have been used in an attempt, directly or indirectly, to reduce the impact of streamwise vortices on the skin-friction drag in turbulent boundary layers. In particular, we examine a linear mechanism associated with these streamwise vortices, and present controllers designed to suppress the linear mechanism. The success of these controllers demonstrates that this linear mechanism plays an important role, although the boundary layer on the whole is governed by nonlinear dynamics.

This paper discusses active feedback control, which involves actuation and sensing, nominally at the wall. We mention here in passing that passive control, which requires no actuation (i.e., no external energy input), has also been tried. One successful example, which has been shown to reduce the skin-friction drag (a maximum on the order of 5-7%), involves riblets. These are surfaces with narrow grooves aligned in the streamwise direction. It is noteworthy that the riblet surface also reduces the skin-friction drag by interfering with the interactions between the streamwise vortices and the wall.<sup>10</sup> The interested reader is referred to Choi *et al.* and the references therein.

## 4 NUMERICAL EXPERIMENTS

All examples presented in this paper, unless stated otherwise, have been obtained in a turbulent channel with unsteady blowing and suction at the wall as control input, which was determined by various feedback control laws. Details of the numerical methods<sup>17</sup> can be found in Kim *et al.*<sup>12</sup> All numerical experiments have been performed at very low Reynolds numbers,  $Re_\tau = 100 - 200$ , where  $Re_\tau$  denotes the Reynolds number based on the wall-shear velocity and channel half-width. Implications related to the low Reynolds number flows are addressed in Section 5.

### 4.1 Opposition Control

In an attempt to mitigate the effect of streamwise vortices in the buffer layer, Choi *et al.*<sup>18</sup> used blowing and suction at the wall equal and opposite to the wall-normal component of velocity at  $y^+ = 10$  (Fig. 3). They showed that this simple control, now known as *opposition control*,<sup>19</sup> resulted in approximately 25-30% drag reduction in a turbulent channel flow. The computed flow fields were examined to determine the mechanism by which the drag reduction was achieved. The most salient feature of the controlled flow field was that the strength of the near-wall streamwise vortices was substantially reduced, and consequently most of the high skin-friction regions were suppressed, resulting in the mean drag reduction.

Although the method employed in opposition control is impractical, as the information at  $y^+ = 10$  is normally not available, it conveys a significant message for our purpose: it demonstrates that manipulation of the near-wall streamwise vortices does indeed lead to substantial reduction of the skin-friction drag in turbulent boundary layers. Opposition control has been used as a reference case to which other control schemes can be compared.

### 4.2 Adaptive Inverse Model

In order to circumvent the problem associated with opposition control, Lee *et al.*<sup>20</sup> used wall actuation, which depends only on flow quantities that can be measured at the wall. They designed and trained a neural network, which served as an adaptive inverse model of the plant represented by the Navier-Stokes equations (Fig. 4). The network was trained to predict actuation at the wall (control input) for given outputs at the wall. Once properly trained, this inverse model network was used as a controller to predict an optimal control input for a desired output, i.e., reduced skin-

friction drag. A schematic illustrating a neural network representing an adaptive inverse model of the Navier-Stokes equations is shown in Fig. 4.

Details of their neural network are given in Lee *et al.*<sup>20</sup> The functional form of the final neural network is:

$$v_{jk} = W_a \tanh \left( \sum_{i=-(N-1)/2}^{(N-1)/2} W_i \frac{\partial w}{\partial y} \Big|_{j,k+i} - W_b \right) - W_c, \quad (1)$$

$$1 \leq j \leq N_x \text{ and } 1 \leq k \leq N_z,$$

where  $W$  denotes weight,  $N$  is the total number of input weights, and the subscripts  $j$  and  $k$  denote the numerical grid point at the wall in, respectively, the streamwise and spanwise directions.  $N_x$  and  $N_z$  are the number of computational grid points in each direction. The summation is done over the spanwise direction. Seven neighboring points ( $N = 7$ ), including the point of interest, in the spanwise direction (corresponding to approximately 90 wall units) were found to provide enough information to adequately train and control the near-wall structures responsible for the high skin friction. Note that the input to the neural network is  $\partial w / \partial y$  at the wall, not  $\partial u / \partial y$ . Initially  $\partial u / \partial y$  and  $\partial w / \partial y$  at the wall at several instances of time were used as input data fields, and the actuation at the wall was used for the output data of the network. Experimentally we found that only  $\partial w / \partial y$  at the wall from the current time was necessary for successful network performance.

Applying this control scheme to a turbulent channel flow at low Reynolds numbers resulted in about 20% drag reduction. The computed flow fields were examined and it was found that instantaneous flow patterns were very similar to those observed in the opposition-controlled channel, i.e., the strength of the near-wall streamwise vortices was substantially reduced (Figs. 5-6). This result further substantiates the notion that successful suppression of streamwise vortices leads to a significant reduction in the skin-friction drag. It is worth mentioning here, however, that there may be other flow quantities that have a more direct link to the reduced skin-friction drag, but these we have not yet explored.

An examination of the weight distribution from the on-line neural network led to a very simple control scheme that worked equally well while being computationally more efficient. This simple control scheme indicated that the optimum blowing and suction at the wall should be in the form,

$$v_w \sim \frac{\partial}{\partial z} \frac{\partial w}{\partial y} \Big|_w, \quad (2)$$



where the overbar represents a local spatial average with high wavenumber components properly reduced (see Lee *et al.*<sup>20</sup> for details). The converged weight distribution can be expressed analytically, thus making the implementation of this control scheme relatively easy.

The simple pattern of the weight distribution derived from the nonlinear network suggests the possibility of using a linear network. A linear neural network, identical to that of Eqn. (1) without the hyperbolic tangent function, was applied to the same problem. This linear network resulted in almost identical drag reduction with instantaneous flow patterns very similar to those obtained by the original nonlinear network. The success of this linear network suggests that the flow dynamics of interest, i.e., those relevant to high-skin friction, can be approximated by a linear model, the implication of which will be further explored in the remainder of this paper.

### 4.3 Adjoint-Based Sup-Optimal Control

As mentioned in the introduction, most previous control work has been rather ad-hoc, in that it was primarily based on the investigator's intuition and insight into the flow physics under consideration. The *opposition control* is a good example. More systematic approaches, relying on the equations that govern the problem under control, have appeared recently. One such approach is adjoint-based optimization.<sup>21-24</sup> In this approach the control objective is to minimize a cost functional,  $J(\phi)$ , of control input,  $\phi$ . Once the sensitivity of the cost functional with respect to the control input is known, it can be minimized by using any gradient-based iteration scheme. For example,

$$J(\phi^{k+1}) = J(\phi^k) + \frac{DJ}{D\phi}(\phi^{k+1} - \phi^k), \quad (3)$$

where  $DJ/D\phi$  is the Fréchet differential of  $J$ , representing the sensitivity of the cost functional to the control input. More advanced iterative schemes, such as a conjugate-gradient method, could also be used, instead of the simple gradient method shown here. A key step is how to evaluate the sensitivity functional. A popular approach has been to express it in terms of properly defined adjoint flow variables, which can be obtained by solving adjoint governing equations. In general, one has to solve the Navier-Stokes equations and the adjoint Navier-Stokes equations simultaneously. Interested readers are referred to the references given above for further details.

Bewley *et al.*<sup>24</sup> applied an adjoint-based optimal control, in which a control objective was minimized over a finite time period, to a turbulent channel at  $Re_\tau=100$ . Their approach led to flow laminarization with a drag reduction of over 50%. However, this algorithm requires solving the

Navier-Stokes equations and their adjoint equations iteratively over a finite time period (referred to as finite-time horizon); while the adjoint equations are integrated backward in time, the Navier-Stokes equations are integrated forward in time, during which the control input, which in turn depends on the adjoint variables, is required. This procedure is computationally expensive, and more importantly, impossible to implement in practice. Nevertheless, this is an important accomplishment on several accounts. For example, it demonstrates that a control algorithm derived rigorously from a control theory independent of flow physics can outperform intuition-based controls. Also, notwithstanding its practical limitation, it establishes the best possible control process, from which physical insight may be gained by examining the manner in which the laminarization occurred. The adjoint-based approach may also be useful for off-line optimization applications, where the iterative optimization is done off-line once and the result is applied in an open-loop control.

Lee *et al.*<sup>22</sup> took a slightly different approach. Instead of searching for the optimal state over a finite time period, which requires solving the Navier-Stokes and their adjoint equations iteratively, they looked for a *suboptimal* state, in which a control objective is minimized in the limit of the time horizon approaching zero. This adjoint-based *suboptimal control* does not require solving the governing equations iteratively. Furthermore, they showed that a wise choice of the control objective, coupled with a particular adjoint formulation (which involved taking an adjoint of only the *linear* part of the discretized Navier-Stokes equations), could lead to a more simple and practical control law. In this approach, the desired control input was expressed in terms of adjoint flow quantities at the wall, which could be evaluated without solving the adjoint equations explicitly. Minimization of a cost functional involving  $\partial w / \partial y$  led to (see Lee *et al.*<sup>22</sup> for the detailed procedure):

$$v_w \sim \left\langle \frac{\partial}{\partial z} \frac{\partial w}{\partial y} \Big|_w \right\rangle, \quad (4)$$

where  $\langle \rangle$  represents a local spatial average. Note that this expression is very similar to Eqn. (2), which was obtained by the adaptive neural network. The only difference in the two expressions is how high wavenumber components are reduced when the spatial average is performed; see Lee *et al.*<sup>22</sup> for details. Application of Eqn. (4) to the turbulent channel resulted in almost identical results to those discussed in Subsection 4.2, in that the computed flow field contained fewer strong near-wall streamwise vortices and skin-friction drag was reduced.

Although the two control schemes discussed in Subsections 4.2 and 4.3 were derived from totally different approaches, they yielded very similar feedback control laws. It is worth mentioning here

that the adaptive nonlinear network could be approximated well by a linear network, and that the final form of the adjoint-based suboptimal control was derived without including the nonlinear part of the discretized Navier-Stokes equations when the adjoint operation was performed. It appears that whatever physics that are relevant to skin-friction drag reduction in turbulent boundary layers can be adequately approximated by a linear model.

## 4.4 Systems Control Theoretic Approaches

Many advances have been made in linear optimal control theory over the past several decades. Unfortunately, applications of this modern control theory to flow-control problems, turbulence control in particular, have been rare. It is in large part due to the common belief that turbulent flows are nonlinear, and hence, there is very little chance that linear control theory is applicable to turbulence control. The other deterring factor might have been the fact that turbulent flows have a large number of degrees of freedom, and require analysis of a very high-dimensional system. It shall be shown here that both concerns can be overcome for control of the skin-friction drag in turbulent boundary layers.

Since the pioneering work by Joshi *et al.*,<sup>25</sup> in which they demonstrated that transition to turbulence (including transition due to finite-amplitude, hence nonlinear, disturbances) can be suppressed by a linear integral feedback controller, there has been a flurry of activity reporting successful applications of linear optimal control to turbulent and transitional flows.<sup>26–31</sup> We briefly review some fundamentals of linear optimal control theory here before we proceed to present our results. The reader is also referred to a recent paper by Bewley,<sup>23</sup> for an excellent introduction to linear optimal control theory as applied to fluid mechanics problems.

### 4.4.1 Linear Optimal Control and State-Space Representation

Linear optimal control theory starts with a state-space representation of the dynamical system to be controlled. A state-space representation of a dynamical system can be written as

$$\frac{dx}{dt} = Ax + Bu, \quad (5)$$

where  $x$  represents the state vector of the system and  $u$  denotes the control input. The system matrix  $A$  contains the system dynamics, and  $B$  denotes an input matrix, which depends on the particular type of actuation. In linear quadratic regulator (LQR) synthesis, a cost function to be

minimized is written in the following quadratic form,

$$J = \lim_{T \rightarrow \infty} \frac{1}{T} \int_0^T (\gamma \mathbf{x}^* Q \mathbf{x} + \mathbf{u}^* R \mathbf{u}) dt, \quad (6)$$

where the superscript  $*$  denotes conjugate transpose and  $\gamma$  is a control parameter. The matrices  $Q$  and  $R$ , respectively, represent a particular form of the control objective and how the cost of control should be accounted for. A large weighting on the cost of control (small  $\gamma$ ) signifies a high cost of control, and vice versa. The optimal control input  $\mathbf{u}$  minimizing the cost function is found in the following form,

$$\mathbf{u} = -K \mathbf{x}, \quad (7)$$

where  $K$  is the control gain matrix, which is to be determined. The optimal  $K$  minimizes the cost function, and is obtained by solving an algebraic Riccati equation involving matrices  $A, B, Q, R$  and the control parameter  $\gamma$ :

$$AP + PA + \gamma Q - PBR^{-1}B^*P = 0, \quad (8)$$

from which  $K = R^{-1}B^*P$  is determined.

Note that in the LQR synthesis, the optimal control input requires complete information of the state vector. In most practical situations, complete system information,  $\mathbf{x}$ , is not known, and it must be estimated based on limited measurements. This leads to linear quadratic Gaussian (LQG) synthesis, and the following dynamical system representation:

$$\frac{d\mathbf{x}}{dt} = A\mathbf{x} + B\mathbf{u} + \Gamma\mathbf{w} \quad (9)$$

$$\mathbf{z} = C\mathbf{x} + D\mathbf{u} + \mathbf{v} \quad (10)$$

$$\frac{d\hat{\mathbf{x}}}{dt} = A\hat{\mathbf{x}} + B\mathbf{u} + L(\mathbf{z} - \hat{\mathbf{z}}) \quad (11)$$

$$\mathbf{u} = -K\hat{\mathbf{x}}, \quad (12)$$

where  $\hat{\mathbf{x}}$  denotes an estimated state vector,  $\mathbf{w}$  and  $\mathbf{v}$ , respectively, represent system and measurement noise, which in LQG synthesis are assumed to be white Gaussian processes,  $\mathbf{z} = C\mathbf{x} + D\mathbf{u} + \mathbf{v}$  denotes the actual observation, and  $\hat{\mathbf{z}} = C\hat{\mathbf{x}} + D\mathbf{u}$  is the observation based on the estimated state. Matrices  $C, D, \Gamma$ , respectively, represent the measurement, feed-through, and input matrices. The Kalman gain matrix  $L$ , which is designed to minimize the error associated with the estimated state, is determined in the same manner as the control gain matrix  $K$ , by solving an algebraic Riccati equation involving matrices  $A, C, \Gamma$ . The ratio of the power spectral densities of the noise mentioned

above enters as a design parameter. In control terminology, Eqn. (11) is referred to as a “system estimator” and Eqn. (12) a “controller,” and together they are referred to as a “compensator.” In general, the system dynamics may contain many unobservable and/or uncontrollable modes, and they are neither desirable nor necessary to include in the estimator. A reduced-order model for the estimator is therefore used. This model reduction step is especially critical for turbulence control, since the original system is a very high-dimensional system, many modes of which are unobservable and uncontrollable as we normally limit our sensing and actuation to the wall. In the study to be described in Section 4.4.5, we used a balanced-realization model-reduction method, in which the original high dimensional system is reduced by considering controllability and observability. The reader is referred to Lee *et al.*<sup>30</sup> for the model-reduction techniques used in the present study.

#### 4.4.2 State-Space Representation of the Navier-Stokes Equations

Representing the wall-normal velocity,  $v$ , and the wall-normal vorticity,  $\omega_y$ , in terms of Fourier modes in the streamwise ( $x$ ) and the spanwise ( $z$ ) directions, the linearized Navier-Stokes (N-S) equations can be written in an operator form

$$\frac{d}{dt} \begin{bmatrix} \hat{v} \\ \hat{\omega}_y \end{bmatrix} = [A] \begin{bmatrix} \hat{v} \\ \hat{\omega}_y \end{bmatrix} \quad (13)$$

where

$$[A] = \begin{bmatrix} L_{os} & 0 \\ L_c & L_{sq} \end{bmatrix} \quad (14)$$

and the  $\hat{(\ )}$  denotes a Fourier-transformed quantity. Here  $L_{os}$ ,  $L_{sq}$  and  $L_c$  represent the Orr-Sommerfeld, Squire, and the coupling operators, respectively, which are defined as

$$L_{os} = \Delta^{-1} \left( -ik_x U \Delta + ik_x \frac{d^2 U}{dy^2} + \frac{1}{Re} \Delta^2 \right) \quad (15)$$

$$L_{sq} = -ik_x U + \frac{1}{Re} \Delta \quad (16)$$

$$L_c = -ik_z \frac{dU}{dy}, \quad (17)$$

where  $k_x$  and  $k_z$  are the streamwise and spanwise wavenumbers, respectively,  $k^2 = k_x^2 + k_z^2$ ,  $\Delta = \partial^2 / \partial y^2 - k^2$ , and  $U$  is the mean velocity about which the Navier-Stokes equations are linearized.

Eqn. (13) is then already in the state-space representation form

$$\frac{dx}{dt} = Ax, \quad (18)$$

where the state vector  $\mathbf{x}$  consists of the wall-normal velocity and wall-normal vorticity expressed in terms of their expansion coefficients. Any polynomial expansion or collocation representation of the state vector can be used for this purpose. Having written the Navier-Stokes equations in this form, we are now in a position to design an optimal controller for this linear system.

#### 4.4.3 Application to a Linear System

Before designing and applying a linear controller to the nonlinear problem of interest, the turbulent channel, we first considered the following linear problem.

The transient growth due to non-normality of the operator associated with linearized Navier-Stokes equations has received much attention during the past several years.<sup>32–37</sup> It has been shown that certain disturbances can grow to  $\mathcal{O}(Re^2)$  in time proportional to  $\mathcal{O}(Re)$ .<sup>35,37</sup> It has been suggested that this transient growth, which is due to a linear mechanism, can lead to a transition to turbulence at a Reynolds number smaller than the critical Reynolds number, below which classical linear stability theory, based on modal analysis, predicts that all small disturbances decay asymptotically. Some investigators have proposed that this linear process is responsible for subcritical transition in some wall-bounded shear flows, such as plane Poiseuille flow and Couette flow. Some investigators further postulated that the same linear process is also responsible for the wall-layer streaky structures observed in turbulent boundary layers.<sup>32,33</sup>

Since this transient growth is due to a linear mechanism, it should be affected by a properly designed linear optimal controller, based on the linear system described in Subsection 4.4.2. The so-called ‘optimal’ disturbance<sup>38</sup> was constructed in a manner similar to that described by Butler and Farrell<sup>32</sup> for  $Re_c = 5,000$ , where  $Re_c$  denotes the Reynolds number based on the centerline velocity and channel half-width. Note that this is a subcritical Reynolds number with no unstable eigenmodes, but this ‘optimal’ disturbance consists of a special combination of decaying eigenmodes. Due to the non-normality of the linearized Navier-Stokes operator, some of these eigenmodes are almost parallel to each other, and the energy associated with this ‘optimal’ disturbance can grow initially before it ultimately decays.

An LQR controller, which minimizes the total disturbance energy, was constructed and applied to the linear system with the ‘optimal’ disturbance as the initial condition. Fig. 7 shows the effect of the LQR controller. Also shown in the figure is a result obtained with opposition control. It should be noted that the LQR controller utilizes complete internal state information, whereas the

opposition control uses the information at a particular wall-normal location only. This explains why the LQR controller performed better than the opposition control.

#### 4.4.4 LQR Control of Turbulent Channel

It was not too surprising to see that a linear optimal controller worked well when applied to a linear problem. A more challenging question is whether a controller based on the linearized system would work at all in turbulent channel flow, which is obviously a nonlinear system. There are several reasons we expected a positive result in spite of the fact that turbulent channel flow is certainly beyond the scope of linear controllers. First, we saw in Subsections 4.2 and 4.3 that the wall-layer dynamics responsible for high skin-friction drag in turbulent boundary layers can be approximated well by a linear model. Second, both the transient growth mechanism in transitional boundary layers and the self-sustaining mechanism of near-wall turbulence structures in turbulent boundary layers are at least in part due to the linear mechanism described in Subsection 4.4.3. Consequently, we should be able to model this linear mechanism in terms of the linear state-space representation, and a controller based on this linear model should be able to affect the linear mechanism.

Several LQR controllers were constructed, to minimize 1) wall-shear stress fluctuations, 2) turbulent kinetic energy, and 3) the linear coupling term (see Subsection 4.5 below). Results are shown in Figs. 8-10. A common feature for all of these drag-reduced flow fields is weakened streamwise vortices (Fig. 9), resulting in reduced high skin-friction extrema at the wall (Fig. 10). In some cases, especially for case 1), the controller met its design objective (i.e., it reduced fluctuating wall-shear stresses) quite dramatically, but it did not lead to similarly dramatic mean drag reduction. A further examination of the computed flow field revealed that, in contrast to opposition control, the control effect is confined to the near-wall.<sup>39</sup> Apparently, we need a cost function, whose minimization affects turbulence structures away from the wall. Nevertheless, all of these *linear* controllers worked remarkably well in the nonlinear flow.

The success of these linear controllers confirms, once again, the notion that a linear mechanism plays an important role in turbulent boundary layers. In a true linear system, the base (i.e., mean) flow about which the system is linearized does not evolve in time, and the system matrix  $A$  is independent of time. In a nonlinear system, however, as the state vector evolves in time, it affects the mean flow and thus  $A$  is not constant in time. One way to account for this nonlinearity is to recompute the system matrix  $A$  as the mean flow evolves. A new gain matrix  $K$  is obtained as



the mean flow evolves. This can be viewed as a type of *gain scheduling*.<sup>23</sup> An example of LQR control with gain scheduling is shown in Fig. 11, which yields complete laminarization at  $Re_\tau=100$ . However, we have observed that this result was very sensitive to the manner by which the gain scheduling was implemented.<sup>39</sup> But this sensitivity notwithstanding, this result illustrates that a further fine tuning of linear controllers can lead to substantial improvements for nonlinear flows.

#### 4.4.5 LQG Control of Turbulent Channel

As mentioned in Subsection 4.4.1, in most practical applications, complete state information is not available and must be estimated from limited measurements. Furthermore, the estimation must be carried out based on a reduced-order model for various reasons. Lee *et al.*<sup>30</sup> constructed a two-dimensional reduced-order model of the linearized Navier-Stokes system, based on controllability and observability considerations. The size of the reduced-order estimator (*i.e.*, the number of independent modes or the length of the state vector representing the reduced-order estimator) was less than 2.5% of the original system. This two-dimensional reduced-order compensator (*i.e.*, estimator plus controller) was applied to the turbulent channel, but Lee *et al.*<sup>30</sup> observed that a fully three-dimensional controller was needed; otherwise, the resulting flow patterns show substantial spanwise variations of wall-shear stress fluctuations, and they had to employ an additional ad-hoc controller to remove the remaining spanwise variations. Lim *et al.*<sup>39</sup> applied an improved three-dimensional version of this LQG controller to the turbulent channel, and obtained about 20% drag reduction. The flow patterns show the same trend as those observed in the turbulent channel with LQR controllers, but the effect is confined to the near-wall region.

The performance of LQG-controllers largely depends on the performance of the estimator. We examined how well the estimator tracks the actual measurement (*i.e.*, how small  $\mathbf{z} - \hat{\mathbf{z}}$  in Eqn. 11 is).<sup>40,39</sup> Our estimator produced excellent tracking, but the estimated internal state ranged from good (near the wall) to poor (away from the wall). Development of an improved reduced-order estimator is key to successful applications of LQG controllers, and we are currently working toward achieving this goal.

### 4.5 Reduction of Non-Normality in Turbulent Channel

The success of linear optimal controllers in the turbulent channel was somewhat unexpected, although we have shown some evidence that a linear mechanism plays an important role in turbulent

boundary layers. In order to further address this question, we turn to a numerical experiment performed by Kim and Lim.<sup>36</sup>

They recognized that the primary reason for non-normality of the linearized Navier-Stokes system is due to  $L_c$  in Eqn. (14). Although  $L_{os}$  itself is not self-adjoint (non-normal), it is  $L_c$  (referred to as the coupling term because  $v$  and  $\omega_y$  are coupled through this term) that makes the operator  $A$  non-normal. Since eigenmodes of a non-normal operator are not orthogonal to each other, they allow transient growth of energy even if the individual modes are stable and decay asymptotically. Some investigators<sup>33</sup> suggest that this non-normal transient growth is responsible for near-wall turbulence structures in turbulent boundary layers. Kim and Lim<sup>36</sup> investigated the role of the coupling term in a fully nonlinear turbulent flow, by considering the following modified nonlinear system:

$$\frac{d}{dt} \begin{bmatrix} \hat{v} \\ \hat{\omega}_y \end{bmatrix} = \begin{bmatrix} L_{os} & 0 \\ 0 & L_{sq} \end{bmatrix} \begin{bmatrix} \hat{v} \\ \hat{\omega}_y \end{bmatrix} + \begin{bmatrix} \mathcal{N}_v \\ \mathcal{N}_{\omega_y} \end{bmatrix}. \quad (19)$$

This modified system can be viewed as representing a virtual turbulent flow with no coupling term, or a turbulent flow with control by which the coupling term is suppressed (see below).

Starting from an initial field obtained from a regular turbulent channel simulation, the above modified nonlinear system was integrated in time and was compared with a nonlinear simulation with the coupling term. It was found that without the coupling term the near-wall structures first disappeared and the flow became laminar (Figs. 12-13). This demonstrates that the linear coupling term plays an essential role in maintaining turbulence in nonlinear flows.

Motivated by the above results, an LQR controller designed to minimize the coupling term was constructed and applied to the channel. Note that this controller can reduce the coupling term but not completely suppress it in contrast to the virtual flow above. The coupling term in the LQR-controlled flow was substantially reduced, and the strength of near-wall turbulence substantially weakened, resulting in about a 20% drag reduction.<sup>39</sup> An LQG controller designed to minimize the coupling term is currently under construction.

## 4.6 Beyond Turbulent Channel Flows

The successful applications of linear controllers in the turbulent channel led us to consider more complex flows. Control of separated flow over an airfoil at a large angle of attack has been studied by many investigators owing to its technological importance. When the angle of attack is increased beyond the stall angle, the flow becomes fully separated, resulting in significant loss of lift. In many

previous studies, periodic blowing and suction at a certain frequency, determined by trial and error, has been used to prevent or minimize stall at high angles of attack.

We plan to develop a control algorithm for the above-mentioned separated flow using the linear control theory discussed in Subsection 4.4. Unlike the turbulent channel or turbulent boundary layer, however, turbulent flow over an airfoil cannot be easily converted into a state-space representation, since the required system information (matrices  $A, B, C$  and  $D$ ) is difficult to obtain. In a situation like this, system identification approaches can be used to model the input/output relationship of the system. Once an approximate model for this complex flow is identified, the same procedure used in channel flow control can be used to design optimal controllers. The underlying assumption here, of course, is that some key dynamics of the separated flow can be captured by a linear model. Whether this assumption is valid, and how successful the approximate model obtained via system identification techniques turns out to be, remains to be seen.

## 5 ISSUES, LIMITATIONS AND CONCLUSION

I have presented a few successful applications of controllers that are fundamentally different from many existing ones in that they were derived from linear control theory, which has not been widely embraced by the fluid mechanics community. These successes are quite promising, as they suggest a new approach for turbulence control, a topic which has been viewed by many as beyond the scope of linear control theory. It turns out that in wall-bounded shear flows a linear mechanism plays an important role in near-wall turbulence dynamics, especially from the perspective of skin-friction drag. This linear mechanism, which exists in the presence of other fundamental nonlinear processes, can be captured by a linear model, and much can be accomplished by utilizing linear control theory. There is some evidence that further fine tuning may lead to even better performance than that shown here. However, there are many outstanding issues that must be resolved before this approach can be fully implemented. Some of these issues are listed below. They are neither in any particular order, nor exhaustive; they simply reflect issues that have come to light during the course of this work.

1. Model reduction. An improved model reduction technique is key to successful applications of linear control theory to flow control in general, and turbulence control in particular. Currently we use a balanced-realization model-reduction approach, in which the original high-

dimensional system is reduced by considering controllability and observability. A reduced-order model should retain the essential features of the original dynamical system. Most existing model-reduction techniques, including ours, aim at reproducing the input-output relationship of the original system, thus accounting for controllability and observability, but they do not account for the control objective. This is certainly not desirable, as it may leave out some important system dynamics, which are relatively less observable or controllable, but nevertheless may contribute significantly to the control objective. Ideally, all three aspects (control objective, controllability and observability) should receive proper weight during the model reduction stage. In this regard, it is worth mentioning that a model reduction purely based on POD (proper orthogonal decomposition) modes may not be appropriate since it gives no consideration to controllability and observability, and perhaps (at least not directly) to the control objective, either.

2. Control objective (or cost function). For the purpose of drag reduction, we have considered several control functions to be minimized (note that the drag itself, which is a mean quantity, cannot be incorporated directly into the cost function), but they are not necessarily the most appropriate ones. In fact, in some examples given here, controllers performed extremely well from the point of minimizing the given cost function – in other words, the controllers met the design objective – but unfortunately they did not lead to correspondingly significant reduction in the mean drag. Whether this implies an inherent limitation of linear controllers for nonlinear flows or simply calls for different cost functions has not yet been determined.
3. Localized control. All examples shown in this paper used controllers designed and applied in wavenumber space. Measurements from distributed sensors are collected and converted into Fourier space, where control input (actuation) is determined and applied (actuation itself can be applied in physical space by converting the control input back to physical space, but that is beside the point). The primary reason behind this approach was that the linearized Navier-Stokes system completely decouples for each wavenumber, thus converting a large linear system into a small linear system for each wavenumber. However, this procedure, which is sometimes referred to as a centralized approach<sup>23</sup> (since it requires central processing of data), requires global sensor information for each actuator. A more desirable approach would be one in which the control input for each actuator is determined solely by information obtained by

neighboring sensors, as in

$$\mathbf{u}(x, z, t) = \int G(x - \xi, z - \eta) \mathbf{z}(\xi, \eta, t) d\xi d\eta, \quad (20)$$

where  $G$  denotes a control kernel in physical space. A key consideration of this approach (referred to as localized or decentralized control) is how well the control kernel can be localized in physical space, which allows determination of the control input,  $\mathbf{u}(x, z, t)$ , based on local  $\mathbf{z}(x, z, t)$ . There is some evidence that this is indeed possible,<sup>23,39</sup> but it requires further investigation.

4. Actuator. In our numerical experiments, we have used the wall-shear stresses as measurements (sensing) and surface blowing and suction as control input (actuation). Shear-stress sensors are currently available and pose no practical problems, but actuators that can deliver the same type of blowing and suction at the wall are not yet available.<sup>41</sup> Furthermore, in our numerical experiments, we have not accounted for any time delay between sensing and actuation, whereas in practice there will be a finite delay due to both actuator response time and data processing time.
5. Numerical issues. Although this is not a control issue, it is worth mentioning here that the system matrix we have to deal with is extremely poorly conditioned (i.e., it has a high condition number) and all computations (e.g., transforming into a Jordan form for model reduction, solving the Riccati equations for the control and estimator gain matrices, etc.) involving the system matrix must be done with care. The effect of under-resolved modes (due to a finite-dimension representation of the infinite-dimension system) and the effect of spurious modes (due to a particular state-space representation) are other examples that require special attention. Some of these modes can be very controllable and/or observable, and therefore can adversely affect the controller design and its performance.
6. Reynolds number. All successful examples thus far, including those conducted by other investigators and not presented here, have been at very low Reynolds numbers. Some investigators believe that there are fundamental changes in the turbulent transport processes in turbulent boundary layers at high Reynolds numbers.<sup>42</sup> Therefore, all current approaches that control near-wall turbulence structures, which according to these investigators are only relevant to low Reynolds number flows, may not be applicable to turbulent boundary layers at high Reynolds

numbers. This remains to be seen. It is worth noting, however, that the riblet surface, which also affects near-wall turbulence structures, has been proven to reduce skin-friction drag during a flight test of a commercial aircraft – an example illustrating that what worked at low Reynolds numbers (both in numerical and laboratory experiments) also worked at a high Reynolds number.

7. Beyond simple flows. It will be extremely interesting to see how far we can push the current approach toward more realistic and complex flows for which we do not have complete system information. The system identification approach is one way to tackle this problem, but it remains to be seen how robust this approach will be, especially for nonlinear flows.

In summary, I have shown that applications of linear control theory to a particular problem of turbulence control result in quite promising results. This is in due large part to the important role of certain linear mechanisms in wall-bounded shear flows. Exploitation of linear mechanisms in other flows may also lead to successful results. Although control theory has emerged as a viable and powerful tool for flow-control problems, there remain many outstanding issues. I expect that further collaborations between control theoreticians and fluid dynamicists will lead to even greater progress in the future.

## ACKNOWLEDGMENTS

I would like to thank my former and current students, postdocs and colleagues at UCLA, Professor Jason Speyer in particular, who has enlightened me about control theory. I would also like to thank my former colleagues at NASA Ames Research Center and Stanford University, Alan Wray, Bob Rogallo, Bill Reynolds and Parviz Moin in particular, from whom I have learned much about turbulence and turbulence simulations. Without their help, winning such a prestigious award would not have been possible; I have been lucky to be where I have been at the right time with the right people. I also gratefully acknowledge the sustained financial support provided by the Air Force Office of Scientific Research (program managers: Drs. James McMichael, Mark Glauser, Tom Beutner, Marc Jacobs, and Berlinda King) and by the Office of Naval Research (program manager: Dr. Pat Purtell) during the course of this work. The computer time provided by NASA Ames Research Center and NSF NPACI Centers is also gratefully acknowledged. Finally, I thank Dr. Gary Coleman for his comments on a draft of this manuscript and Mr. Junwoo Lim for providing

some figures used in this paper.

## References

- [1] D. M. Bushnell, private communication, 1996. A 10% reduction in fuel cost of commercial aircraft would yield a 40% increase in the profit margin of an airplane.
- [2] P. Moin and K. Mahesh. Direct Numerical Simulation: A Tool in Turbulence Research. *Ann. Rev. Fluid Mech.*, **30**:539–578, 1998.
- [3] T. Tsao, F. Jiang, C. Liu, R. Miller, S. Tung, J-B. Huang, D. Babcock, C. Lee, Y-C. Tai, C-M Ho, J. Kim, and R. Goodman. MEMS-Based Active Drag Reduction in Turbulent Boundary Layers. *Microengineering Aerospace Systems*, Helvajian (Ed.). The Aerospace Press, 1999.
- [4] C-M. Ho and Y-C. Tai. Micro-Electro-Mechanical-Systems (MEMS) and Fluid Flows. *Ann. Rev. Fluid Mech.*, **30**:579–612, 1998.
- [5] K. Zhou, J. C. Doyle, and K. Glover. Robust and optimal control. Prentice Hall, 1996.
- [6] P. Moin and J. Kim. Numerical investigation of turbulent channel flow. *J. Fluid Mech.*, **118**, 1982.
- [7] The original plan was for the ILLIAC IV to be used by scientists at the University of Illinois, but student demonstrations led to its removal out of the University. Dr. Hans Marc, then Director of NASA Ames Research Center and a theoretical physicist by training, seized the opportunity to bring the computer to Ames Research Center as he foresaw what the powerful computer could do for scientific research.
- [8] I am much indebted to Alan Wray for recollecting technical details of ILLIAC IV mentioned in this paper.
- [9] S. J. Kline, W. C. Reynolds, F. A. Schraub, and P. W. Runstadler. The structure of turbulent boundary layers. *J. Fluid Mech.*, **30**, 1967.
- [10] H. Choi, P. Moin, and J. Kim. Direct numerical simulation of turbulent flow over riblets. *J. Fluid Mech.*, **255**, 1993.

- [11] A. G. Kravchenko, H. Choi, and P. Moin. On the relation of near-wall streamwise vortices to wall skin friction in turbulent boundary layers. *Phys. Fluids A*, **5**(12):3307–3309, 1993.
- [12] J. Kim, P. Moin, and R. D. Moser. Turbulence statistics in fully developed channel flow at low Reynolds number. *J. Fluid Mech.*, **177**:133–166, 1987.
- [13] J. M. Hamilton, J. Kim, and F. Waleffe. Regeneration mechanisms of near-wall turbulence structures. *J. Fluid Mech.*, **287**:317–348, 1995.
- [14] F. Waleffe and J. Kim. How streamwise rolls and streaks self-sustain in a shear flow. *Self-Sustaining Mechanisms of Wall Turbulence* (ed. Panton). Computational Mechanics Publications, 1997.
- [15] J. Jiménez and A. Pinelli. The autonomous cycle of near-wall turbulence. *J. Fluid Mech.*, **389**:335–359, 1999.
- [16] W. Schoppa and H. Hussain. Coherent structure generation in near-wall turbulence. *J. Fluid Mech.*, **453**:57–108, 2002.
- [17] In our original paper, we used the 2nd-order Adams-Bashforth (AB) method. Since then it has been switched to a low-storage 3rd-order Runge-Kutta (RK) scheme. The 3rd-order RK scheme is the preferred method, and I mention this here as I have noticed that many investigators are still using the 2nd-order AB method in similar calculations, perhaps due to our original report.
- [18] H. Choi, P. Moin, and J. Kim. Active turbulence control for drag reduction in wall-bounded flows. *J. Fluid Mech.*, **262**:75–110, 1994.
- [19] E. P. Hammond, T. R. Bewley, and P. Moin. Observed mechanisms for turbulence attenuation and enhancement in opposition-controlled wall-bounded flows. *Phys. Fluids*, **10**(9):2421–2423, 1998.
- [20] C. Lee, J. Kim, D. Babcock, and R. Goodman. Application of neural networks to turbulence control for drag reduction. *Phys. Fluids*, **9**(6):1740–1747, 1997.
- [21] H. Choi, R. Teman, P. Moin, and J. Kim. Feedback control for unsteady flow and its application to the stochastic burgers equation. *J. Fluid Mech.*, **253**, 1993.



- [22] C. Lee, J. Kim, and H. Choi. Suboptimal control of turbulent channel flow for drag reduction. *J. Fluid Mech.*, **358**:245–258, 1998.
- [23] T. R. Bewley. Flow control: new challenges for a new Renaissance. *Progress in Aerospace Sciences*, 37:21–58, 2001.
- [24] T. R. Bewley, P. Moin, and R. Temam. DNS-based predictive control of turbulence: an optimal benchmark for feedback algorithms. *J. Fluid Mech.*, **447**:179–226, 2001.
- [25] S. S. Joshi, J. L. Speyer, and J. Kim. A systems theory approach to the feedback stabilization of infinitesimal and finite-amplitude disturbances in plane Poiseuille flow. *J. Fluid Mech.*, **332**:157–184, 1997.
- [26] S. S. Joshi, J. L. Speyer, and J. Kim. Finite dimensional optimal control of Poiseuille flow. *J. Guidance, Control, and Dynamics*, **22**:340–348, 1999.
- [27] T. R. Bewley and S. Liu. Optimal and robust control and estimation of linear paths to transition. *J. Fluid Mech.*, **365**:305–349, 1998.
- [28] L. Cortelezzi, K. Lee, J. Kim, and J. L. Speyer. Skin-friction drag reduction via robust reduced-order linear feedback control. *Int. J. Comp. Fluid Dyn.*, **11**:79–92, 1998.
- [29] L. Cortelezzi and J. L. Speyer. Robust reduced-order controller of laminar boundary layer transitions. *Phys. Rev. E*, **58**:1906, 1998.
- [30] K. Lee, L. Cortelezzi, J. Kim, and J. L. Speyer. Application of reduced-order controller to turbulent flows for drag reduction. *Phys. Fluids*, **13**(5):1321–1330, 2001.
- [31] A special symposium on this topic was held during the 54th APS/DFD meeting in San Diego, CA, November 16-18, 2001. The interested reader is referred to the Bulletin of American Physical Society, **46**, No. 10, November, 2001.
- [32] K. M. Butler and B. F. Farrell. Three-dimensional optimal perturbations in viscous shear flow. *Phys. Fluids A*, **4**(8):1637–1650, 1992.
- [33] K. M. Butler and B. F. Farrell. Optimal perturbations and streak spacing in wall-bounded turbulent shear flow. *Phys. Fluids A*, **5**(3):774–777, 1993.

- [34] S. C. Reddy and D. S. Henningson. Energy growth in viscous channel flows. *J. Fluid Mech.*, **252**:209–238, 1993.
- [35] B. F. Farrell and P. J. Ioannou. Stochastic forcing of the linearized Navier-Stokes equations. *Phys. Fluids A*, **5**(11):2600–2609, 1993.
- [36] J. Kim and J. Lim. A linear process in wall-bounded turbulent shear flows. *Phys. Fluids*, **12**(8):1885–1888, 2000.
- [37] B. Bamieh and M. Dahleh. Energy amplification in channel flows with stochastic excitation. *Phys. Fluids*, **13**(11):3258–3269, 2001.
- [38] From a control point of view, this is actually the ‘worst’ disturbance; we employ this commonly-used term in quotes to avoid confusion with optimal control.
- [39] J. Lim. *A Linear Control in Turbulent Boundary Layers*. Ph.D. dissertation, University of California, Los Angeles, 2002.
- [40] J. Lim, J. Kim, S. Kang, and J. L. Speyer. Linear controllers for turbulent boundary layers. *Bulletin of the American Physical Society*, **46**(10):156, 2001.
- [41] A synthetic jet comes close as far as the blowing is concerned. The flow pattern during the suction phase of a synthetic jet is, however, quite different from that of the surface suction used in the numerical experiment.
- [42] J. C. R. Hunt, private communication, 2001.

## Figure Captions

Figure 1. Marker particles in a motion picture of a simulated flow (left) and hydrogen bubbles in a laboratory experiment by Kline *et al.*<sup>9</sup> (right).

Figure 2. Skin-friction in turbulent boundary layers. Plan view of contours of spanwise vorticity at the wall, showing high skin-friction regions indicated by blue and green (top). Cross section view of the high skin-friction region marked by the straight line in the top figure (lower right corner), showing a pair of streamwise vortices in the wall region. Colors denote the magnitude of streamwise vorticity while the vectors indicate the wall-normal and spanwise components of the velocity in the plane (bottom).

Figure 3. A schematic illustrating opposition control.

Figure 4. A schematic illustrating a neural network representing an adaptive inverse model of the Navier-Stokes plant.

Figure 5. Contours of streamwise wall-shear stress in  $(x, z)$ -plane in regular (top) and NN-controlled (bottom) channel.

Figure 6. Contours of streamwise vorticity in  $(y, z)$ -plane in regular channel (top) and NN-controlled channel (bottom).

Figure 7. Time evolution of an 'optimal' disturbance with and without control: —, uncontrolled; ----, opposition control; — —, an LQR controller.

Figure 8. Time evolution of mean wall-shear stress (normalized by its value when control started) in turbulent channel: —, uncontrolled; others, various LQR controllers.

Figure 9. Contours of streamwise vorticity in  $(y, z)$ -plane in regular channel (top) and in channel with an LQR-controller, which minimizes wall-shear stress fluctuations (bottom).

Figure 10. Contours of wall-shear stress in  $(x, z)$ -plane in regular channel (top) and in channel with an LQR-controller, which minimizes wall-shear stress fluctuations (bottom).

Figure 11 Time evolution of mean wall-shear stress (normalized by its value when control started) in channel with an LQR controller, which accounts for the change of the mean flow: —, uncontrolled; others, with a gain-scheduled LQR controller. Both gain-scheduled LQR controllers led to complete laminarization.

Figure 12. Time evolution of mean wall-shear stress (normalized by its value when control started) with and without the linear coupling term: —, regular channel; ----, channel without the coupling term.

Figure 13. Contours of streamwise vorticity in  $(y - z)$ -plane: (a)  $t^+ = 0$ ; (b)  $t^+ = 20$ ; c)  $t^+ = 200$ . Note that  $L_c = 0$  only in the upper-half of the channel.

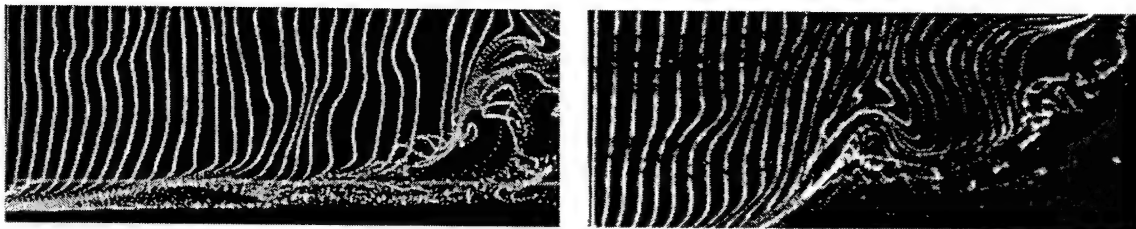


Figure 1: Marker particles in a motion picture of a simulated flow (left) and hydrogen bubbles in a laboratory experiment by Kline *et al.*<sup>9</sup> (right).

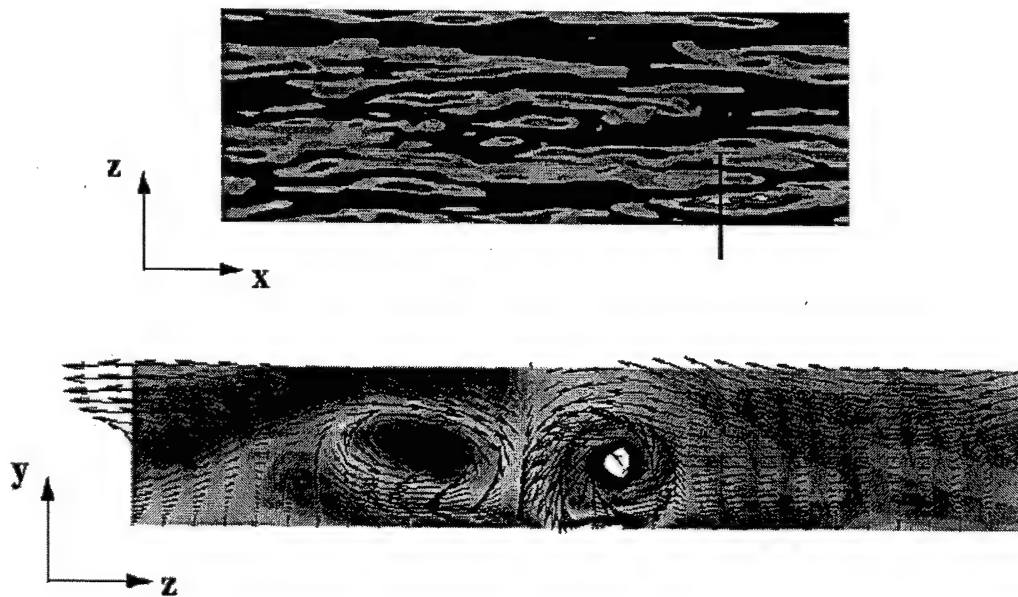


Figure 2: Skin-friction in turbulent boundary layers. Plan view of contours of spanwise vorticity at the wall, showing high skin-friction regions indicated by blue and green (top). Cross section view of the high skin-friction region marked by the straight line in the top figure (lower right corner), showing a pair of streamwise vortices in the wall region. Colors denote the magnitude of streamwise vorticity while the vectors indicate the wall-normal and spanwise components of the velocity in the plane (bottom).

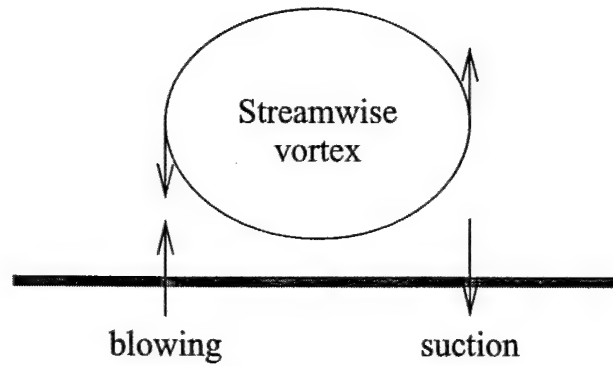


Figure 3: A schematic illustrating opposition control.

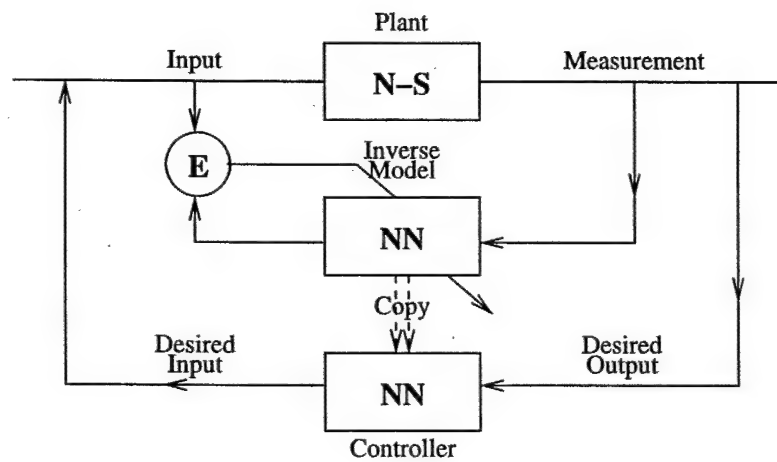


Figure 4: A schematic illustrating a neural network representing an adaptive inverse model of the Navier-Stokes plant.

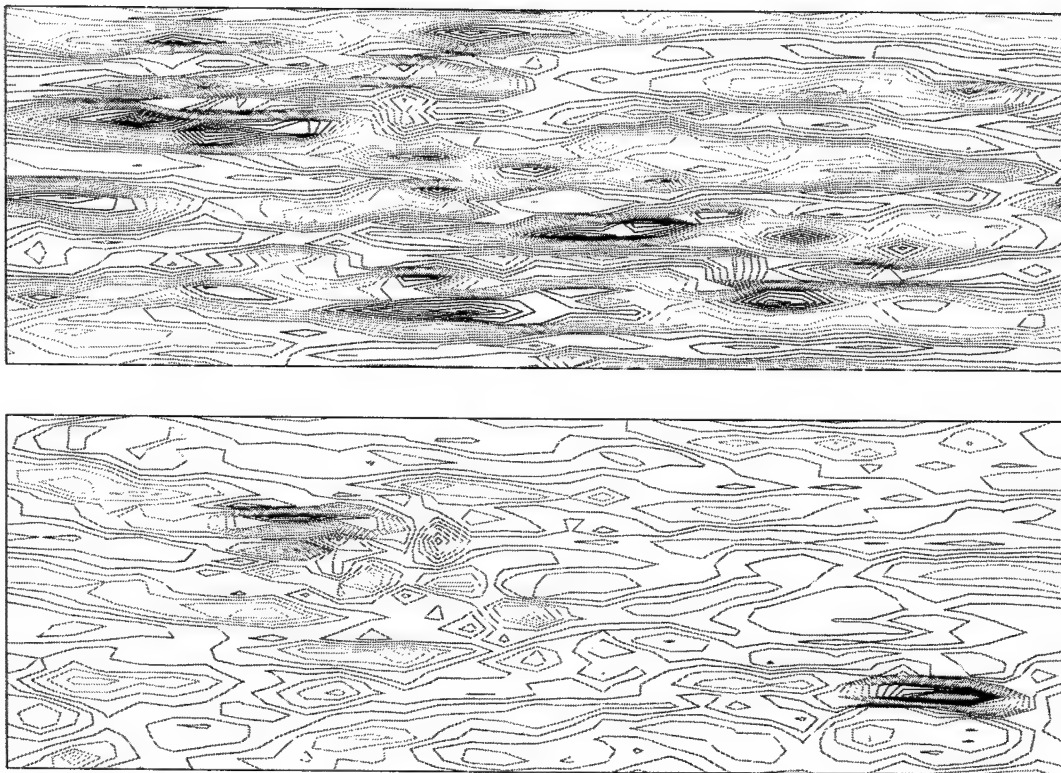


Figure 5: Contours of streamwise wall-shear stress in  $(x, z)$ -plane in regular (top) and NN-controlled (bottom) channel.

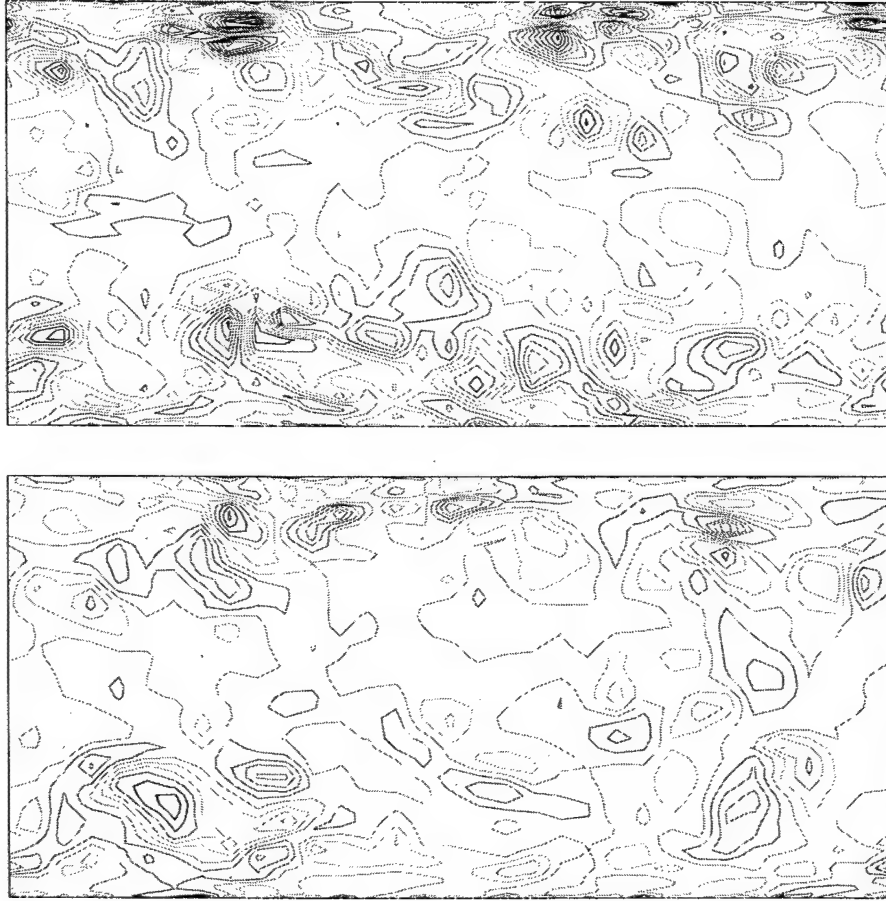


Figure 6: Contours of streamwise vorticity in  $(y, z)$ -plane in regular channel (top) and NN-controlled channel (bottom).



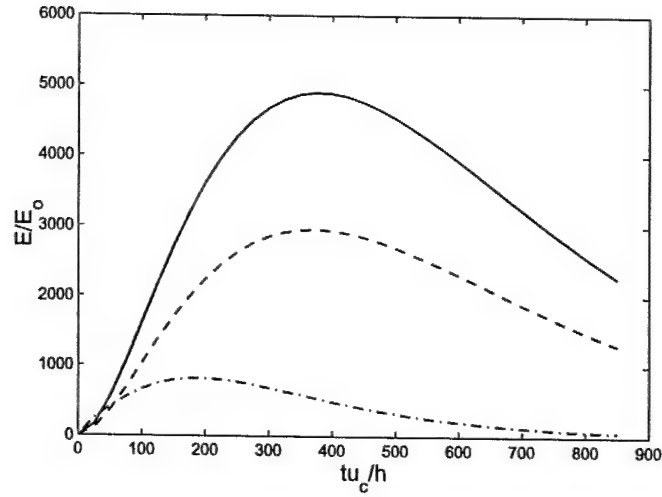


Figure 7: Time evolution of an 'optimal' disturbance with and without control: —, uncontrolled; ----, opposition control; —·—, an LQR controller.

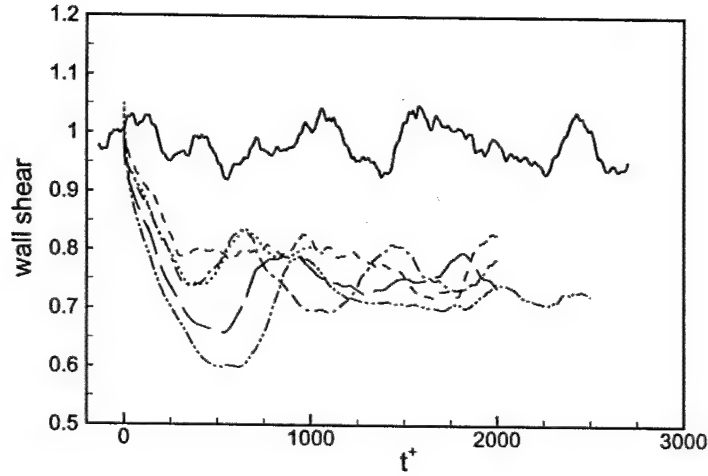


Figure 8: Time evolution of mean wall-shear stress (normalized by its value when control started) in turbulent channel: —, uncontrolled; others, various LQR controllers.

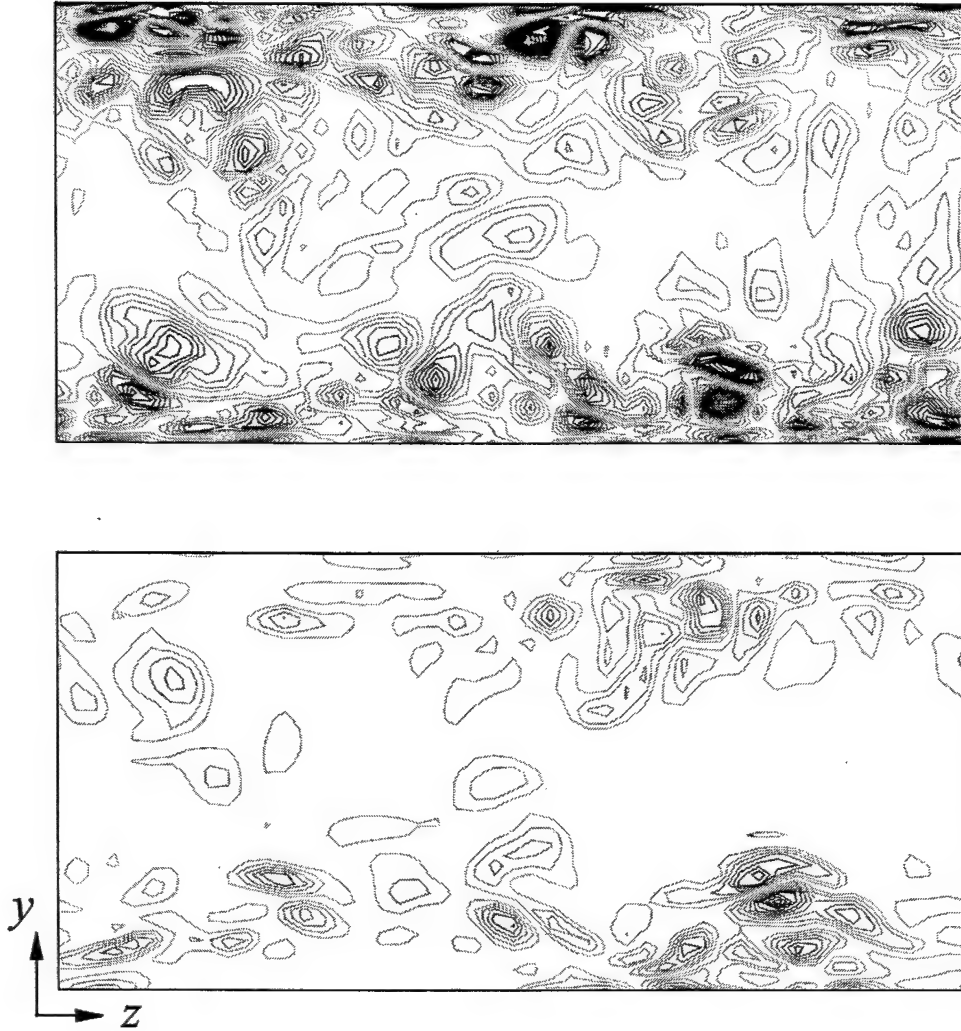


Figure 9: Contours of streamwise vorticity in  $(y, z)$ -plane in regular channel (top) and in channel with an LQR-controller, which minimizes wall-shear stress fluctuations (bottom).

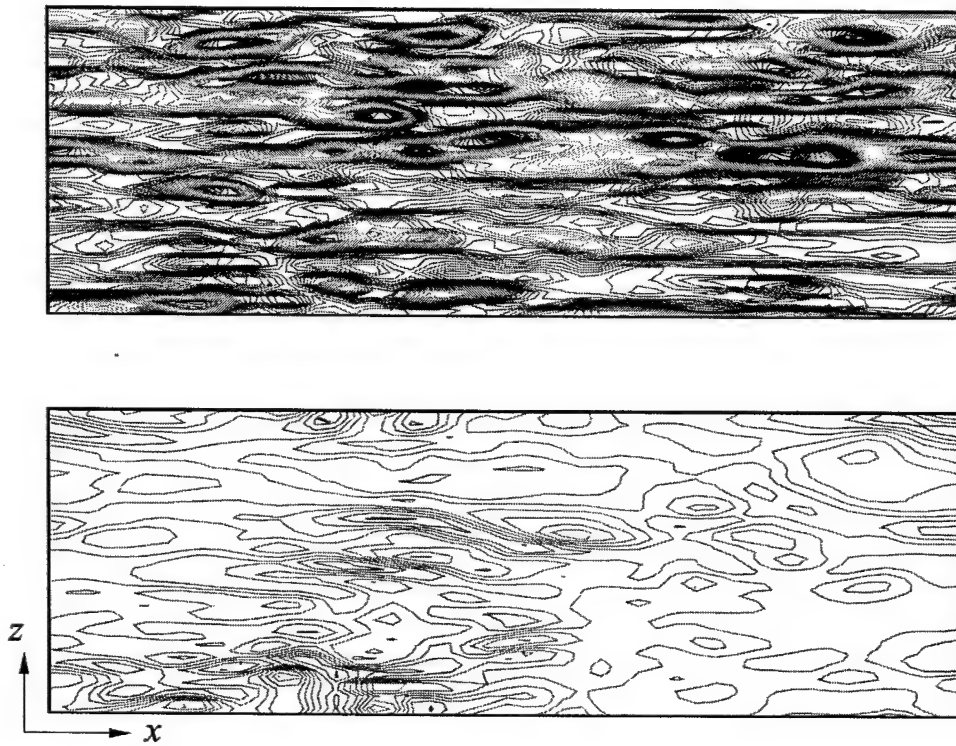


Figure 10: Contours of wall-shear stress in  $(x, z)$ -plane in regular channel (top) and in channel with an LQR-controller, which minimizes wall-shear stress fluctuations (bottom).

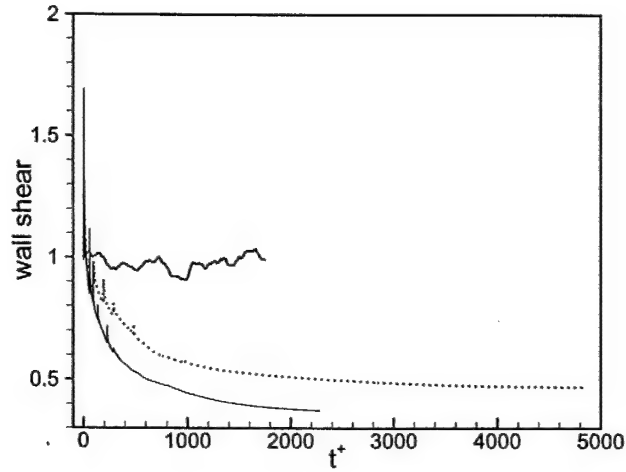


Figure 11: Time evolution of mean wall-shear stress (normalized by its value when control started) in channel with an LQR controller, which accounts for the change of the mean flow: —, uncontrolled; others, with a gain-scheduled LQR controller. Both gain-scheduled LQR controllers led to complete laminarization.

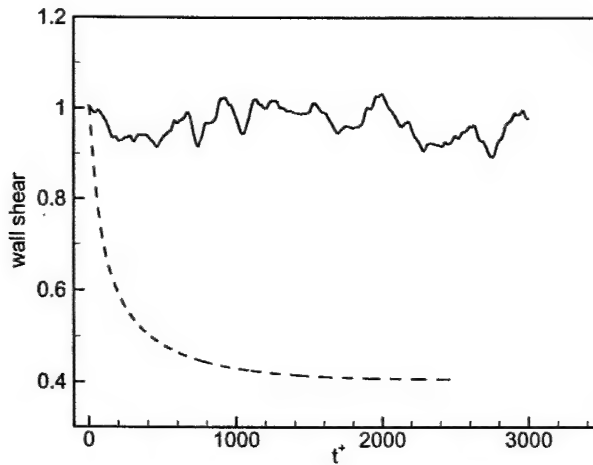


Figure 12: Time evolution of mean wall-shear stress (normalized by its value when control started) with and without the linear coupling term: —, regular channel; ----, channel without the coupling term.

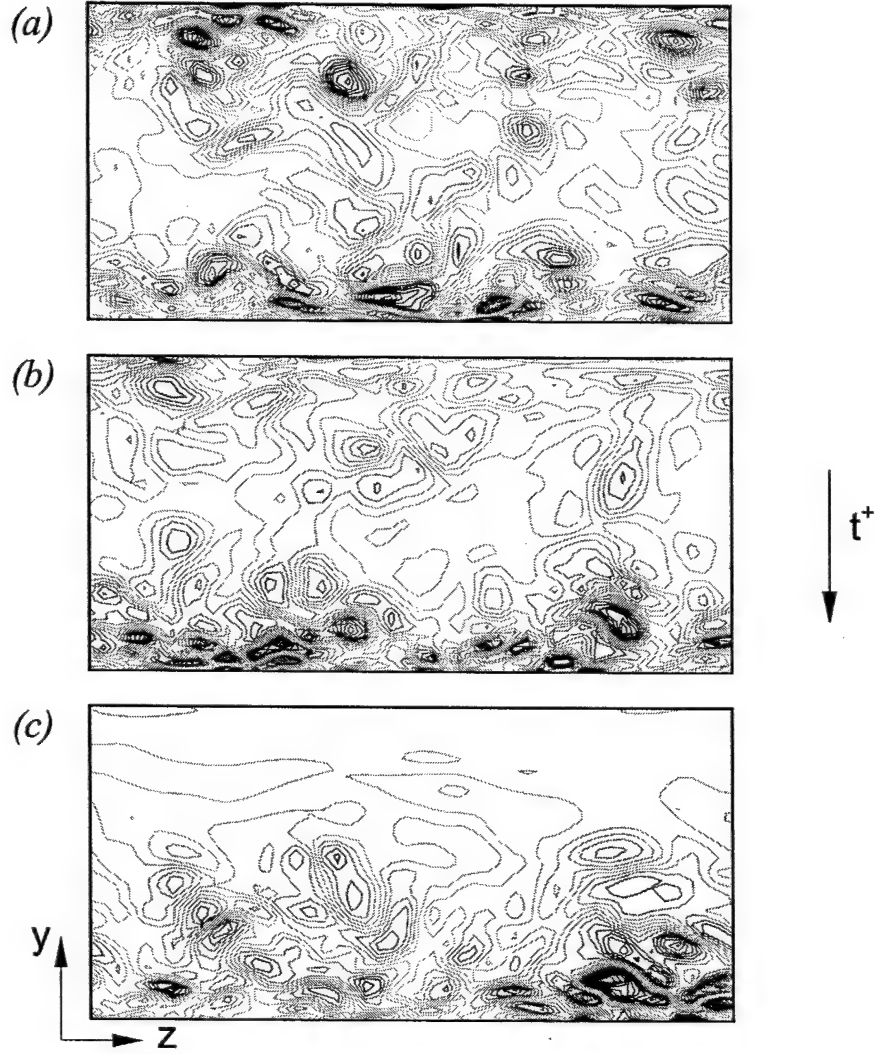


Figure 13: Contours of streamwise vorticity in  $(y-z)$ -plane: (a)  $t^+ = 0$ ; (b)  $t^+ = 20$ ; c)  $t^+ = 200$ . Note that  $L_c = 0$  only in the upper-half of the channel.

We have also shown that the transient responses incurred at the initial time can be reduced significantly by increasing  $Ra$  to its operating value in small increments. This technique allows us to initialize the estimator at each increment of  $Ra$  and consequently avoid controller saturations. Furthermore, by making incremental changes in  $Ra$  and using a controller designed to stabilize the system in a region about the design values, the value of the maximum value of  $Ra$  could be increased further, even though there will be unstable regions formed below stable regions in  $Ra$ .

So far, we have assumed that the order of the controller is equal to the order of the plant. In full numerical simulations and experiments, controller designs based on reduced-order models are more practical for implementation (see, for example, Cortelezzi & Speyer 1998; Armaou & Christofides 2000). In our current model the actuation is assumed to be distributed continuously. In practice it will be discrete and implementation issues need to be addressed.

This research is supported by a grant from United States Air Force (Grant no. F49620-93-1-0332), and also by NASA Microgravity Physics Program (NAG3-1819) in the preliminary stage. We thank R. E. Kelly and R. T. M'Closkey for their encouragement and numerous stimulating discussions on the subject during the course of this study.

## REFERENCES

- ARMAOU, A. & CHRISTOFIDES, P. D. 2000 Feedback control of the Kuramoto-Sivashinsky equation. *Physica D* **137**, 49–61.
- BRYSON, A. E. & HO, Y. C. 1969 *Applied Optimal Control*. Xerox, Waltham, MA.
- CHANDRASEKHAR, S. 1961 *Hydrodynamic and Hydromagnetic Stability*. Oxford University Press.
- CORTELEZZI, L. & SPEYER, J. L. 1998 Robust reduced-order controller of laminar boundary layer transitions. *Phys. Rev. E* **58**, 1906–1910.
- CROSS, M. C. & HOHENBERG, P. C. 1993 Pattern formation outside of equilibrium. *Rev. Mod. Phys.* **65**, 851–1112.
- DOYLE, J. C. & STEIN, G. 1979 Robustness with observers. *IEEE Trans. Automat. Contr.* **AC-24**, 607–611.
- GOTTLIEB, D. & ORSZAG, S. A. 1981 *Numerical Analysis of Spectral Methods: Theory and Applications*. SIAM, Philadelphia.
- HOWLE, L. E. 1997a Linear stability analysis of controlled Rayleigh-Bénard convection using shadowgraphic measurement. *Phys. Fluids* **9**, 3111–3113.
- HOWLE, L. E. 1997b Control of Rayleigh-Bénard convection in a small aspect ratio container. *Int. J. Heat Mass Transfer* **40**, 817–822.
- HOWLE, L. E. 1997c Active control of Rayleigh-Bénard convection. *Phys. Fluids* **9**, 1861–1863.
- HOWLE, L. E. 2000 The effect of boundary properties on controlled Rayleigh-Bénard convection. *J. Fluid Mech.* **411**, 39–58.
- JOSHI, S. S., SPEYER, J. L. & KIM, J. 1997 A systems theory approach to the feedback stabilization of infinitesimal and finite-amplitude disturbances in plane Poiseuille flow. *J. Fluid Mech.* **332**, 157–184.
- JOSHI, S. S., SPEYER, J. L. & KIM, J. 1999 Finite dimensional optimal control of Poiseuille flow. *J. Guidance, Control Dyn.* **22**, 340–348.
- KWAKERNAK, H. & SIVAN, R. 1972 *Linear Optimal Control Systems*. John Wiley & Sons.
- RHEE, I. & SPEYER, J. L. 1991 A game theoretic approach to a finite-time disturbance attenuation problem. *IEEE Trans. Automat. Contr.* **36**, 1021–1032.
- TANG, J. & BAU, H. H. 1993 Stabilization of the no-motion state in Rayleigh-Bénard convection through the use of feedback control. *Phys. Rev. Lett.* **70**, 1795–1798.
- TANG, J. & BAU, H. H. 1994 Stabilization of the no-motion state in the Rayleigh-Bénard problem. *Proc. R. Soc. Lond. A* **447**, 587–607.

- TANG, J. & BAU, H. H. 1998*a* Experiments on the stabilization of the no-motion state of a fluid layer heated from below and cooled from above. *J. Fluid Mech.* **363**, 153–171.
- TANG, J. & BAU, H. H. 1998*b* Numerical investigation of the stabilization of the no-motion state of a fluid layer heated from below and cooled from above, *Phys. Fluids* **10**, 1597–1610.
- TURAN, L., MINGORI, D. L. & GOODWIN, G. C. 1994 Loop transfer recovery design using biased and unbiased controllers. *IEEE Trans. Automat. Contr.* **39**, 601–605.

APPENDIX D:  
Active Suppression of Finite Amplitude  
Rayleigh-Bénard Convection  
*accepted to J. Fluid Mech.*



# Active suppression of finite amplitude Rayleigh-Bénard convection

By A. C. OR AND J. L. SPEYER

Department of Mechanical & Aerospace Engineering, University of California, Los Angeles,  
CA 90095-1597, USA

(Received 14 May 2002 and in revised form 10 November 2002)

We study by a fully nonlinear, three-dimensional pseudospectral, time-splitting simulation the feedback control of a layer of fluid heated from below. The initial condition corresponds to a steady, large-amplitude, preferred convection state obtained at Prandtl number of 7.0 and Rayleigh number of  $10^4$ , which is about six times the Rayleigh critical value. A robust controller based on the LQG (Linear-Quadratic-Gaussian) synthesis method is used. Both sensors and actuator are thermal-based, planar, and assumed to be continuously distributed. The simulated results show that large-amplitude steady-state convection rolls can be suppressed by the linear LQG controller action. The Green's function of the controller gives the shape of the control action corresponding to a point measurement. In addition, for Rayleigh numbers below the proportional feedback control stability limit, this controller appeared to be effective in damping out steady-state convection rolls as well. However, in a region very near the proportional control stability limit, proportional control action induces subcritical g-type hexagonal convection, which is obtained here through direct simulations. Note that well above this proportional control limit, the LQG still damps out all convection. Check cases to validate the nonlinear plant model are also performed by comparison with published results.

---

## 1. Introduction

Active suppression of onset of convection in a layer of fluid has potentially important applications in improving the material that goes through solidification in a mould. For instance, during the growth phase of large silicon wafers or composite materials, a large thermal gradient typically causes undesirable convective motions in the melt. To understand the active control of the realistic manufacturing process, an idealized system is an important starting point. To this end Rayleigh-Bénard convection is ideal for vigorous theoretical analysis.

Considerable theoretical studies have employed the linear feedback control to increase the stability threshold of the purely heat conductive state so that no convection occurs despite the presence of a large thermal gradient (Tang & Bau 1993, Tang & Bau 1994, Tang & Bau 1998a,b, Howle 1997a,b,c, Howle, 2000, Or et al. 2001). These studies used the linear plant model and employed a simple controller using the proportional feedback. The implantable sensor and actuator are assumed to be of the thermal type and continuously distributed spatially on the horizontal plane. Analysis as well as experimental results in general indicate that the proportional controller will stabilize the basic state up to Rayleigh number ( $Ra$ ) of 3 to 4 times its critical value of the basic state (see Tang & Bau 1994, Howle 1997a). Furthermore, as shown in Tang and Bau (1994), a controller-induced oscillatory instability occurs at a large gain. A linear-quadratic-gaussian (LQG) controller has also been studied (Or et al. 2001) to increase the region of stabilization and with a higher margin of robustness. First, the stability limit can be raised to about 14 times the critical value of  $Ra$ . Second, the gain and phase margins about the design point of the controller appear adequate for practical implementation.

To develop a control design to be implementable for applicational processes (such as for crystal growth or a melt), it is crucial to understand the control process for simpler

geometry and material properties. We have been focused on an Oberbeck-Boussinesq model for a horizontal layer of fluid. The plant dynamics is known as Rayleigh-Bénard convection (RBC) (Cross and Hohenberg, 1993). As a first step the performance of the linear controller design for the linear plant dynamics is reported in Or et al. (2001). In this paper, as a step further the focus is turned to the performance of the linear controller design for the fully nonlinear plant dynamics.

It is well known that in a large layer of heated fluid, convection occurs as a steady pattern of two-dimensional rolls. The two-dimensional convection rolls and the stability properties were investigated in detail by Clever & Busse (1974) and Busse & Clever (1979). For the heated layer corresponding to  $Ra > Ra_{c0}$  ( $Ra_{c0}$  is computed theoretically to have value 1707.762 up to 3 decimal places), the stable roll pattern occurs only within a band of wavenumber centered approximately about the critical wavenumber  $\alpha_c = 3.117$ . Within the stable band the rolls realized do not necessarily have a preferred length scale. Indeed, their wavelength appears to be dictated by the initial conditions used to select the rolls and by the manner that the basic state temperature is prescribed spatially and temporally. The band is bounded on both sides by instabilities that pertains to changing the wavelength of the rolls but not changing the planform. As the induced rolls acquire a wavelength too large or too small, an instability will occur to shift their length scale back to a value close to the critical value. As the value of  $Ra$  increases, the rolls will at some point become unstable and the convection structure will converge to a pattern with more complex spatial or temporal structure. The exact value of  $Ra$  that the transition occurs is wavenumber dependent. For Prandtl number ( $Pr$ ) of 7.0, for instance, the two-dimensional rolls become unstable to a three-dimensional bimodal convection at roughly  $Ra \approx 25Ra_{c0}$  at the wavenumber about 2.0 (see the experimental observations presented in Fig. 11, Busse & Clever (1979)). The transition highlights a sufficiently strong thermal

boundary layer effect, made possible at  $Ra$  values. The transition to three-dimensional convection occurs at a significantly higher  $Ra$  threshold than the closed-loop stability limit of  $14.5Ra_{c0}$  based on the linear LQG controller (Or et al. 2001). For our control analysis here, therefore, we only need to consider the two-dimensional rolls as the initial state of convection to be controlled.

Our present control problem can be investigated most effectively by the use of time-domain analysis. A three-dimensional, fully nonlinear pseudospectral model using time-splitting integration method is developed, based on the Oberbeck-Boussinesq equations. The proportional feedback control controller is easily implementable. This case provides the check cases for code validation purposes. Certain flow patterns that are known to be induced by the controller effects, such as the oscillation mode (Tang & Bau 1994) and the g-type hexagons (Or & Kelly 2001), can be obtained here from the direct numerical simulations and compared with those reported from previous analyzes. In Section 2, the nonlinear plant model and the LQG controller will be briefly described. The results will be presented in Section 3, followed by the conclusion in Section 4.

## 2. Mathematical Formulation

### (a) Nonlinear Plant Model and Numerical Solution

The nonlinear plant model is governed by the Oberbeck-Boussinesq equations for a horizontal layer of fluid. In the nondimensional form  $d$ ,  $d^2/\kappa$ ,  $\kappa/d$ ,  $\kappa/d^2$ ,  $\rho(\kappa/d)^2$  and  $\Delta T$  are used as the scales of length, time, velocity, vorticity, pressure and temperature, where  $d$  is the layer thickness,  $\kappa$  and  $\rho$  are the mean thermal diffusivity and density of the fluid, and  $\Delta T$  is the temperature difference between the upper and lower wall in the purely

conductive basic state. The governing nondimensional equations are,

$$Pr^{-1}\partial_t \mathbf{v} = Pr^{-1}\mathbf{v} \times \boldsymbol{\omega} + \mathbf{k}Ra\theta - \nabla\pi + \nabla^2 \mathbf{v} , \quad (2.1)$$

$$\partial_t \theta = -\mathbf{v} \cdot \nabla \theta + w + \nabla^2 \theta , \quad (2.2)$$

$$\nabla \cdot \mathbf{v} = 0 , \quad (2.3)$$

where  $\mathbf{v} = (u, v, w)$  is the velocity vector field,  $\boldsymbol{\omega} = \nabla \times \mathbf{v}$  is the vorticity,  $\pi = p + \mathbf{v} \cdot \mathbf{v}/2$  is the pressure head,  $\theta$  is the perturbation temperature and  $\mathbf{k}$  is unit vector in the  $z$ -direction. The two external parameters are Rayleigh and Prandtl numbers, given by  $Ra = g\Delta T d^3 / \nu \kappa$  and  $Pr = \nu / \kappa$  where  $\nu$  is the mean kinematic viscosity. The continuity equation (2.3) applies only when the flow is incompressible.

The velocity field is assumed to be nonpermeable and non-slip at the upper and lower walls, thus subject to

$$\mathbf{v}(x, y, 0, t) = \mathbf{0} , \quad \mathbf{v}(x, y, 1, t) = \mathbf{0} . \quad (2.4)$$

The temperature field, on the other hand, is assumed to satisfy the isothermal condition at the upper wall. The lower wall is non-isothermal due to the action of the thermal actuation. It is assumed that a control temperature  $\theta_c(x, y, t)$  can be imposed. The upper and lower thermal boundary conditions for the perturbation field are therefore

$$\theta(x, y, 1, t) = 0 , \quad \theta(x, y, 0, t) = \theta_c(x, y, t) . \quad (2.5)$$

In order to perform the feedback control, the perturbation temperature field has to be measured in the fluid. In our model three sensor planes are embedded in the layer at carefully chosen levels at  $z = z_s$  (with  $s = 1, 2, 3$ ). For analysis purpose these sensor planes are assumed to exert no blockage effects on the flow field. They measure the planar temperature distribution in the layer,

$$\theta(x, y, z_s, t) = \theta_s(x, y, t) , \quad s = 1, 2, 3 . \quad (2.6)$$

Assuming a continuous-distributed sensor,  $\theta_s(x, y, t)$  are known at sampled points and time.

In the numerical scheme the dependent variables  $u$ ,  $v$ ,  $w$ ,  $p$  and  $\theta$  are expressed by the following truncated, triple sums,

$$\begin{bmatrix} u \\ v \\ w \\ p \\ \theta \end{bmatrix} (x, y, z, t) = \text{Re} \left\{ \sum_{n=0}^N \sum_{k=0}^K \sum_{m=-M+1}^M \begin{bmatrix} u_{kmn} \\ v_{kmn} \\ w_{kmn} \\ p_{kmn} \\ \theta_{kmn} \end{bmatrix} (t) T_n(z) e^{i(k\alpha_x x + m\alpha_y y)} \right\} \quad (2.7)$$

where  $\text{Re}$  denotes the real part of the sum,  $\alpha_x$  and  $\alpha_y$  are the fundamental wavenumbers in the  $x$  and  $y$  directions, respectively. The asymmetric treatment of the indices  $k$  and  $m$  reduces the number of coefficients by half because the velocity, pressure and temperature are real dependent variables (see Marcus, 1984). These two parameters are prescribed in the model. The functions  $T_n(z)$  ( $n = 0, 1, \dots$ ) denote the Chebyshev polynomials. Note that a linear coordinate transformation is implicitly assumed to convert the Chebyshev function domain between  $\pm 1$  to our physical range  $0 \leq z < 1$ . The actuator and sensor temperatures,  $\theta_c$  and  $\theta_s$  ( $s = 1, 2, 3$ ), are planar (two-dimensional). They are expanded in double series in a similar fashion,

$$\begin{bmatrix} \theta_s(z_1, t) \\ \theta_s(z_2, t) \\ \theta_s(z_3, t) \\ \theta_c(0, t) \end{bmatrix} (x, y, t) = \text{Re} \left\{ \sum_{k=0}^K \sum_{m=-M+1}^M \begin{bmatrix} \theta_{km,s}(z_1, t) \\ \theta_{km,s}(z_2, t) \\ \theta_{km,s}(z_3, t) \\ \theta_{km,c}(0, t) \end{bmatrix} e^{i(k\alpha_x x + m\alpha_y y)} \right\}, \quad (2.8)$$

In our terminology, the lower thermal boundary condition (2.5) and the sensor equations (2.6) are, respectively, the input to and output from the nonlinear plant model.

The nonlinear equations, together with the boundary and the continuity equations are

then solved numerically by using the pseudospectral, time-splitting integration technique (Gottlieb & Orszag 1977, Canuto et al. 1986, Bodenschatz et al. 2000). Marcus (1984) provided a detailed description of the implementation of the method for the Taylor-vortex flow simulations. Using the time-splitting method, an integration time step is split into 3 fractional steps. The first is a nonlinear fractional step, typically done using an explicit, second-order Adams-Bashforth scheme,

$$\mathbf{v}^{N+1/3} = \mathbf{v}^N + \Delta t \frac{3}{2} [\mathbf{v}^N \times \boldsymbol{\omega}^N + PrRa\theta^N \mathbf{k}] - \Delta t \frac{1}{2} [\mathbf{v}^{N-1} \times \boldsymbol{\omega}^{N-1} + PrRa\theta^{N-1} \mathbf{k}] . \quad (2.9)$$

$$\theta^{N+1/3} = \theta^N - \Delta t \frac{3}{2} [\mathbf{v}^N \cdot \nabla \theta^N - w^N] + \Delta t \frac{1}{2} [\mathbf{v}^{N-1} \cdot \nabla \theta^{N-1} - w^{N-1}] . \quad (2.10)$$

The superscript  $N$  here denotes the time step and is not to be confused with the truncation number for the vertical dependence. A significant fraction of the total computation load occurs in computing the nonlinear terms. In the collocation space the nonlinear terms are computed spatially by point-by-point multiplications. However, fast Fourier transforms (FFT) and inverse fast Fourier transforms (IFFT) have to be used to convert the field back and forth between the collocation and the Chebyshev-Fourier spaces. The fast Fourier transform (FFT) and inverse fast Fourier transform (IFFT) routines are obtained from the library of the *Numerical Recipes* (Press et al. 1992), with some minor modifications. For validation, these routines have been checked against the standard *Matlab* FFT and IFFT functions and match up to 15 decimal places. For typical flow fields the truncation errors from FFT and IFFT due to aliasing are substantially small (Marcus 1984, Press et al., 1992). We note that, however, the FFT method can still be computationally demanding for high resolution solutions. The pseudospectral method is generally known to be efficient. There also exists other efficient methods not using the transforms, for instance, the reduced-order Galerkin method (Howle, 1996).

After obtaining the  $(N + 1/3)^{th}$  fractional step with the Adams-Basforth scheme, we

compute the  $(N + 1)^{th}$  step from the following equation,

$$(1 - Pr\Delta t\nabla^2)\mathbf{v}^{N+1} = \mathbf{v}^{N+1/3} - Pr\Delta t\nabla\pi, \quad (2.11)$$

subject to  $\nabla \cdot \mathbf{v}^{N+1} = 0$ . It is noted that in general  $\nabla \cdot \mathbf{v}^{N+1/3} \neq 0$ . The most straightforward procedure for solving Eq.(2.11) appears to be splitting the equation into a pressure step and a viscous step (we refer to it as the direct approach). In the pressure step the flow field subject to a no normal-flow boundary condition at the walls can be solved from a Poisson equation, based on the property that the pressure field is irrotational and the flow field satisfies the continuity constraint (2.3). Next, a diffusive fractional step completes the solution of the fractional velocity and temperature fields by prescribing the no-slip and thermal boundary conditions at the walls. As simple as it appeared, the scheme had problems computing the correct flow field. In his numerical simulation of Taylor vortex flow, Marcus (1984) reported large boundary errors using this direct approach. In his discussions it was argued that the shear may play a role and it is not clear whether a similar problem will occur for RBC. In our study we have applied the direct scheme in our preliminary simulations and observed large errors even for the open-loop simulations. Thus, it appears that the problem is common to both Taylor vortex flows as well as RBC. For more detail about the cause of the large boundary errors in the direct approach, we refer to Marcus (1984). Marcus identified the source of errors and developed a procedure to correct it. His remedy is to further split the fractional solution into a complementary and a particular solution so that the boundary conditions and the continuity equations are satisfied numerically. The procedure, however, involves the additional computation of several Green's functions and seems elaborate. Since the boundary-value problem corresponding to Eq.(2.11) is linear, we anticipate there are simpler alternative approach to resolve the numerical difficulty. Here, we solve the problem involving the pressure and viscous forces as a single step, without splitting the pressure and viscous terms. First, we



use the continuity equation as the constraint and eliminate the two horizontal velocity components in favor of the vertical component. Second, we obtain the solution of the boundary-value problem for  $w$  and  $\theta$ . Finally, we recover  $u$  and  $v$  from  $w$ , Fourier mode by Fourier mode, using again the continuity equation. This scheme seems significantly simpler and has been tested here to be effective. Because of the simplicity, it is worth the description as an alternative approach to the time-splitting procedure.

By eliminating pressure from the Eq.(2.11), we obtain a single scalar equation governing  $w$ ,

$$(1 - Pr\Delta t\nabla^2)\nabla^2\partial_z w^{N+1} = \nabla_{\perp}^2\partial_z w^{N+1/3} - \partial_{zz}^2(\partial_x u^{N+1/3} + \partial_y v^{N+1/3}). \quad (2.12)$$

The equation above is integrated in  $z$ , this gives

$$(1 - Pr\Delta t\nabla^2)\nabla^2 w^{N+1} = \nabla_{\perp}^2 w^{N+1/3} - (\partial_{xz}^2 u^{N+1/3} + \partial_{yz}^2 v^{N+1/3}). \quad (2.13)$$

The integration constant is zero because of the non-slip boundary condition. (This constant will depend on the initial conditions when the case of free-slip boundary conditions is considered). The above equation is of fourth-order spatially. It has to satisfy four boundary conditions, as follows,

$$w^{N+1} = 0, \quad \text{and} \quad \partial_z w^{N+1} = 0, \quad \text{at } z = 0, 1. \quad (2.14)$$

The fourth-order boundary-value problem Eq.(2.12) determines  $w^{N+1}$ . After we have obtained  $w^{N+1}$ , the horizontal velocity components corresponding to  $w^{N+1}$  can be obtained by inverting the continuity and Helmholtz equations Fourier mode by Fourier mode. In the expansion,  $w^{N+1}$  is given by

$$w^{N+1}(x, y, z, t) = \text{Re} \left\{ \sum_{k=0}^K \sum_{m=-M+1}^M w_{km}^{N+1}(z, t) e^{i(k\alpha_x x + m\alpha_y y)} \right\}. \quad (2.15)$$

Similarly, the horizontal velocity components are

$$\begin{bmatrix} u^{N+1}(x, y, z, t) \\ v^{N+1}(x, y, z, t) \end{bmatrix} = \text{Re} \left\{ \sum_{k=0}^K \sum_{m=-M+1}^M \begin{bmatrix} u_{km}^{N+1}(z, t) \\ v_{km}^{N+1}(z, t) \end{bmatrix} e^{i(k\alpha_x x + m\alpha_y y)} \right\}. \quad (2.16)$$

Each pair of coefficients  $(u_{km}^{N+1}, v_{km}^{N+1})$  now satisfies a Helmholtz equation

$$\nabla_{\perp}^2 \begin{bmatrix} u_{km}^{N+1} \\ v_{km}^{N+1} \end{bmatrix} = \alpha_{km}^2 \begin{bmatrix} u_{km}^{N+1} \\ v_{km}^{N+1} \end{bmatrix} \quad (2.17)$$

where  $\alpha_{km} = \{(k\alpha_x)^2 + (m\alpha_y)^2\}^{1/2}$ . The Helmholtz equation together with the continuity equation allows us to solve for  $v_{km}^{N+1}$  in terms of  $w_{km}^{N+1}$ , provided that  $\alpha_{km} \neq 0$ . The condition  $\alpha_{km} \neq 0$  can occur in the case of free-slip wall but not in the case of no-slip wall. We refer to the discussion (on P.970) of Cross and Hohenberg (1993). The perturbation temperature field, on the other hand, is not constrained to have zero mean field. Using the continuity equation, we obtain the horizontal velocity components,

$$u_{km}^{N+1} = \frac{1}{\alpha_{km}^2} \partial_{xz}^2 w_{km}^{N+1}, \quad v_{km}^{N+1} = \frac{1}{\alpha_{km}^2} \partial_{yz}^2 w_{km}^{N+1}. \quad (2.18)$$

#### (b) The Proportional Feedback Controller

In the proportional feedback control, a proportional relationship is constructed between the input and output of the plant. As in the cases studied by Tang and Bau (1994) and Or et al. (2001), only one sensor plane is used and the control law in this case is

$$\theta_c(0, t) = -K_p \theta_s(z_s, t) \quad (2.19)$$

where  $K_p$  is a constant gain and  $z_s$  is the vertical height of the sensor plane. The controller is very simple for this case.

#### (c) The LQG Controller

The theory and design of the LQG controller was described in (Or et al. 2001), so we refer the readers to the paper for the detailed description. In brief, the linear stability equations of the Fourier-decomposed system of convection and the measurement equation are given in matrix form, respectively, by

$$\dot{\mathbf{x}} = \mathbf{A}\mathbf{x} + \mathbf{B}\mathbf{u}, \quad \mathbf{z} = \mathbf{C}\mathbf{x}, \quad (2.20)$$

where the entries of the state vector  $\mathbf{x}$  are the Chebyshev coefficients of velocity and temperature perturbations;  $u$  (measured at plane  $z = 0$ ) and  $\mathbf{z}$  (measured at planes  $z_1, z_2, z_3$ ) are, respectively, the Fourier coefficients of the planar control and measured temperatures. Note that the Fourier-decomposed equations correspond to wavenumber  $\alpha_{km}$  and Rayleigh number  $Ra$ . The following modifications to the original formulation of the controller model (Or et al. 2001) have been made here: (i) the vertical dependence is expanded in terms of the Chebyshev polynomials instead of the beam functions as the basis functions. The expansion procedure, originally based on the Galerkin method, has been converted to the tau method. In the improved numerical procedure, we obtain the exact condition  $\mathbf{D} \equiv \mathbf{0}$ , in contrast to the previous condition that  $\mathbf{D} \rightarrow \mathbf{0}$  only as  $N \rightarrow \infty$ . (ii) We no longer consider the wavenumber as a prescribed parameter here. Instead, an individual modal controller is developed for each set of wavenumbers  $(k\alpha_x, m\alpha_y)$ . There is a set of state-space equations for each wavevector. In total, there are  $2(K+1)M$  sets of  $\mathbf{A}$ ,  $\mathbf{B}$  and  $\mathbf{C}$  matrices to be processed.

The LQG controller is comprised of a Kalman filter and an optimal regulator. The Kalman filter equation and the optimal regulator equation corresponding to the state-space equations (2.20) above are, respectively,

$$\dot{\hat{\mathbf{x}}} = \mathbf{A}^*\hat{\mathbf{x}} + \mathbf{B}^*\mathbf{u} + \mathbf{K}_f(\mathbf{z} - \hat{\mathbf{z}}), \quad \hat{\mathbf{z}} = \mathbf{C}^*\hat{\mathbf{x}}, \quad \mathbf{u} = -\mathbf{K}_c\hat{\mathbf{x}}, \quad (2.21)$$

where  $\hat{\mathbf{x}}$  is the estimate state vector. We distinguish the matrices with asterisk super-

scripts to highlight that the system is computed at a nominal (designed) wavenumber and Rayleigh number,  $(\alpha_{km}^*, Ra^*)$ . The Kalman gain vector  $\mathbf{K}_f$  and the optimal gain vector  $\mathbf{K}_c$  are determined from separate steady-state algebraic Riccati equations. The Kalman filter is used here as a state observer rather than as an estimator since no noises are injected into the system simulation. The cost functional, weighting and filter parameters chosen for controller design are described in detail in Or et al. (2001) which will not be repeated here. For robustness consideration, in the design the Kalman filter input matrix  $\mathbf{G}$  has been set equal to the control input matrix  $\mathbf{B}$ , a step known as the loop transfer recovery to recover the full-state feedback performance of the optimal regulator. The weights for the objective functions, as well as the filter parameters and the loop transfer recovery are described in Or, et al. 2001.

It is worth noting that the LQG controller is a variant of the  $H_\infty$  controller when the disturbance attenuation bound is infinite (see Rhee and Speyer, 1991). In Or et al. 2001, robustness is demonstrated classically by having large gain and phase margins in the closed-loop response. Furthermore, if a full loop transfer recovery is achieved, the full-state feedback LQ regulator performance will have a robustness of  $\pm 60$  deg. phase margin and 6 db to infinite gain margin. Since our system is non-minimal phased, only partial recovery is expected. Since large gain and phase margins were obtained for the linear system, the performance of the LQG controller in terms of robustness should not be expected to be significantly different from that of the  $H_\infty$  controller.

In Fig. 1, we show the three-dimensional nonlinear plant model. The control input and measurement output of the model are Fourier-Chebyshev coefficients rather than their collocation point values. On the other hand, in the physical plant (such as in laboratory experiments) the input and output are physical temperature distributions. Since the LQG controller is formulated in the modal space, when the upper block represents the

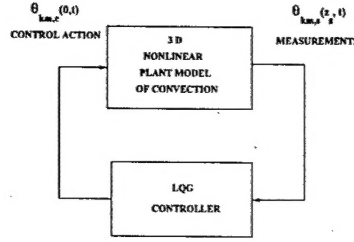


FIGURE 1. The LQG Control Loop Diagram

plant instead of the model, a FFT and an IFFT have to be performed, respectively, at the input and output of the controller. In our case, the LQG controller takes the measurements from the 3D nonlinear plant model (Fourier coefficients at sensor planes) as input and determines a control action (Fourier coefficients at actuator plane) as output. The estimate state vector represents the vertical structure and the state matrices  $\mathbf{A}^*$ ,  $\mathbf{B}^*$ ,  $\mathbf{C}^*$  and  $\mathbf{D}^*$  are computed in terms of the designed values of wavenumber and Rayleigh number,  $\alpha_{km}^*$  and  $Ra^*$ . (see Eq.(3.7) of Or et al. (2001)).

The truncation numbers ( $K = 32, M = 32, N = 32 + 1$ ) considered here are of moderate size. It is still convenient to compute and pre-store the steady-state Kalman gain  $\mathbf{K}_f$  and regulator gain,  $\mathbf{K}_c$ . However, it is not feasible to pre-store the state matrices  $\mathbf{A}^*$  for all the wavenumbers. Instead, we compute  $\mathbf{A}^*$  for each set of wavenumbers at each time step in the time loop. At each time step, the three sensor plane temperatures, in modal coefficients,  $\theta_{km,s}(z_i, t)$  ( $i = 1, 2, 3$ ) (see Eq.(2.8)), are exported from the nonlinear plant model. There are  $6(K + 1)M$  of such coefficients, corresponding to wavenumbers 0 to  $K\alpha_x$  in the  $x$  dependence and  $(-M + 1)\alpha_y$  to  $M\alpha_y$  in the  $y$  dependence. These values are then fed into the controller which consists of the Kalman filter and the regulator. The controller processes the information based on the measured data and determines the control output in terms of a set of  $2(K + 1)M$  modal coefficients for  $\theta_{km,c}(0, t)$ . These values are then inputted into the nonlinear model through the lower-wall boundary condition.

## (d) Green's Function For Point Sensors and Actuators

In some experimental implementations (Tang & Bau 1998a) the sensors and actuators are discrete rather than continuous. For the low-resolution point sensors and actuators (typically with spacing between array points of  $O(d)$ ), it is desirable to stack the arrays of sensor and actuator points vertically on top of each other. Indeed, our result will show that the maximal effect of actuation caused by an impulse on the sensor plane occurs as a point collocated horizontally with the impulse. For a linear system the controller input-to-output relationship can be expressed in the following integral form,

$$\theta_c(x, y, t) = \int \int \int G(x, y, t | x', y', t') \theta_s(x', y', t') dx' dy' dt' \quad (2.22)$$

where  $\theta_c(x, y, t)$  and  $\theta_s(x', y', t')$  are, respectively, the planar actuator and sensor temperature fields. Here  $(x, y)$  and  $(x', y')$  denote coordinates for the actuator and sensor planes, respectively. The kernel  $G(x, y, t, | x', y', t')$  is a Green's function (or an influence function). The first 3 arguments in  $G$  represent the effect and the last 3 represent the cause.

In principle, the input and output of the LQG controller can be represented by a linear differential operator  $L$ . The precise form of  $L$  needs not be specified here, since for our purpose the Green's function will be computed spectrally. In terms of  $L$ , we can describe some general properties of Green's function. The input and output temperatures to the controller is governed by  $L\theta_c = \theta_s$ , subject to appropriate lateral boundary conditions in  $x, y$ . The Green's formula for any two arbitrary functions  $u(x, y, t)$  and  $v(x, y, t)$  can be written as the sum of an integral  $\int \int \int (uLv - vL^+u) dx' dy' dt'$  and a number of terms evaluated at the lateral boundaries  $x = 0, 2\pi/\alpha_x$  and  $y = 0, 2\pi/\alpha_y$ . In the formula  $L^+$  is the adjoint operator of  $L$ . Now if further restriction are imposed on  $u$  and  $v$ , the Green's formula produces some important property about the Green's function. Let

$u = G(x, y, t|x_1, y_1, t')$  and  $v = G^+(x, y, t|x_2, y_2, t')$  where  $G$  and  $G^+$  satisfy, respectively,

$$LG(x, y, t|x_1, y_1, t') = \delta(x-x_1)\delta(y-y_1)\delta(t-t'), \quad L^+G^+(x, y, t|x_2, y_2, t') = \delta(x-x_2)\delta(y-y_2)\delta(t-t'). \quad (2.23)$$

In addition,  $G$  and  $G^+$  satisfy the appropriate lateral boundary conditions and adjoint boundary conditions so that the boundary terms in the Green's formula vanish. The Green's formula becomes

$$\int \int \int (G^+LG - GL^+G^+)dx'dy'dt' \equiv 0. \quad (2.24)$$

Substituting (2.23) in (2.24) we obtain Maxwell's reciprocity relationship  $G(x_2, y_2, t|x_1, y_1, t') = G^+(x_1, y_1, t|x_2, y_2, t')$ . In our problem the lateral boundary conditions are periodic. The differential operators in  $x$  and  $y$  are even in  $\partial_x$  and  $\partial_y$ . The linear operator  $L$  is self-adjoint, i.e.,  $L \equiv L^+$  and the symmetric relationship holds,

$$G(x_2, y_2, t|x_1, y_1, t') = G(x_1, y_1, t|x_2, y_2, t'). \quad (2.25)$$

The symmetry relationship above can be interpreted as follows: at a given time  $t > t'$  an actuator output of the controller at  $(x_2, y_2)$  due to a unit impulsive sensor input of the controller at  $(x_1, y_1)$  and time  $t'$  is equal to the actuator output at  $(x_1, y_1)$  due to a unit impulse sensor input at  $(x_2, y_2)$  and time  $t'$ .

Of particular interest here is the shape of the actuator temperature  $\theta_c(x, y, t)$  generated by a unit impulse temperature at a sensor point  $(x_p, y_p)$ , say, at  $t = t_p$ . The spatial roll off of the actuator temperature affects the spatial resolution of the spacing between sensor points. Let the impulsive measurement be

$$\theta_s(x', y', t') = \delta(x' - x_p)\delta(y' - y_p)\delta(t' - t_p), \quad (2.26)$$

from Eq.(2.22) we obtain the Green's function

$$\theta_c(x, y, t) = G(x, y, t|x_p, y_p, t_p). \quad (2.27)$$

For each Fourier mode that corresponds to the wave vector  $(k\alpha_x, m\alpha_y)$  (where  $-K/2 \leq k \leq K/2$  and  $-M/2 \leq m \leq M/2$ ), the coefficient represent an entry of measurement vector  $\mathbf{z}$  in the filter equation (2.21). We then have

$$u(z, k\alpha_x, m\alpha_y, t) = \int_0^t e^{(\mathbf{A}^* - \mathbf{K}_f \mathbf{C}^*)(t-\tau)} \mathbf{z}(\tau) d\tau. \quad (2.28)$$

Note that the homogeneous solution due to the initial condition decays rapidly and does not contribute for sufficiently large  $t$ . After the  $\mathbf{z}$  and  $u$  of all the Fourier modes are computed, a FFT will transform the two sets of coefficients to  $\theta_s(x, y, z_s, t)$  and  $\theta_c(x, y, 0, t)$ , respectively. When  $\theta_s(x, y, z_s, t)$  is impulsive according to Eq.(2.26), then Eq.(2.28) gives the Green's function.

### 3. Numerical Results

#### (a) Nonlinear convection

Above the value  $Ra = Ra_{c0} \approx 1707.76$ , the no-motion state gives rise to steady, two-dimensional convection rolls. Depending on the value of  $Pr$ , these rolls in turn will become unstable at still higher values of  $Ra$ , making transitions to two-dimensional oscillatory convection or steady three-dimensional convection depending on the value of Prandtl number. Considerable detail about the bifurcation diagram is documented in Cross & Hohenberg (1993).

Before engaging in the closed-loop numerical simulations, it is worthwhile to perform some comparison to known results, as check cases for validating the nonlinear plant model. In Clever and Busse (1974) selective Nusselt number values for the two dimensional convection solution were published. Table 1 shows the values of Nusselt number,  $Nu$ , for several different values of  $Ra$  at  $Pr = 0.71$  and  $7.0$  for two-dimensional rolls at  $\alpha_x = 3.117$  ( $\alpha_y = 0$ ). The Nusselt number is a measure of the convective heat transfer,